DESIGN AND APPLICATION OF POLYMERIC MIXED CONDUCTORS

by

Ho Joong Kim

A Dissertation

Submitted to the Faculty of Purdue University

In Partial Fulfillment of the Requirements for the degree of

Doctor of Philosophy

Davidson School of Chemical Engineering

West Lafayette, Indiana

December 2022

THE PURDUE UNIVERSITY GRADUATE SCHOOL

STATEMENT OF COMMITTEE APPROVAL

Dr. Bryan W. Boudouris, Chair

Davidson School of Chemical Engineering

Dr. Letian Dou

Davidson School of Chemical Engineering

Dr. Stephen P. Beaudoin

Davidson School of Chemical Engineering

Dr. Chi Hwan Lee

Weldon School of Biomedical Engineering

Approved by:

Dr. John Morgan

Dedicated to Namsook Lee and Hyungrae Cho, my forever missed grandparents.

ACKNOWLEDGMENTS

First and foremost, I would like to thank my advisor Dr. Bryan W. Boudouris for all the mentorship and support he has given me throughout my time here. Your keen insight, generous support, and wise mentorship helped grow and succeed both professionally and personally. At times when I had felt lost and confused, your encouragement empowered me to push forward. You are an amazing, inspirational role model as a researcher, as a leader, and as a parent. I would like to extend my gratitude to the committee members: Dr. Chi Hwan Lee, Dr. Letian Dou, and Dr. Stephen Beaudoin for their many constructive discussions, feedbacks, and suggestions that not only helped me with research but also with professional development.

I would also like to thank our collaborators: Dr. Pete Kollbaum, Dr. Kyunghun Kim, Dr. Jinyuan Zhang, and Dawn Meyer. Our working together led to so much progress and success, and I have learned a great deal from working with every single one of you. I would also like to thank the staff at Birck Nanotechnology Center, especially Dr. Joon Park and Tim Miller, for helping me with device fabrication and teaching me technical know-hows. Your help was crucial in getting me as far as I have. I must thank Beverly Johnson, Robin Waling, Jeff Valley, Nick Humphrey, Jason Davenport, and Dr. Gabriela Nagy for all the support that you provide to ensure safe and sound operation of all the research labs in our department.

My research group is one composed of individuals coming from unique backgrounds and cultures, and yet we function as one harmonized team. Thank you, Daniel, Po, Suman, Hongguang, Wenchao, Teng, Varad, Jaeyub, Noelia, Sid, John, Kuluni, Femi, Sheng-Ning, Ying, Aaron, Connie, Carsten, Hyunki, and Hamas, with whom I have had the fortune of working with. It has been a pleasurable journey, and I hope I have given as much as I have received during my time as a member of Boudouris Research Group.

My wife HyoSun, I cannot thank you enough for being there for me all these years, and giving birth to our precious daughter, Ellie. Your standing next to me all these years is what made everything possible. To my parents Dr. Yongsuk Kim and Dr. Hyunmi Cho, and last but not least, my only brother Hyo Kim. I will always love you just as you always have. It is my greatest fortune to have you all as my parents and a brother, and I can only hope to be half the parent you are.

TABLE OF CONTENTS

LIST OF TABLES

LIST OF FIGURES

LIST OF SCHEMES

ABSTRACT

Organic electronics has been a highly researched field owing to the low cost, biocompatibility, mechanical flexibility, and superior performance relative to their inorganic counterparts in some applications. Significant advancement has been achieved across various device platforms including organic light-emitting diodes (OLEDs), organic field effect transistors (OFETs), and organic solar cells, for instance. Recently, soft materials that can conduct both charge and ions simultaneously (i.e., organic mixed conductors) have been a major catalyst in the fields of biosensors and energy storage. Extensive research efforts in the organic electronics field are being invested to establish the relevant structure-property relationships to design and develop higher performing organic mixed conductors. Simultaneously, these materials are utilized in developing prototype biosensors with the aim of superior performance, lower cost, and better patient comfort and outcomes than currently available technologies. Following suit, this dissertation is dedicated to furthering organic electronics on both fundamental and applied fronts. Specifically, this work examines a novel class of redox-active macromolecules, radical polymers, as the organic electrochemical transistor (OECT) active layer. In addition, wearable ocular biosensors utilizing soft materials to realize design innovation are presented.

For the first part of the present dissertation, radical polymer-based blends are evaluated for mixed electron and ion conduction in OECTs. Traditional macromolecular design motifs for OECT active layer materials have been a closed-shell macromolecular backbone for electron conduction with charge-neutral hydrophilic side chains (e.g., triethylene glycol) for ion conduction. When poly(4-glycidyloxy-2,2,6,6-tetramethylpiperidine-1-oxyl) (PTEO) is blended with poly(3-hexylthiophene) (P3HT), 2,2,6,6-tetramethylpiperidin-N-oxy (TEMPO) radicals in PTEO act as an independent voltage regulator that modulates the ionic and hence electronic transport of the OECT devices. Electrochemical analysis of the blend films reveals that the ionic transport and hence electrochemical doping of the P3HT phase occur when the applied bias matches the onset oxidation potential of TEMPO radicals in PTEO even though that of P3HT is lower than that of TEMPO oxidation. By optimizing the blend ratio, figure-of-merit (i.e., μC^*) values over 150 F V^{-1} cm^{-1} s^{-1} at loadings as low as 5% PTEO (by weight) are achieved, placing the performance on the same order as top-performing conjugated polymers despite the mediocre

performance of pristine P3HT (<10 F V^{-1} cm^{-1} s^{-1}). These findings suggest that introduction of open-shell moieties in the OECT active layer as a secondary redox-active species may significantly improve OECT performance metrics and offer a new paradigm for future macromolecular designs.

In the second part of the dissertation, novel design strategies for wearable ocular electroretinography (ERG) sensors are presented. Typically, wearable sensors are custom-made contact lenses fabricated in a bottom-up fashion where the pre-fabricated sensor component is either embedded in the contact lens body or sandwiched between two. The present work instead utilizes commercially available contact lenses, and the corneal electrode is integrated via electropolymerization of poly(3,4-ethylenedioxythiophene):iron(III) p-toluenesulfonate (PEDOT:Tos) on the lens surface. Electrochemical analysis of the PEDOT:Tos reveals that the measured impedance is several orders of magnitude lower than that of noble metals (e.g., Au) used as the working electrode in commercial electrodes. The mechanical and chemical stability along with the soft form factor of the present design strategy enables high-fidelity recording of ERG signals in human subjects without the need for topical anesthesia.

Following the similar strategy, a new seamless wearable ocular sensor integration strategy utilizing polydopamine (PDA) conformal coating is demonstrated. In this work, we utilize its strong adhesive property originating from the van der Waals interactions between catechol moieties of PDA and various hydrophilic functional groups (e.g., hydroxy, ether, etc.) already present in commercial contact lens materials. The facile integration demonstrates high peeling strength (> 55 J m^{-2}), chemical and mechanical stability. A series of *in vivo* assessments demonstrates high accuracy, reliability, and user comfort of the fabricated wearable sensor in both animal and human subjects. The findings suggest that the PDA-assisted integration strategy may be applied in designing various future-generation wearable ocular electrophysiological sensors.

1. INTRODUCTION

An ever-increasing demand for effective diagnostics platforms has propelled the development of various biosensor and bioelectronics technology.[1–3] Organic semiconductors that conduct electronically and ionically, also known as organic mixed ionic-electronic conductors (OMIECs), have been major catalysts for such progress, owing to their low cost, biocompatibility, mechanical flexibility, and superior performance relative to their inorganic counterparts in various applications.[2,4] Most importantly, the ability to transduce ionic currents into electronic currents makes OMIECs ideal active sensing components to take in ionic biological signals produced by cellular activities and convert them into collectable electronic signals to be recorded and analyzed.[1,5–7] This unique property has caused OMIECs to be used in various bioelectronic applications including electrophysiological recorders,[8–11] biomolecular and metabolite sensors.[12–16] Significant research has been invested in establishing relevant structure-property relationships, which can drive performance improvement and fine-tuning of desired materials properties. Various OMIECs based on π-conjugated polymers have since been developed with design considerations to promote ion transport. Specifically, to promote mixed transport of ionic and electronic charges throughout the bulk of the active thin layer, charge-conducting conjugated macromolecules are complemented with solvophilic moieties via grafting[17–20] of, or blending[3,21–23] with poly(ethylene glycol) (PEG) or its derivatives. The same strategy, but with polyelectrolytes inspired by poly(3,4-ethylenedioxythiophene):polystyrene sulfonate (PEDOT:PSS), has been attempted as well.[24–26] Despite much progress and success in both fundamentals and application fronts, there is general lack in the number of chemistries being investigated.

An alternative class of soft materials incorporating organic stable radicals has been gaining increasing attention for many organic electronics applications.[27–32] Radical polymers refer to macromolecules which possess redox-active pendant groups, which can be reduced or oxidized to form closed shells with neighboring counterions or among themselves, enabling solid-state charge transport. In comparison to their conjugated counterparts, nonconjugated backbone of these materials also make them highly transmissive, and thus, appealing for optoelectronic device applications. The most studied test vehicle in this class is poly(2,2,6,6-tetramethylpiperidinyloxy methacrylate) (PTMA), and it has been employed in many

applications including organic batteries,[27] and solar cells,[33,34]. Recently, poly(4-glycidyloxy-2,2,6,6-tetramethylpiperidine-1-oxyl) (PTEO) was synthesized, which demonstrated a record-high electronic conductivity of ~20 S m^{-1} for nonconjugated macromolecules, higher than those of many undoped conjugated polymers.[35] The study highlighted that inter-radical proximity is crucial in dictating radical polymers' electronic conductivity. Additionally, PTEO stands a particularly appealing model polymer for mixed conduction applications: Its low T_g is attributed to the polyethylene oxide (PEO) backbone, and the very hydrophilicity of the backbone chemistry also relates to ionic conductivity of aqueous electrolyte. Such groundbreaking discovery showed the potential of these nonconjugated organic radical polymers with appealing properties and performance, and platforms where mixed conduction occurs present opportunities for this class of materials to be potentially employed heavily.

1.1 Dissertation Overview

The motivation for the present dissertation is to establish the structure-property relationships of radical polymer-based mixed conductors and exploit their applications in various organic electronic devices. As such, the research effort is divided between two fronts. The first theme revolves around the investigation of how redox-active radical moieties impact mixed charge and ion transport in organic electrochemical transistor (OECT) architecture. A nonconjugated radical polymer, PTEO,[35] was introduced for the first time as an ionic conductor in a blended system with poly(3-hexylthiophene) (P3HT) to showcase the advantages of having an open-shell moiety in designing an active layer for an OECT. Secondly, novel device integration methodologies are applied to develop novel wearable ocular electrophysiological sensors. Wearable electroretinography (ERG) and intraocular pressure (IOP) monitoring devices are presented where the sensor components are integrated onto commercially available contact lenses, a fundamentally different approach from previous efforts in which sensors are either embedded in an elastomer lens body or sandwiched between two.

Chapter 2 introduces organic electronics wherein mixed ionic and electronic conduction occurs. Specifically, the working principles of and the corresponding macromolecular design considerations for organic electrochemical transistor (OECT) archetype are discussed along with previous efforts in such designs. Additionally, the theoretical background and the current

measurement technologies for electroretinography (ERG) and intraocular pressure (IOP) measurement are introduced.

Chapter 3 has been published as "Radical Polymer-Based Organic Electrochemical Transistors," by H. J. Kim, K. Perera, Z. Liang, B. Bowen, J. Mei, and B. W. Boudouris, *ACS Macro Letters* **2022**, 11, 243 – 250. The article explores the impact of incorporating stable radicals (i.e., TEMPO) into the active layer of the OECTs. Specifically, PTEO was blended with P3HT to develop a novel mixed semiconductor at varying ratios to probe the effect of TEMPO radicals and its composition on the performance. Electrochemical analysis

Chapter 4 has been published as "All-printed Stretchable Corneal Sensor on Soft contact Lenses for Noninvasive and Painless Ocular Electrodiagnosis," by K. Kim, H. J. Kim, H. Zhang, W. Park, D. Meyer, M. K. Kim, B. Kim, H. Park, B. Xu, P. Kollbaum, B. W. Boudouris, and C. H. Lee, *Nature Communications* **2021**, 12, 1, 1 – 11. We fabricate a metal/elastomer composite electrode via printing, whose bonding onto commercial contact lenses is enabled by electropolymerization of poly(3,4-ethylenedioxythiophene) doped with iron (III) p-toluenesulfonate (PEDOT:Tos) at the electrode/lens interface. Electrochemical impedance spectroscopy confirms that the PEDOT:Tos electrode, also acting as the anchoring layer, demonstrates several orders of magnitude lower impedance than gold (Au) electrodes used in commercial products.

Chapter 5 has been published as "Smart Soft Contact Lenses for Continuous 24-hour Monitoring of Intraocular Pressure in Glaucoma Care," by J. Zhang, K. Kim, H. J. Kim, D. Meyer, W. Park, S. A. Lee., Y. Dai, B. Kim, H. Moon, J. Shah, K. Harris, B. Collar, K. Liu, P. Irazoqui, H. Lee, S. A. Park, P. Kollbaum, B. W. Boudouris, and C. H. Lee, *Nature Communications* **2022**, 13, 1, 1 - 15. The work demonstrates a novel ocular sensor integration scheme realized by utilizing polydopamine (PDA) as a biocompatible, electroless adhesive. PDA coating allows seamless bonding of prefabricated sensor components onto commercial contact lenses.

Chapter 6 summarizes the results and significance of the works discussed in this dissertation, followed by brief discussions on ongoing works and future suggestions. The preliminary results detailing organic radical liquid crystals with tunable electronic conductivity are presented, and future designs for the ocular electrophysiological sensors are suggested.

1.2 References

(1) Turner, A. P. F. Biosensors: Sense and Sensibility. *Chem. Soc. Rev.* **2013**, *42* (8), 3184–3196.

(2) Rivnay, J.; Owens, R. M.; Malliaras, G. G. The Rise of Organic Bioelectronics. *Chem. Mater.* **2014**, *26* (1), 679–685.

(3) Zhang, M.; Lin, P.; Yang, M.; Yan, F. Fabrication of Organic Electrochemical Transistor Arrays for Biosensing. *Biochim. Biophys. Acta - Gen. Subj.* **2013**, *1830* (9), 4402–4406.

(4) Guo, X.; Baumgarten, M.; Müllen, K. Designing π-Conjugated Polymers for Organic Electronics. *Prog. Polym. Sci.* **2013**, *38* (12), 1832–1908.

(5) Kergoat, L.; Piro, B.; Berggren, M.; Horowitz, G.; Pham, M.-C. Advances in Organic Transistor-Based Biosensors: From Organic Electrochemical Transistors to Electrolyte-Gated Organic Field-Effect Transistors. *Anal. Bioanal. Chem.* **2012**, *402* (5), 1813–1826.

(6) Marks, A.; Griggs, S.; Gasparini, N.; Moser, M. Organic Electrochemical Transistors: An Emerging Technology for Biosensing. *Adv. Mater. Interfaces* **2022**, *9* (6), 2102039.

(7) Mabeck, J. T.; Malliaras, G. G. Chemical and Biological Sensors Based on Organic Thin-Film Transistors. *Anal. Bioanal. Chem.* **2006**, *384* (2), 343–353.

(8) Khodagholy, D.; Doublet, T.; Quilichini, P.; Gurfinkel, M.; Leleux, P.; Ghestem, A.; Ismailova, E.; Hervé, T.; Sanaur, S.; Bernard, C.; et al. In Vivo Recordings of Brain Activity Using Organic Transistors. *Nat. Commun.* **2013**, *4* (1), 1–7.

(9) Hempel, F.; Law, J. K.-Y.; Nguyen, T. C.; Munief, W.; Lu, X.; Pachauri, V.; Susloparova, A.; Vu, X. T.; Ingebrandt, S. PEDOT: PSS Organic Electrochemical Transistor Arrays for Extracellular Electrophysiological Sensing of Cardiac Cells. *Biosens. Bioelectron.* **2017**, *93*, 132–138.

(10) Lee, W.; Kobayashi, S.; Nagase, M.; Jimbo, Y.; Saito, I.; Inoue, Y.; Yambe, T.; Sekino, M.; Malliaras, G. G.; Yokota, T.; et al. Nonthrombogenic, Stretchable, Active Multielectrode Array for Electroanatomical Mapping. *Sci. Adv.* **2018**, *4* (10), eaau2426.

(11) Bai, L.; Elósegui, C. G.; Li, W.; Yu, P.; Fei, J.; Mao, L. Biological Applications of Organic Electrochemical Transistors: Electrochemical Biosensors and Electrophysiology Recording. *Front. Chem.* **2019**, *7*, 313.

(12) Tang, H.; Yan, F.; Lin, P.; Xu, J.; Chan, H. L. W. Highly Sensitive Glucose Biosensors Based on Organic Electrochemical Transistors Using Platinum Gate Electrodes Modified with Enzyme and Nanomaterials. *Adv. Funct. Mater.* **2011**, *21* (12), 2264–2272.

(13) Lin, P.; Luo, X.; Hsing, I. M.; Yan, F. Organic Electrochemical Transistors Integrated in Flexible Microfluidic Systems and Used for Label-Free DNA Sensing. *Adv. Mater.* **2011**, *23* (35), 4035–4040.

(14) Gualandi, I.; Tonelli, D.; Mariani, F.; Scavetta, E.; Marzocchi, M.; Fraboni, B. Selective Detection of Dopamine with an All PEDOT:PSS Organic Electrochemical Transistor. *Sci. Rep.* **2016**, *6* (1), 1–10.

(15) Tang, H.; Lin, P.; Chan, H. L. W.; Yan, F. Highly Sensitive Dopamine Biosensors Based on Organic Electrochemical Transistors. *Biosens. Bioelectron.* **2011**, *26* (11), 4559–4563.

(16) Currano, L. J.; Sage, F. C.; Hagedon, M.; Hamilton, L.; Patrone, J.; Gerasopoulos, K. Wearable Sensor System for Detection of Lactate in Sweat. *Sci. Rep.* **2018**, *8* (1), 1–11.

(17) Giovannitti, A.; Maria, I. P.; Hanifi, D.; Donahue, M. J.; Bryant, D.; Barth, K. J.; Makdah, B. E.; Savva, A.; Moia, D.; Zetek, M.; et al. The Role of the Side Chain on the Performance of N-Type Conjugated Polymers in Aqueous Electrolytes. *Chem. Mater.* **2018**, *30* (9), 2945–2953.

(18) Savagian, L. R.; Österholm, A. M.; Ponder, J. F.; Barth, K. J.; Rivnay, J.; Reynolds, J. R. Balancing Charge Storage and Mobility in an Oligo(Ether) Functionalized Dioxythiophene Copolymer for Organic- and Aqueous- Based Electrochemical Devices and Transistors. *Adv. Mater.* **2018**, *30* (50), 1804647.

(19) Parr, Z. S.; Rashid, R. B.; Paulsen, B. D.; Poggi, B.; Tan, E.; Freeley, M.; Palma, M.; Abrahams, I.; Rivnay, J.; Nielsen, C. B. Semiconducting Small Molecules as Active Materials for P-Type Accumulation Mode Organic Electrochemical Transistors. *Adv. Electron. Mater.* **2020**, *6* (6), 2000215.

(20) Flagg, L. Q.; Bischak, C. G.; Onorato, J. W.; Rashid, R. B.; Luscombe, C. K.; Ginger, D. S. Polymer Crystallinity Controls Water Uptake in Glycol Side-Chain Polymer Organic Electrochemical Transistors. *J. Am. Chem. Soc.* **2019**, *141* (10), 4345–4354.

(21) Jimison, L. H.; Hama, A.; Strakosas, X.; Armel, V.; Khodagholy, D.; Ismailova, E.; Malliaras, G. G.; Winther-Jensen, B.; Owens, R. M. PEDOT: TOS with PEG: A Biofunctional Surface with Improved Electronic Characteristics. *J. Mater. Chem.* **2012**, *22* (37), 19498–19505.

(22) Frankenstein, H.; Stein, E.; Stolov, M.; Koifman Khristosov, M.; Freger, V.; Frey, G. L. Blends of Polymer Semiconductor and Polymer Electrolyte for Mixed Ionic and Electronic Conductivity. *J. Mater. Chem. C* **2021**, *9* (24), 7765–7777.

(23) Strakosas, X.; Sessolo, M.; Hama, A.; Rivnay, J.; Stavrinidou, E.; Malliaras, G. G.; Owens, R. M. A Facile Biofunctionalisation Route for Solution Processable Conducting Polymer Devices. *J. Mater. Chem. B* **2014**, *2* (17), 2537–2545.

(24) Ouyang, L.; Musumeci, C.; Jafari, M. J.; Ederth, T.; Inganäs, O. Imaging the Phase Separation between PEDOT and Polyelectrolytes during Processing of Highly Conductive PEDOT:PSS Films. *ACS Appl. Mater. Interfaces* **2015**, *7* (35), 19764–19773.

(25) Inal, S.; Rivnay, J.; Hofmann, A. I.; Uguz, I.; Mumtaz, M.; Katsigiannopoulos, D.; Brochon, C.; Cloutet, E.; Hadziioannou, G.; Malliaras, G. G. Organic Electrochemical Transistors Based on PEDOT with Different Anionic Polyelectrolyte Dopants. *J. Polym. Sci. Part B Polym. Phys.* **2016**, *54* (2), 147–151.

(26) Lill, A. T.; Cao, D. X.; Schrock, M.; Vollbrecht, J.; Huang, J.; Nguyen-Dang, T.; Brus, V. V; Yurash, B.; Leifert, D.; Bazan, G. C. Organic Electrochemical Transistors Based on the Conjugated Polyelectrolyte PCPDTBT-SO3K (CPE-K). *Adv. Mater.* **2020**, *32* (33), 1908120.

(27) Nakahara, K.; Oyaizu, K.; Nishide, H. Organic Radical Battery Approaching Practical Use. *Chem. Lett.* **2011**, *40* (3), 222–227.

(28) Bobela, D. C.; Hughes, B. K.; Braunecker, W. A.; Kemper, T. W.; Larsen, R. E.; Gennett, T. Close Packing of Nitroxide Radicals in Stable Organic Radical Polymeric Materials. *J. Phys. Chem. Lett.* **2015**, *6* (8), 1414–1419.

(29) Rostro, L.; Wong, S. H.; Boudouris, B. W. Solid State Electrical Conductivity of Radical Polymers as a Function of Pendant Group Oxidation State. *Macromolecules* **2014**, *47* (11), 3713–3719.

(30) Oyaizu, K.; Ando, Y.; Konishi, H.; Nishide, H. Nernstian Adsorbate-like Bulk Layer of Organic Radical Polymers for High-Density Charge Storage Purposes. *J. Am. Chem. Soc.* **2008**, *130* (44), 14459–14461.

(31) Aqil, A.; Vlad, A.; Piedboeuf, M. L.; Aqil, M.; Job, N.; Melinte, S.; Detrembleur, C.; Jérôme, C. A New Design of Organic Radical Batteries (ORBs): Carbon Nanotube Buckypaper Electrode Functionalized by Electrografting. *Chem. Commun.* **2015**, *51* (45), 9301–9304.

(32) Wilcox, D. A.; Agarkar, V.; Mukherjee, S.; Boudouris, B. W. Stable Radical Materials for Energy Applications. *Annu. Rev. Chem. Biomol. Eng.* **2018**, *9*, 83–103.

(33) Rostro, L.; Galicia, L.; Boudouris, B. W. Suppressing the Environmental Dependence of the Open-Circuit Voltage in Inverted Polymer Solar Cells through a Radical Polymer Anodic Modifier. *J. Polym. Sci. Part B Polym. Phys.* **2015**, *53* (5), 311–316.

(34) Sung, S. H.; Bajaj, N.; Rhoads, J. F.; Chiu, G. T.; Boudouris, B. W. Radical Polymers Improve the Metal-Semiconductor Interface in Organic Field-Effect Transistors. *Org. Electron.* **2016**, *37*, 148–154.

(35) Joo, Y.; Agarkar, V.; Sung, S. H.; Savoie, B. M.; Boudouris, B. W. A Nonconjugated Radical Polymer Glass with High Electrical Conductivity. *Science (80-.).* **2018**, *359* (6382), 1391–1395.

2. ORGANIC ELECTRONICS BASED ON MIXED ION AND ELECTRON CONDUCTORS

In this chapter, we highlight the fundamentals of various electronic technology. Currently available technology and devices are introduced along with their shortcomings, where opportunities for improvement arise with the use of novel soft materials. Specifically, the working principle of an organic electrochemical transistor (OECT) and material design strategies so far are introduced. We also focus on the need for electroretinography (ERG) and intraocular pressure (IOP) measurement, which are used by ophthalmologists for diagnoses of retinopathy issues and glaucoma, respectively.

2.1 Organic Electrochemical Transistors (OECTs) as In-Situ Biosensors

Organic electrochemical transistors (OECTs) have garnered considerable attention as active sensing components across various applications employed including biomolecular sensors,[1,2] cellular sensors,[3,4] and neural interface devices.[5–7] An OECT is a three-terminal device in which the electronic conductivity that is established between source (S) and drain (D) terminals is modulated in response to a gate bias (G), analyte, or biological event (Figure 2.1). The device architecture of OECTs resembles that of a more traditional field-effect transistor with a top gate-bottom contact configuration. The key difference between the two device types, however, is that doping occurs throughout (at least most of) the channel volume in OECTs, whereas doping of the organic field-effect transistor (OFET) active layer occurs only at the channel/(gate)electrolyte interface. The volumetric doping of the OECT active layer is enabled by injection of solvated ionic dopants, driven by gate bias, which can maintain charge neutrality of the active layer.

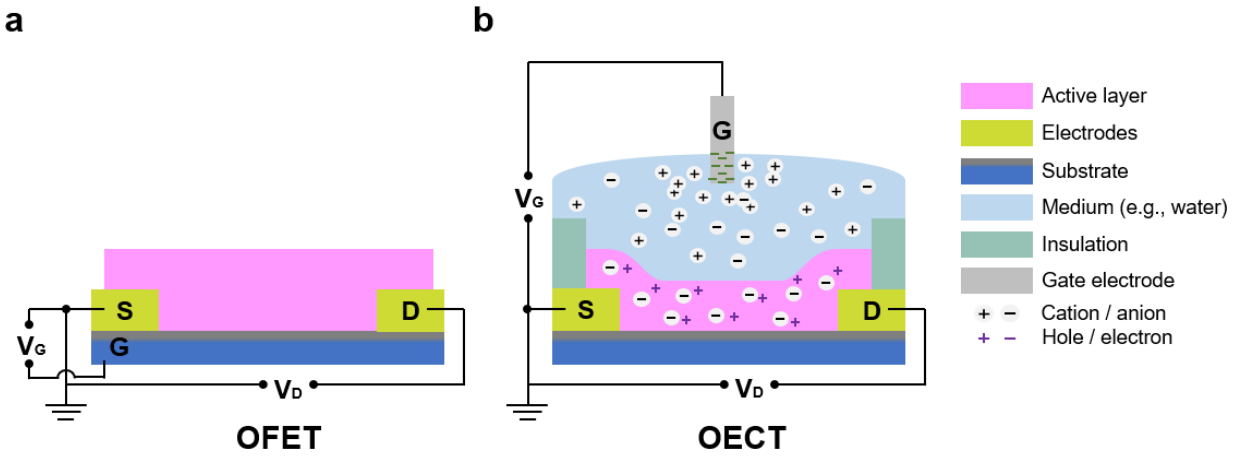

Figure 2.1. Representative schematics of accumulation-mode organic thin film transistors at their ON state. The applied voltage from gate modulates the current flowing from source to drain via (a) interfacial inversion of charges in OFETs or via (b) bulk electrochemical oxidation/reduction of active layer in OECTs.

The analytical model commonly used to describe the OECT operation is one formulated by Bernards et al.,[8] which describes an OECT as having an ionic circuit and an electronic circuit. In the model, the electronic circuit simply consists of a resistor relating to the conductivity of the channel semiconductor, while the ionic circuit consists of a resistor and a capacitor, representing the electrolyte diffusion and ion uptake within the channel volume, respectively. The resulting expression for the source-drain current in the Bernard model, I_D, is as follows:

$$I_D = \left(\frac{Wd}{L}\right) \mu C^* \left[V_P - V_G + \frac{1}{2}V_D\right] V_D$$

The notion that the ion uptake of the polymeric film in OECTs indeed is purely volumetric has been proven experimentally.[9,10] In turn, this difference in dimensionality of the (de)doping process therefore leads to two to three order-of-magnitude difference in transconductance between the two transistor structures. The capacitance has a linear dependence on the film volume with a zero offset, suggesting that there was insignificant ion accumulation at the electrolyte/channel interface.

The performance of the OECT active layer is typically represented with its transconductance, g_m, taken as the first derivative of I_D with respect to V_G. The model offers a

decent fit for describing the output and transfer characteristics of an OECT and can be distilled down to an equation for steady-state g_m at saturation as follows:

$$g_m = \frac{dI_D}{dV_G} = \left(\frac{Wd}{L}\right)\mu C^*(|V_T - V_G|)$$

The first terms L, W, and d represent the active channel area dimensions, the channel length, width, and thickness, while V_T and V_G refer to the channel threshold voltage and the gate voltage, respectively. The middle terms, the carrier mobility (μ) and the volumetric capacitance (C^*) capture the material properties. More specifically, μ and C^* are directly related to electronic transport and ionic penetration within the polymer channel, respectively. Volumetric capacitance of counterion dopants of OECTs is orders of magnitude higher than that of OFETs, which leads to the difference in transconductance between the two device types.[11] A as a general rule of thumb, which applies to traditional forms of transistors, higher carrier mobility and capacitance are desirable in OECTs in order to achieve high g_m. In addition, quick transient response (i.e., how fast the device can be turned on and off) and long-term stability are other important qualities desired in OECT channel materials.

Unlike in field-effect transistors, the concept of an OECT device being comprised of two distinct channels – ionic and electronic – should be cautiously approached because of ion-electron coupling. The structure-property relationships of organic semiconductors in terms of mixed conduction seems to suggest a fundamental trade-off between the two parameters: μ is associated with well-ordered, crystalline morphology of conducting polymer, whereas C^* is favored for amorphous domain with higher free volume.[12,13] Dopants are in the forms of solvated ions injected into the organic semiconductor, which, upon injection, would cause the polymer would swell and undergo molecular rearrangement to accommodate them.[14] These morphological changes, in turn, would affect the molecular packing and alters the overall percolation of the charge conduction. As such, after more than a decade of extensive research on mixed conduction experimentally and computationally, analyses on the underlying structure-property relationships remain controversial.

2.1.1 Mixed Conduction in Conjugated Polymers

The world of organic electronics has been dominated by conjugated polymers. Conjugated polymers refer to macromolecules consisting of alternating single and double bonds

along the backbone. Delocalization of the π-orbitals allow for facile transport of charges along the backbone, render this class of polymers electronically active. The electronic conductivity of these conjugated polymers in their neutral state is low but can be modulated through the incorporation of dopants. The most often employed conductor among conjugated polymers is poly(3,4-ethylenedioxythiophene) doped with poly(styrene sulfonate) (PEDOT:PSS). PEDOT:PSS is a polyelectrolyte complex composed of PEDOT doped with surrounding deprotonated PSS polyanion. Many of the desirable qualities, including high conductivity, water-processability, and commercial availability, have motivated academia to readily employ PEDOT:PSS across various applications.[15–24] Although the excitement around PEDOT:PSS in organic electronics is still ongoing, the material is not without a few shortcomings. PEDOT:PSS OECTs typically operate in depletion mode, which means that a large hole current flows through the channel in the absence of a gate bias. This can potentially raise concerns in its use in lab-on-a-chip bioelectronics where form factors (and battery sizes) are quite limiting. PEDOT:PSS also has a Young's modulus significantly higher than those of biological tissues, which could limit future implantable bioelectronics application.[25] Lastly, PEDOT:PSS has a complex structure which limits its use as a model system in the pursuit of expanding general understanding of the underlying structure-property relationships involved in OECT.

Different molecular design strategies have been examined in developing alternative high-performance OECT active layers. The majority of the design motifs and principles employed in synthesizing OECT materials is inherited from similar fields including OFET platforms. Various other backbone chemistries including propylenedioxythiophene (ProDOT),[26] diketopyrrolopyrrole (DPP),[27] isoindigo,[28] and naphthalene-1,4,5,8-tetracarboxylic-diimide (NDI),[29,30] have been used to synthesize OECT materials. However, unlike in OFETs, where heavy focus is placed on the crystallinity of OFET materials to maximize the carrier mobility, the volumetric capacitance of the film is paramount in improving the OECT performance. Functionalization of conjugated backbones with ethylene glycol (EG) pendant groups is one of the most common and powerful design approaches to boost the overall hydrophilicity, and therefore, the volumetric capacitance.[26,31] OECTs made from poly(2-(3,3'-bis(2-(2-(2-methoxyethoxy)ethoxy)ethoxy)-[2,2′-bithiophen]-5-yl)thieno[3,2-b]thiophene) p(g2T-TT) and its derivatives exhibit state-of-the-art performance of $\mu C^* > 500$ F V^{-1} cm^{-1} s^{-1}.[32] These studies suggest that controlling the amount and the distribution of hydrophilic and ionically conductive

moieties can act as an effective handle in controlling the performance of OECT materials. Despite much progress and success in both fundamentals and application fronts, there is general lack in the number of chemistries being investigated.

2.1.2 Radical Polymers

An alternative class of soft materials incorporating organic stable radicals has been gaining increasing attention for organic electronics applications.[33–38] Radical polymers refer to macromolecules that possess redox-active pendant groups, which can be reduced or oxidized to form closed shells with neighboring counterions or among themselves, enabling solid-state charge transport. In comparison to their conjugated counterparts, nonconjugated backbones of these materials also make them highly transmissive, and thus appealing for optoelectronic device applications. The most studied test vehicle in this class is poly(2,2,6,6-tetramethylpiperidinyloxy methacrylate) (PTMA), and it has been employed in many applications including organic batteries,[33] and solar cells,[39,40]. Recently, poly(4-glycidyloxy-2,2,6,6-tetramethylpiperidine-1-oxyl) (PTEO) was synthesized by Joo et al., which demonstrated a record-high electronic conductivity of ~20 S m^{-1} for nonconjugated macromolecules, higher than those of many undoped conjugated polymers.[41] The study highlighted that inter-radical proximity is crucial in dictating radical polymers' electronic conductivity. Despite continued improvements, radical polymers have yet to witness expansion in terms of the span of their applications beyond organic energy storage devices. PTEO stands a particularly appealing model polymer for mixed conduction applications. Its low T_g is attributed to the polyethylene oxide (PEO) backbone, and the hydrophilicity of the backbone chemistry also relates to ionic conductivity of aqueous electrolyte. Such groundbreaking discovery showed the potential of these nonconjugated organic radical polymers with appealing properties and performance, and an OECT platform where mixed conduction occurs is yet another test bed for this class of materials to be potentially heavily employed.

2.2 ERG Examination for Diagnosis of Retinopathy

Electroretinography (ERG) is an ophthalmologic diagnostic exam that measures the mass electrical responses of various retinal cells.[42] The ERG carries clinical utility as it allows

clinicians to extract diagnostic information on various retinopathy in a noninvasive manner. The electrical responses arise from currents generated by retinal cells upon exposure of light stimuli of standardized intensity and patterns, which are collected by electrodes in either direct or indirect contact with a patient's cornea. The minimum set of retinograms to be collected for clinically valid diagnostics is called full-field ERG (ffERG).[43,44] The examination parameters are specifically defined by the International Society for Clinical Electrophysiology of Vision (ISCEV). Depending on the light adaptation (light-adapted or dark-adapted), intensity of the light flicker (0.01 or 3.0 $cd \cdot s \cdot m^{-2}$), and the pattern (single burst or flickers), responses from different retinal cells including photoreceptors (rods and cones), responses of inner retinal cells and ganglion cells can be selectively or collectively acquired (Figure 2.2).

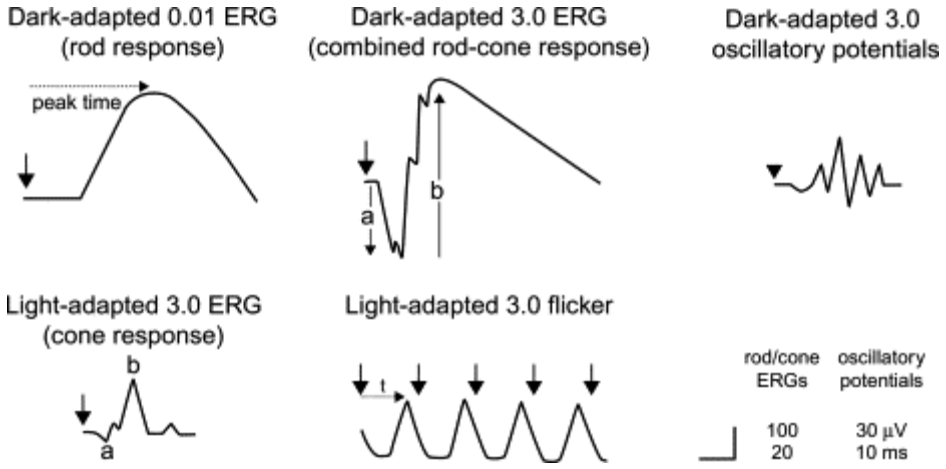

Figure 2.2. Schematic diagram of the five different electroretinograms. Light pulses of weaker magnitudes (i.e., 0.01 $cd \cdot s \cdot m^{-2}$) stimulate the rod cells ('a' wave), while more intense pulses tend to draw out responses of the cone and ganglion cells ('b' wave).

Different conditions are designed to specifically target and isolate responses from retinal cells, which are nominally called a waves and b waves. There are other waves, namely c and d waves, which originate from scleral and pigment epithelial cells. For instance, a dark-adapted 0.01 ERG (e.g., a single light pulse of 0.01 $cd \cdot s \cdot m^{-2}$ subjected to an eye adapted to a dark background for approximately 20 minutes) elicits a b-wave response, attributed to the rod-biopolar cells. The amplitude of the a wave and the implicit time would then be extracted and analyzed to check for any abnormality.

2.2.1 Electrodes Used in ERG

Many commercially available working electrodes capable of recording ERGs exist, and they can be categorized into different types by where they are placed. The two most commonly employed subtypes are corneal and conjunctival electrodes as shown in Figure 2.3. The further an electrode is placed away from the patient's eye the weaker the recorded response becomes.[45] The signal-to-noise ratio decreases further because the signals must travel further through more cell layers.

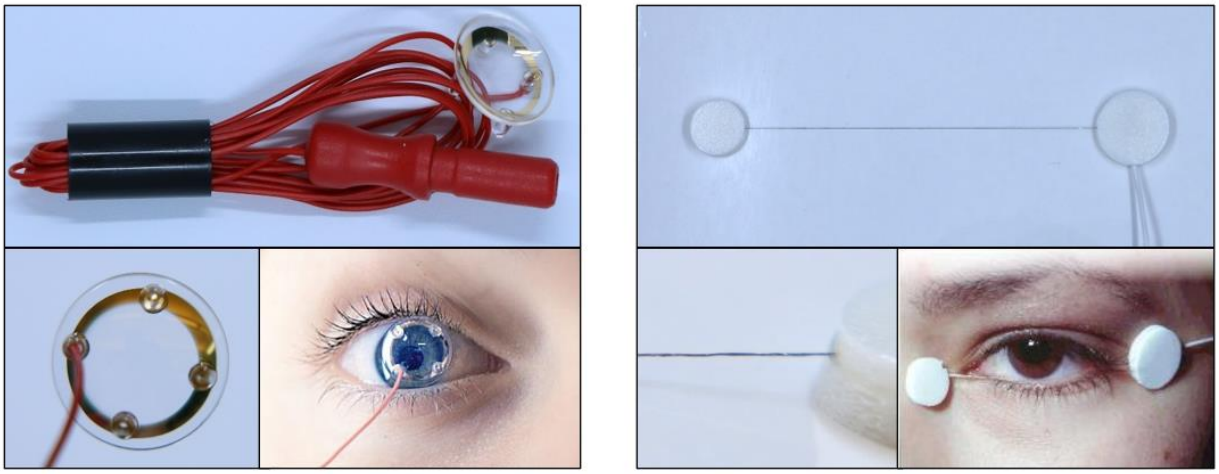

Figure 2.3. ERG-Jet™ corneal (left) and DTL Plus™ conjunctival (right) electrodes used for ERG. While the direct corneal contact allows collection of higher-quality ERGs, the rigid lens body of the corneal electrodes cause misalignment and much discomfort despite application of anesthesia.

While high-quality ERG response is desirable for accurate diagnosis of patient's retinal physiology, another significant factor clinicians consider is the patient's comfort. Corneal electrodes, while capable of collecting higher quality ERG responses, tend to cause more discomfort in patients during usage.[46] ERG-Jet electrodes, for instance, are composed of rigid plastic lens body with an electroplated gold around the periphery acting as the electrode. When using corneal electrodes like the ERG-Jet, the ISCEV protocol mandates the use of topical anesthesia. This contrasts with the case of conjunctival electrodes, such as DTL Plus, in which using anesthesia is optional. Even with the aid of topical anesthesia, surveys revealed that patients prefer electrodes that cause them less discomfort.[46] It is therefore a highly investigated

venue to develop a novel corneal ERG electrode with novel materials that capture high amplitudes of ERG biopotential shifts while causing minimal discomfort.

2.3 Intraocular Pressure (IOP) as the Primary Risk Factor for Glaucoma Diagnosis

Glaucoma is the second leading cause of blindness and the leading cause of irreversible loss of vision worldwide.[47] In a typical case of glaucoma, an abnormal build-up of fluid (i.e., aqueous humor) in the anterior chamber increases the intraocular pressure (IOP) of the patient's eye and the increased pressure exerts leads to optic nerve damages (Figure 2.4). This fluid build-up is the result of malfunctioning drainage canal called trabecular meshwork, induced either by its obstruction (primary open angle glaucoma; POAG) or by elevated pressure blocking the entire trabecular meshwork (acute angle-closure glaucoma; AACG). The predominant subtype, POAG, accounts for the more than two-thirds of all cases of glaucoma and about 90% of primary glaucoma cases (i.e., it develops without any identifiable underlying disease).[48–50] While the number of POAG cases in elderly populations (40–80 years of age) is estimated to increase from 53 million in 2020 to 80 million in 2040, at least half of the glaucoma cases are unaware of the condition or undiagnosed.[51,52] The difficulty with POAG is that there are no noticeable symptoms, and patients do not perceive them until at least 30% of the optic nerve tissues have been irreversibly damaged. Early detection and appropriate treatment of glaucoma is therefore crucial in slowing its progression and preventing permanent vision loss.

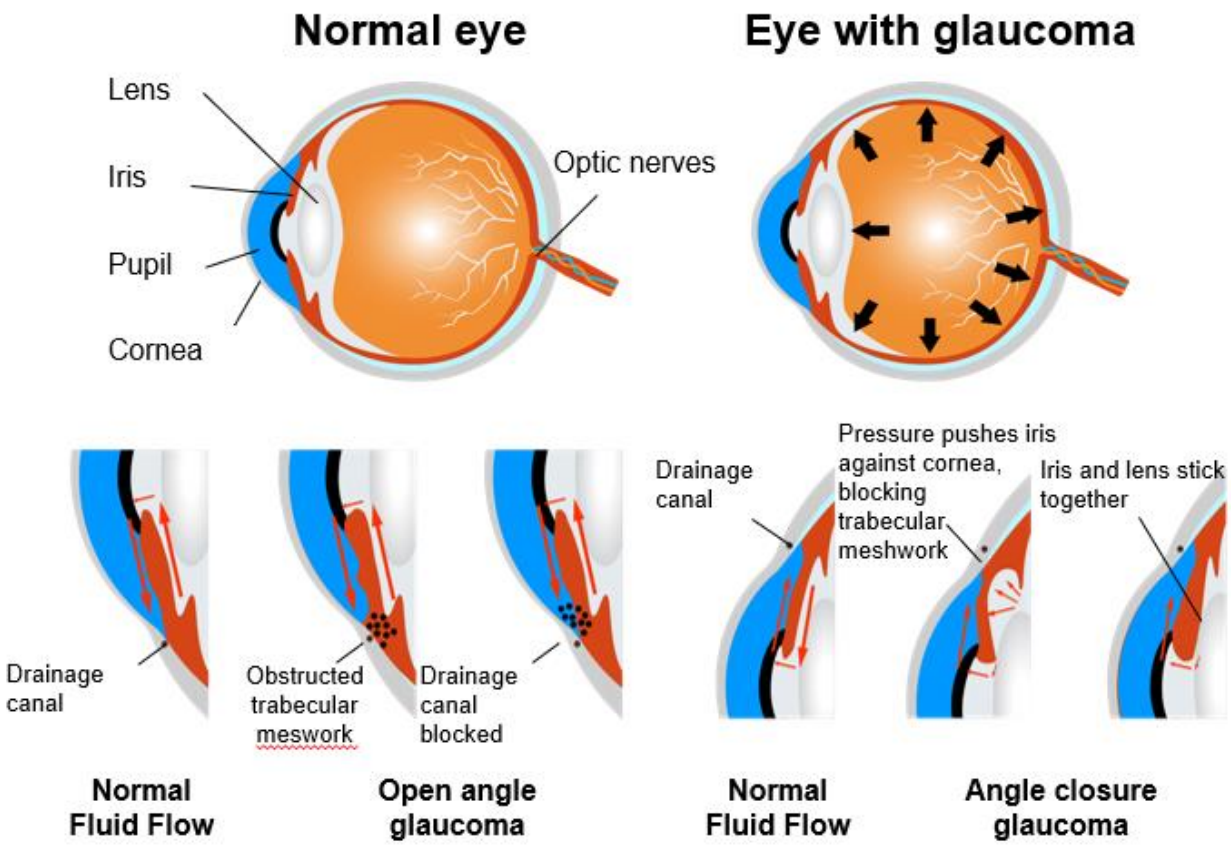

Figure 2.4. Comparison of a normal eye and an eye with glaucoma. Both primary open-angle glaucoma (POAG) and chronic angle-closure glaucoma (CACG) lead to an increased pressure build-up, damaging optic nerves located at the back of the eye near retina.

Glaucoma is typically diagnosed at clinics through a comprehensive eye examination, which is a series of examinations to screen for and diagnose common ocular diseases. While there are many other risk factors including the patient's age, family history, myopia, and the presence of certain systemic diseases such as diabetes,[50,53–56] the primary risk factor being typically monitored is the patient's IOP. Measurement of IOP is performed with any of various tonometer types, including applanation tonometer, pneumatonometer, and dynamic contour tonometer. Among various tonometers, Goldmann applanation tonometry (GAT) has been the gold standard for IOP measurements.[57–60] However, the clinically adopted methods are not without limitations. First, IOP follows a circadian rhythm and typically peaks at night. Measurements of IOP taken during the day at clinics may lead to false negative results. Additionally, severe IOP fluctuations are not captured by these measurements because a single

measurement is taken during an eye exam.[61–63] Unusually large diurnal fluctuations in IOP despite the normal baseline is associated with glaucoma, but typical tonometry-based IOP measurements from occasional clinic visits fail to capture them.

2.3.1 Wearable IOP Sensors Working Principle

Continuous, real-time monitoring of IOP has been desirable as it would allow early detection of glaucoma and prevention of significant vision impairment. In contrast to the implantable, in-situ IOP monitoring counterparts, wearable sensors are free from device infection/malfunction risks, can be easily unequipped when needed, and do not require invasive surgeries. Since demonstration of the first prototype as early as back in 1974,[64] many advances have been made in developing various wearable IOP sensors integrated into contact lens bodies, utilizing different sensing mechanisms.[65] Depending on the working principle, most of the IOP sensor devices can be categorized into inductive coupling telemetry,[66–69] piezoresistive,[70] and microfluidic sensors.[71,72] The most frequently studied subtype for developing wearable IOP sensors is the inductive coupling telemetry (Figure 2.5).

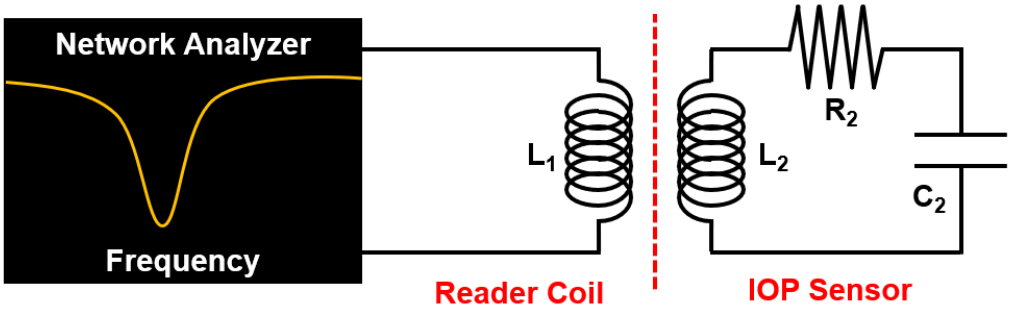

Figure 2.5. The conceptual diagram and the equivalent circuit of inductive coupling telemetry. The sensor component registers IOP variations via a circuit element (e.g., a resistor or a capacitor), and the corresponding changes in C_2 or R_2 are reflected in shifting of the recorded resonant frequency, *f*. Subscripts 1 and 2 refer to the reader coil and the wearable IOP sensor, respectively.

The inductive coupling telemetry allows wireless powering and data transmission, and hence offers a smaller form factor as the sensor component does not require a battery. The

equivalent circuit of the sensor unit is an inductor-capacitor-resistor (LCR) coupled with an inductor (reading coil) whose resonant frequency is defined as follows:

$$f = \frac{1}{2\pi}\sqrt{\frac{1}{L_2^2 C_2^2} - \frac{R_2^2}{L_2^2}} \approx \frac{1}{2\pi\sqrt{L_2 C_2}} \quad if \quad R_2 \ll \sqrt{\frac{L_2}{C_2}}$$

Where L_2, C_2, and R_2 refer to the sensor inductance, capacitance, and resistance, respectively. The sensor is linked to an external reading coil in proximity for wireless communication of real-time frequency data. The resonant frequency shifts when the inductance or capacitance of the sensor component changes, which in turn reflects changes in the corneal curvature determined by the IOP.

Considerable research effort has been devoted to designing and developing various wireless IOP monitoring device prototypes with successful demonstration of both in-vivo and ex-vivo IOP tracking on animal eyes.[68,69,72–74] Typically, these wearable sensors are fabricated by integrating active integrated circuit (IC) components and functional nanomaterials (e.g., graphene and metal nanowires) embedded in biocompatible polymer bodies (e.g., parylene C, and SU-8, hydrogels, silicone, etc.). Despite the initial success, these approaches have issues associated with long-term usage and wear. The lack of mechanical durability, chemical instability, insufficient water content and oxygen transmissibility, and/or safety risks with stiff IC chips limit their implementation on human subjects.[65] Meanwhile, commercially available soft contact lenses (SCLs), consisting of variations of different biocompatible hydrogels and silicone, satisfy all of those criteria set forth by the U.S. Food and Drug Administration (FDA). It is therefore highly desirable to incorporate these SCLs in fabricating continuous IOP monitoring sensors which, upon realization, will facilitate implementation on human patients. However, while these SCLs provide an attractive substrate on which to mount IOP monitoring devices, it remains a considerable engineering challenge to develop safe and durable integration of the two.

2.4 References

(1) Khodagholy, D.; Curto, V. F.; Fraser, K. J.; Gurfinkel, M.; Byrne, R.; Diamond, D.; Malliaras, G. G.; Benito-Lopez, F.; Owens, R. M. Organic Electrochemical Transistor Incorporating an Ionogel as a Solid State Electrolyte for Lactate Sensing. *J. Mater. Chem.* **2012**, *22* (10), 4440–4443.

(2) Parlak, O.; Keene, S. T.; Marais, A.; Curto, V. F.; Salleo, A. Molecularly Selective Nanoporous Membrane-Based Wearable Organic Electrochemical Device for Noninvasive Cortisol Sensing. *Sci. Adv.* **2018**, *4* (7), eaar2904.

(3) Kuhlbusch, T. A. J.; Asbach, C.; Fissan, H.; Göhler, D.; Stintz, M. Nanoparticle Exposure at Nanotechnology Workplaces: A Review. *Part. Fibre Toxicol.* **2011**, *8* (1), 22.

(4) Leung, C. H.; Wu, K. J.; Li, G.; Wu, C.; Ko, C. N.; Ma, D. L. Application of Label-Free Techniques in Microfluidic for Biomolecules Detection and Circulating Tumor Cells Analysis. *TrAC - Trends Anal. Chem.* **2019**, *117*, 78–83.

(5) Williamson, A.; Ferro, M.; Leleux, P.; Ismailova, E.; Kaszas, A.; Doublet, T.; Quilichini, P.; Rivnay, J.; Rõzsa, B.; Katona, G.; et al. Localized Neuron Stimulation with Organic Electrochemical Transistors on Delaminating Depth Probes. *Adv. Mater.* **2015**, *27* (30), 4405–4410.

(6) Gerasimov, J. Y.; Gabrielsson, R.; Forchheimer, R.; Stavrinidou, E.; Simon, D. T.; Berggren, M.; Fabiano, S. An Evolvable Organic Electrochemical Transistor for Neuromorphic Applications. *Adv. Sci.* **2019**, *6* (7), 1801339.

(7) Khodagholy, D.; Doublet, T.; Quilichini, P.; Gurfinkel, M.; Leleux, P.; Ghestem, A.; Ismailova, E.; Hervé, T.; Sanaur, S.; Bernard, C.; et al. In Vivo Recordings of Brain Activity Using Organic Transistors. *Nat. Commun.* **2013**, *4* (1), 1–7.

(8) Bernards, D. A.; Malliaras, G. G. Steady-State and Transient Behavior of Organic Electrochemical Transistors. *Adv. Funct. Mater.* **2007**, *17* (17), 3538–3544.

(9) Rivnay, J.; Leleux, P.; Ferro, M.; Sessolo, M.; Williamson, A.; Koutsouras, D. A.; Khodagholy, D.; Ramuz, M.; Strakosas, X.; Owens, R. M.; et al. High-Performance Transistors for Bioelectronics through Tuning of Channel Thickness. *Sci. Adv.* **2015**, *1* (4), e1400251.

(10) Volkov, A. V.; Wijeratne, K.; Mitraka, E.; Ail, U.; Zhao, D.; Tybrandt, K.; Andreasen, J. W.; Berggren, M.; Crispin, X.; Zozoulenko, I. V. Understanding the Capacitance of PEDOT:PSS. *Adv. Funct. Mater.* **2017**, *27* (28), 1700329.

(11) Inal, S.; Malliaras, G. G.; Rivnay, J. Benchmarking Organic Mixed Conductors for Transistors. *Nat. Commun.* **2017**, *8* (1), 1767.

(12) Wu, X.; Surendran, A.; Ko, J.; Filonik, O.; Herzig, E. M.; Müller-Buschbaum, P.; Leong, W. L. Ionic-Liquid Doping Enables High Transconductance, Fast Response Time, and High Ion Sensitivity in Organic Electrochemical Transistors. *Adv. Mater.* **2019**, *31* (2), 1805544.

(13) Noriega, R.; Rivnay, J.; Vandewal, K.; Koch, F. P. V.; Stingelin, N.; Smith, P.; Toney, M. F.; Salleo, A. A General Relationship between Disorder, Aggregation and Charge Transport in Conjugated Polymers. *Nat. Mater.* **2013**, *12* (11), 1038–1044.

(14) Flagg, L. Q.; Giridharagopal, R.; Guo, J.; Ginger, D. S. Anion-Dependent Doping and Charge Transport in Organic Electrochemical Transistors. *Chem. Mater.* **2018**, *30* (15), 5380–5389.

(15) Gualandi, I.; Tonelli, D.; Mariani, F.; Scavetta, E.; Marzocchi, M.; Fraboni, B. Selective Detection of Dopamine with an All PEDOT:PSS Organic Electrochemical Transistor. *Sci. Rep.* **2016**, *6* (1), 1–10.

(16) Stříteský, S.; Marková, A.; Víteček, J.; Šafaříková, E.; Hrabal, M.; Kubáč, L.; Kubala, L.; Weiter, M.; Vala, M. Printing Inks of Electroactive Polymer PEDOT:PSS: The Study of Biocompatibility, Stability, and Electrical Properties. *J. Biomed. Mater. Res. - Part A* **2018**, *106* (4), 1121–1128.

(17) Inal, S.; Rivnay, J.; Hofmann, A. I.; Uguz, I.; Mumtaz, M.; Katsigiannopoulos, D.; Brochon, C.; Cloutet, E.; Hadziioannou, G.; Malliaras, G. G. Organic Electrochemical Transistors Based on PEDOT with Different Anionic Polyelectrolyte Dopants. *J. Polym. Sci. Part B Polym. Phys.* **2016**, *54* (2), 147–151.

(18) Zhang, M.; Lin, P.; Yang, M.; Yan, F. Fabrication of Organic Electrochemical Transistor Arrays for Biosensing. *Biochim. Biophys. Acta - Gen. Subj.* **2013**, *1830* (9), 4402–4406.

(19) Khodagholy, D.; Gurfinkel, M.; Stavrinidou, E.; Leleux, P.; Herve, T.; Sanaur, S.; Malliaras, G. G. High Speed and High Density Organic Electrochemical Transistor Arrays. *Appl. Phys. Lett.* **2011**, *99* (16), 227.

(20) Rivnay, J.; Leleux, P.; Sessolo, M.; Khodagholy, D.; Hervé, T.; Fiocchi, M.; Malliaras, G. G. Organic Electrochemical Transistors with Maximum Transconductance at Zero Gate Bias. *Adv. Mater.* **2013**, *25* (48), 7010–7014.

(21) Bihar, E.; Deng, Y.; Miyake, T.; Saadaoui, M.; Malliaras, G. G.; Rolandi, M. A Disposable Paper Breathalyzer with an Alcohol Sensing Organic Electrochemical Transistor. *Sci. Rep.* **2016**, *6* (1), 1–6.

(22) Nilsson, D.; Kugler, T.; Svensson, P. O.; Berggren, M. An All-Organic Sensor-Transistor Based on a Novel Electrochemical Transducer Concept Printed Electrochemical Sensors on Paper. *Sensors Actuators, B Chem.* **2002**, *86* (2–3), 193–197.

(23) Coppedè, N.; Tarabella, G.; Villani, M.; Calestani, D.; Iannotta, S.; Zappettini, A. Human Stress Monitoring through an Organic Cotton-Fiber Biosensor. *J. Mater. Chem. B* **2014**, *2* (34), 5620–5626.

(24) Lin, P.; Yan, F.; Chan, H. L. W. Ion-Sensitive Properties of Organic Electrochemical Transistors. *ACS Appl. Mater. Interfaces* **2010**, *2* (6), 1637–1641.

(25) ElMahmoudy, M.; Inal, S.; Charrier, A.; Uguz, I.; Malliaras, G. G.; Sanaur, S. Tailoring the Electrochemical and Mechanical Properties of PEDOT:PSS Films for Bioelectronics. *Macromol. Mater. Eng.* **2017**, *302* (5), 1600497.

(26) Savagian, L. R.; Österholm, A. M.; Ponder Jr, J. F.; Barth, K. J.; Rivnay, J.; Reynolds, J. R. Balancing Charge Storage and Mobility in an Oligo (Ether) Functionalized Dioxythiophene Copolymer for Organic-and Aqueous-based Electrochemical Devices and Transistors. *Adv. Mater.* **2018**, *30* (50), 1804647.

(27) Giovannitti, A.; Rashid, R. B.; Thiburce, Q.; Paulsen, B. D.; Cendra, C.; Thorley, K.; Moia, D.; Mefford, J. T.; Hanifi, D.; Weiyuan, D. Energetic Control of Redox-Active Polymers toward Safe Organic Bioelectronic Materials. *Adv. Mater.* **2020**, 1908047.

(28) Wang, Y.; Zeglio, E.; Liao, H.; Xu, J.; Liu, F.; Li, Z.; Maria, I. P.; Mawad, D.; Herland, A.; Mcculloch, I.; et al. Hybrid Alkyl-Ethylene Glycol Side Chains Enhance Substrate Adhesion and Operational Stability in Accumulation Mode Organic Electrochemical Transistors. *Chem. Mater.* **2019**, *31* (23), 9797–9806.

(29) Sun, H.; Vagin, M.; Wang, S.; Crispin, X.; Forchheimer, R.; Berggren, M.; Fabiano, S. Complementary Logic Circuits Based on High-performance N-type Organic Electrochemical Transistors. *Adv. Mater.* **2018**, *30* (9), 1704916.

(30) Giovannitti, A.; Maria, I. P.; Hanifi, D.; Donahue, M. J.; Bryant, D.; Barth, K. J.; Makdah, B. E.; Savva, A.; Moia, D.; Zetek, M. The Role of the Side Chain on the Performance of N-Type Conjugated Polymers in Aqueous Electrolytes. *Chem. Mater.* **2018**, *30* (9), 2945–2953.

(31) Moser, M.; Savagian, L. R.; Savva, A.; Matta, M.; Ponder, J. F.; Hidalgo, T. C.; Ohayon, D.; Hallani, R.; Reisjalali, M.; Troisi, A.; et al. Ethylene Glycol-Based Side Chain Length Engineering in Polythiophenes and Its Impact on Organic Electrochemical Transistor Performance. *Chem. Mater.* **2020**, *32* (15), 6618–6628.

(32) Moser, M.; Hidalgo, T. C.; Surgailis, J.; Gladisch, J.; Ghosh, S.; Sheelamanthula, R.; Thiburce, Q.; Giovannitti, A.; Salleo, A.; Gasparini, N.; et al. Side Chain Redistribution as a Strategy to Boost Organic Electrochemical Transistor Performance and Stability. *Adv. Mater.* **2020**, *32* (37), 2002748.

(33) Nakahara, K.; Oyaizu, K.; Nishide, H. Organic Radical Battery Approaching Practical Use. *Chem. Lett.* **2011**, *40* (3), 222–227.

(34) Bobela, D. C.; Hughes, B. K.; Braunecker, W. A.; Kemper, T. W.; Larsen, R. E.; Gennett, T. Close Packing of Nitroxide Radicals in Stable Organic Radical Polymeric Materials. *J. Phys. Chem. Lett.* **2015**, *6* (8), 1414–1419.

(35) Rostro, L.; Wong, S. H.; Boudouris, B. W. Solid State Electrical Conductivity of Radical Polymers as a Function of Pendant Group Oxidation State. *Macromolecules* **2014**, *47* (11), 3713–3719.

(36) Oyaizu, K.; Ando, Y.; Konishi, H.; Nishide, H. Nernstian Adsorbate-like Bulk Layer of Organic Radical Polymers for High-Density Charge Storage Purposes. *J. Am. Chem. Soc.* **2008**, *130* (44), 14459–14461.

(37) Aqil, A.; Vlad, A.; Piedboeuf, M. L.; Aqil, M.; Job, N.; Melinte, S.; Detrembleur, C.; Jérôme, C. A New Design of Organic Radical Batteries (ORBs): Carbon Nanotube Buckypaper Electrode Functionalized by Electrografting. *Chem. Commun.* **2015**, *51* (45), 9301–9304.

(38) Wilcox, D. A.; Agarkar, V.; Mukherjee, S.; Boudouris, B. W. Stable Radical Materials for Energy Applications. *Annu. Rev. Chem. Biomol. Eng.* **2018**, *9*, 83–103.

(39) Rostro, L.; Galicia, L.; Boudouris, B. W. Suppressing the Environmental Dependence of the Open-Circuit Voltage in Inverted Polymer Solar Cells through a Radical Polymer Anodic Modifier. *J. Polym. Sci. Part B Polym. Phys.* **2015**, *53* (5), 311–316.

(40) Sung, S. H.; Bajaj, N.; Rhoads, J. F.; Chiu, G. T.; Boudouris, B. W. Radical Polymers Improve the Metal-Semiconductor Interface in Organic Field-Effect Transistors. *Org. Electron.* **2016**, *37*, 148–154.

(41) Joo, Y.; Agarkar, V.; Sung, S. H.; Savoie, B. M.; Boudouris, B. W. A Nonconjugated Radical Polymer Glass with High Electrical Conductivity. *Science (80-.).* **2018**, *359* (6382), 1391–1395.

(42) Gouras, P. Symposium on Electrophysiology: Electroretinography: Some Basic Principles. *Invest. Ophthalmol. Vis. Sci.* **1970**, *9* (8), 557–569.

(43) McCulloch, D. L.; Marmor, M. F.; Brigell, M. G.; Hamilton, R.; Holder, G. E.; Tzekov, R.; Bach, M. ISCEV Standard for Full-Field Clinical Electroretinography (2015 Update). *Doc. Ophthalmol.* **2015**, *130* (1), 1–12.

(44) Robson, A. G.; Nilsson, J.; Li, S.; Jalali, S.; Fulton, A. B.; Tormene, A. P.; Holder, G. E.; Brodie, S. E. ISCEV Guide to Visual Electrodiagnostic Procedures. *Doc. Ophthalmol.* **2018**, *136* (1), 1–26.

(45) Esakowitz, L.; Kriss, A.; Shawkat, F. A Comparison of Flash Electroretinograms Recorded from Burian Allen, JET, C-Glide, Gold Foil, DTL and Skin Electrodes. *Eye* **1993**, *7* (1), 169–171.

(46) Yin, H.; Pardue, M. T. Performance of the DTL Electrode Compared to the Jet Contact Lens Electrode in Clinical Testing. *Doc. Ophthalmol.* **2004**, *108* (1), 77–86.

(47) Allison, K.; Patel, D.; Alabi, O. Epidemiology of Glaucoma: The Past, Present, and Predictions for the Future. *Cureus* **2020**, *12* (11).

(48) Everitt, D. E.; Avorn, J. Systemic Effects of Medications Used to Treat Glaucoma. *Ann. Intern. Med.* **1990**, *112* (2), 120–125.

(49) Lieberman, E.; Stoudemire, A. Use of Tricyclic Antidepressants in Patients with Glaucoma: Assessment and Appropriate Perecautions. *Psychosomatics* **1987**, *28* (3), 145–148.

(50) Coleman, A. L.; Miglior, S. Risk Factors for Glaucoma Onset and Progression. *Surv. Ophthalmol.* **2008**, *53* (6), S3–S10.

(51) Tham, Y.-C.; Li, X.; Wong, T. Y.; Quigley, H. A.; Aung, T.; Cheng, C.-Y. Global Prevalence of Glaucoma and Projections of Glaucoma Burden through 2040: A Systematic Review and Meta-Analysis. *Ophthalmology* **2014**, *121* (11), 2081–2090.

(52) Leske, M. C.; Connell, A. M. S.; Wu, S.-Y.; Nemesure, B.; Li, X.; Schachat, A.; Hennis, A.; Group, B. E. S. Incidence of Open-Angle Glaucoma: The Barbados Eye Studies. *Arch. Ophthalmol.* **2001**, *119* (1), 89–95.

(53) Detry-Morel, M. Is Myopia a Risk Factor for Glaucoma? *J. Fr. Ophtalmol.* **2011**, *34* (6), 392–395.

(54) Marcus, M. W.; de Vries, M. M.; Montolio, F. G. J.; Jansonius, N. M. Myopia as a Risk Factor for Open-Angle Glaucoma: A Systematic Review and Meta-Analysis. *Ophthalmology* **2011**, *118* (10), 1989–1994.

(55) Tielsch, J. M.; Katz, J.; Sommer, A.; Quigley, H. A.; Javitt, J. C. Family History and Risk of Primary Open Angle Glaucoma: The Baltimore Eye Survey. *Arch. Ophthalmol.* **1994**, *112* (1), 69–73.

(56) Herndon, L. W.; Weizer, J. S.; Stinnett, S. S. Central Corneal Thickness as a Risk Factor for Advanced Glaucoma Damage. *Arch. Ophthalmol.* **2004**, *122* (1), 17–21.

(57) Moses, R. A. The Goldmann Applanation Tonometer. *Am. J. Ophthalmol.* **1958**, *46* (6), 865–869.

(58) Pakrou, N.; Gray, T.; Mills, R.; Landers, J.; Craig, J. Clinical Comparison of the Icare Tonometer and Goldmann Applanation Tonometry. *J. Glaucoma* **2008**, *17* (1), 43–47.

(59) Bochmann, F.; Kaufmann, C.; Thiel, M. A. Dynamic Contour Tonometry versus Goldmann Applanation Tonometry: Challenging the Gold Standard. *Expert Rev. Ophthalmol.* **2010**, *5* (6), 743–749.

(60) Yilmaz, I.; Altan, C.; Aygit, E. D.; Alagoz, C.; Baz, O.; Ahmet, S.; Urvasizoglu, S.; Yasa, D.; Demirok, A. Comparison of Three Methods of Tonometry in Normal Subjects: Goldmann Applanation Tonometer, Non-Contact Airpuff Tonometer, and Tono-Pen XL. *Clin. Ophthalmol. (Auckland, NZ)* **2014**, *8*, 1069.

(61) Asrani, S.; Zeimer, R.; Wilensky, J.; Gieser, D.; Vitale, S.; Lindenmuth, K. Large Diurnal Fluctuations in Intraocular Pressure Are an Independent Risk Factor in Patients with Glaucoma. *J. Glaucoma* **2000**, *9* (2), 134–142.

(62) Saccà, S. C.; Rolando, M.; Marletta, A.; Macrì, A.; Cerqueti, P.; Ciurlo, G. Fluctuations of Intraocular Pressure during the Day in Open-Angle Glaucoma, Normal-Tension Glaucoma and Normal Subjects. *Ophthalmologica* **1998**, *212* (2), 115–119.

(63) Medeiros, F. A.; Weinreb, R. N.; Zangwill, L. M.; Alencar, L. M.; Sample, P. A.; Vasile, C.; Bowd, C. Long-Term Intraocular Pressure Fluctuations and Risk of Conversion from Ocular Hypertension to Glaucoma. *Ophthalmology* **2008**, *115* (6), 934–940.

(64) Greene, M. E.; Gilman, B. G. Intraocular Pressure Measurement with Instrumented Contact Lenses. *Invest. Ophthalmol. Vis. Sci.* **1974**, *13* (4), 299–302.

(65) Yang, C.; Huang, X.; Li, X.; Yang, C.; Zhang, T.; Wu, Q.; Liu, D.; Lin, H.; Chen, W.; Hu, N. Wearable and Implantable Intraocular Pressure Biosensors: Recent Progress and Future Prospects. *Adv. Sci.* **2021**, *8* (6), 2002971.

(66) Todani, A.; Behlau, I.; Fava, M. A.; Cade, F.; Cherfan, D. G.; Zakka, F. R.; Jakobiec, F. A.; Gao, Y.; Dohlman, C. H.; Melki, S. A. Intraocular Pressure Measurement by Radio Wave Telemetry. *Invest. Ophthalmol. Vis. Sci.* **2011**, *52* (13), 9573–9580.

(67) Shih, Y.-C.; Shen, T.; Otis, B. P. A 2.3$\mu $ W Wireless Intraocular Pressure/Temperature Monitor. *IEEE J. Solid-State Circuits* **2011**, *46* (11), 2592–2601.

(68) Chen, G.-Z.; Chan, I.-S.; Leung, L. K. K.; Lam, D. C. C. Soft Wearable Contact Lens Sensor for Continuous Intraocular Pressure Monitoring. *Med. Eng. Phys.* **2014**, *36* (9), 1134–1139.

(69) Kim, J.; Kim, M.; Lee, M.-S.; Kim, K.; Ji, S.; Kim, Y.-T.; Park, J.; Na, K.; Bae, K.-H.; Kyun Kim, H. Wearable Smart Sensor Systems Integrated on Soft Contact Lenses for Wireless Ocular Diagnostics. *Nat. Commun.* **2017**, *8* (1), 1–8.

(70) Takahashi, H.; Dung, N. M.; Matsumoto, K.; Shimoyama, I. Differential Pressure Sensor Using a Piezoresistive Cantilever. *J. micromechanics microengineering* **2012**, *22* (5), 55015.

(71) An, H.; Chen, L.; Liu, X.; Zhao, B.; Zhang, H.; Wu, Z. Microfluidic Contact Lenses for Unpowered, Continuous and Non-Invasive Intraocular Pressure Monitoring. *Sensors Actuators A Phys.* **2019**, *295*, 177–187.

(72) Agaoglu, S.; Diep, P.; Martini, M.; Samudhyatha, K. T.; Baday, M.; Araci, I. E. Ultra-Sensitive Microfluidic Wearable Strain Sensor for Intraocular Pressure Monitoring. *Lab Chip* **2018**, *18* (22), 3471–3483.

(73) Yuan, M.; Das, R.; McGlynn, E.; Ghannam, R.; Abbasi, Q. H.; Heidari, H. Wireless Communication and Power Harvesting in Wearable Contact Lens Sensors. *IEEE Sens. J.* **2021**, *21* (11), 12484–12497.

(74) Sakintuna, B.; Lamari-Darkrim, F.; Hirscher, M. Metal Hydride Materials for Solid Hydrogen Storage: A Review. *Int. J. Hydrogen Energy* **2007**, *32* (9), 1121–1140.

3. RADICAL POLYMER-BASED ORGANIC ELECTROCHEMICAL TRANSISTORS*

3.1 Abstract

Organic electrochemical transistors (OECTs) are an emerging platform for bioelectronic applications. Significant effort has been placed in designing advanced polymers that simultaneously transport both charge and ions (i.e., macromolecules that are mixed conductors). However, the considerations for mixed organic conductors are often different from the established principles that are well-known in the solid-state organic electronics field; thus, the discovery of new OECT macromolecular systems is highly desired. Here, we demonstrate a new materials system by blending a radical polymer (i.e., a macromolecule with a nonconjugated backbone and with stable open-shell sites at its pendant group) with a frequently used conjugated polymer. Specifically, poly(4-glycidyloxy-2,2,6,6-tetramethylpiperidine-1-oxyl) (PTEO) was blended with poly(3-hexylthiophene) (P3HT) to create thin films with distinct closed-shell and open-shell domains. Importantly, the sharp and unique oxidation-reduction (redox) potential associated with the radical moieties of the PTEO chain provided a distinct actuation feature to the blended films that modulated the ionic transport of the OECT devices. In turn, this led to controlled regulation of the doping of the P3HT phase in the composite film. By decoupling the ionic and electronic transport into two distinct phases, and by using an ion transport phase with well-controlled redox activity, never-before-seen performance for a P3HT-based OECT was observed. That is, at loadings as low as 5% PTEO (by weight) OECTs achieved figure-of-merit (i.e., μC*) values > 150 F V^{-1} cm^{-1} s^{-1}, which places the performance on the same order as state-of-the-art conjugated polymers despite the relatively common conjugated macromolecular moiety implemented. As such, this effort presents a design platform by which to readily create tailored OECT response through strategic macromolecular selection and polymer processing.

* Reprinted with permission from Kim, H. J.; Perera, K.; Liang, Z.; Bowen, B.; Mei, J.; Boudouris, B. ACS Macro Lett. **2022**,11 (2), 243–250. Copyright 2022 American Chemical Society.

3.2 Introduction

An increasing demand for effective diagnostics systems has propelled the development and advancement of bioelectronic devices and biosensors.[1–3] Organic semiconductors that readily allow for mixed electronic and ionic conduction have been major catalysts for progress in the flexible and intrinsically stretchable biosensors community due to their low cost, biocompatibility, and mechanically robust behavior relative to their inorganic counterparts.[4–8] Specifically, organic electrochemical transistors (OECTs) have garnered considerable attention as active sensing components across various applications, including biomolecular sensors,[9,10] cellular sensors,[11,12] and neural interface devices.[13–15] The most oft-employed mixed conductor among conjugated polymers is the blend of poly(3,4-ethylenedioxythiophene) doped with poly(styrene sulfonate) (PEDOT:PSS). Many desirable qualities, including high conductivity, water processability, and commercial availability, have motivated scientists and engineers to readily employ PEDOT:PSS in multiple systems.[3,16–24] Although there is still significant excitement surrounding PEDOT:PSS, this polymer blend is not without a few shortcomings. For instance, PEDOT:PSS OECTs typically operate in depletion mode, which means that a high (hole) current flows through the channel in the absence of a gate bias. This can potentially raise concerns for its use in lab-on-a-chip bioelectronics where form factors and energy storage unit (e.g., battery) dimensions are necessarily restricted. PEDOT:PSS also has a Young's modulus significantly higher than that of biological tissue, which could limit future implantable bioelectronics application, although clever molecular design strategies regarding the PSS moiety have addressed this concern to some degree.[25,26] In addition, PEDOT:PSS has a complex macromolecular structure that is altered in an ill-defined manner through a variety of solvent processing techniques.[27–30] As such, site-to-site variabilities in its performance have been observed, and this limits its use as a model system in the pursuit of expanding a general understanding of the underlying structure-property relationships involved in OECTs.

To address this opportunity, different molecular design strategies have been developed for alternative high-performance OECT active layers.[31–33] The majority of the design motifs and principles employed in synthesizing OECT materials is inherited from related organic electronic materials platforms, including the principles developed during the rise of polymers for organic field-effect transistors (OFETs). Various backbone chemistries, including propylenedioxythiophene (ProDOT),[34] diketopyrrolopyrrole (DPP),[35] isoindigo,[36] and

naphthalene-1,4,5,8-tetracarboxylic-diimide (NDI),[37,38] have led to the successful syntheses of OECT materials. However, unlike in OFETs, where heavy focus is placed on the crystallinity of OFET materials to improve the charge carrier mobility, the volumetric capacitance (C*) of the film is paramount in improving the OECT performance to facilitate dopant ion injection.[4,5,39] Therefore, functionalizing the conjugated backbones of these designer polymers with ethylene glycol (EG) pendant groups is one of the most common and powerful design approaches to boost their volumetric capacitance.[34,40] For instance, OECT materials made from poly(2-(3,3′-bis(2-(2-(2-methoxyethoxy)ethoxy)ethoxy)-[2,2′-bithiophen]-5-yl)thieno[3,2-b]thiophene) p(g2T-TT) and its derivatives have exhibited figure-of-merit μC* [i.e., the product of charge mobility (μ) and volumetric capacitance (C*)] values > 500 F V^{-1} cm^{-1} s^{-1}.[41] In this way, much success has been achieved in both elucidating the fundamental mechanism of operation and in application fronts using these PEGylated conjugated polymers; however these design motifs are also limited in the number of chemistries that have been evaluated.[8]

An alternative class of soft materials, radical polymers (i.e., macromolecules with nonconjugated backbones and with stable open-shell groups at their pendant sites), have gained increasing attention in organic electronics applications.[42–51] The redox-active pendant groups of radical polymers can be oxidized and/or reduced to form their closed-shell analogs (i.e., the ionic species), enabling solid-state charge transport.[52–55] Their high theoretical capacities (>100 mAh g^{-1}) and fast redox reactions have motivated the use of these materials as active components in organic batteries.[42,47,56–59] To date, however, radical polymers have been rarely evaluated as the main component in other organic electronics platforms aside from organic battery materials. Among the limiting factors preventing radical polymers from being explored in other applications is their generally low electrical conductivity.[60] To this end, conjugated radical polymers (CRPs) have been designed with an aim of improved electronic conductivity.[61] Interestingly, when two distinct redox active moieties with different potentials are present in the electrochemical system an internal charge transfer between these chemistries is observed.[62–64] The relative redox potential of the conjugated backbone and the pendant radical dictate in which order these redox active moieties are oxidized and reduced. The studies on CRPs suggest the potential usefulness of the stable radicals as a voltage regulator with which to tune ion injection to a desired potential. One particularly attractive way to introduce radical moieties is blending the two polymers to create distinct polymer phases when they are cast as thin films. Blending

two different polymers for electronic conduction and ionic conduction allows facile decoupling of mixed conduction and therefore can serve as a platform to understand the underlying structure-property relationship for mixed conductors.[65–68] This strategy allows for strategic placement of the redox-active stable radicals to the ion conducting pathway and, therefore, controlling the ion infiltration based on their redox states.

Here, we incorporate a radical moiety into OECT active layers by blending poly(4-glycidyloxy-2,2,6,6-tetramethylpiperidine-1-oxyl) (PTEO) as the primary ion conductor and poly(3-hexylthiophene) (P3HT) as the primary charge conductor (Figure 3.1a). P3HT is an oft-used polymeric semiconductor whose overall structure-property relations are well-developed. PTEO, with a hydrophilic, poly(ethylene oxide)-like (PEO-like) backbone and pendant 2,2,6,6-tetramethylpiperidine 1-oxyl (TEMPO) radicals. On the other hand, the PTEO thin film showed prominent redox peaks characteristic of the TEMPO radicals with the oxidation peak located at +0.74 V (vs. Ag/AgCl).[73,74] PTEO, with a hydrophilic, poly(ethylene oxide)-like (PEO-like) backbone and pendant 2,2,6,6-tetramethylpiperidine 1-oxyl (TEMPO) radicals (Scheme 3.1, Figure 3.2, and Figure 3.3), which serves as a pathway for hydrated ion transport that serves as a dopant for the P3HT phase. Electrochemical analyses of the blend films revealed that ion injection into the blend film was indeed controlled by the TEMPO redox profile. Specifically, the presence of the TEMPO moiety caused the threshold voltage (V_T) to shift during OECT operation. By tuning the composition of the blend, a high μC^* of 151 ± 7 F V^{-1} cm^{-1} s^{-1} was achieved for the 5% PTEO (by weight) OECT, the highest reported to date among P3HT-based OECTs and on the same order of magnitude as state-of-the-art OECT materials working in an accumulation mode.[5,66,69] Further increasing the PTEO weight loading improved the response kinetics while decreasing the steady-state performance, suggesting that polymer composition plays an important role in tuning the film morphology to tailor the two metrics for a desired application. The complex internal transfer mechanism observed in the CRPs was not observed in the blend films, suggesting that our approach may be extended to a variety of conjugated polymers and radical polymers which can be synthesized in a rather straightforward manner. Therefore, our findings motivate incorporation of redox-active radicals as a threshold voltage regulator in designing next-generation, high-performance organic mixed conductors that are independent of the chemistry of the conjugated polymer matrix.

3.3 Materials and Methods

3.3.1 Materials

All chemicals were purchased from Sigma-Aldrich, and they were used as received unless otherwise stated. Poly(3-heyxlthiophene) (P3HT) (M_w ~36.6 kg mol^{-1}; 95.2% regioregularity) was purchased from Ossila Ltd. Glass wafers were purchased from Mark Optics.

3.3.2 Synthesis of 4-glycidyloxy-2,2,6,6-tetramethylpiperidine-1-oxyl (TEO)

PTEO was synthesized according to the literature with minor modifications.[60,70–72] For the synthesis of the TEO monomer, 8.25 g of 4-hydroxy-2,2,6,6-tetramethylpiperidin-*N*-oxy (TEMPO-OH) dissolved in THF (at a concentration of 275 mg mL^{-1}) were added dropwise into the mixture containing 20 mL of epichlorohydrin, 3 g of tetrabutylammonium hydrogen sulfate (TBAHS), and aqueous sodium hydroxide (28 mL of total volume where it was 50% NaOH, by weight). The resulting mixture was stirred at room temperature for 16 h. After the reaction, the mixture was poured into 200 mL of water. The product was extracted with ethyl acetate, washed with deionized water three times, and dried with anhydrous magnesium sulfate. The monomer was dried, and it was further purified using a silica gel column chromatography (hexane:ethyl acetate = 8:1, v/v). The monomer was recovered as needle-shaped red crystals, when the temperature was at or below room temperature, and it was stored in inert atmosphere until further use.

3.3.3 Synthesis of Poly(4-glycidyloxy-2,2,6,6-tetramethylpiperidine-1-oxyl) (PTEO)

The polymerization of TEO into PTEO was carried out by adding 1 g of TEO into a mixture containing 0.3 mL of diglyme, 102 µL of 1 M potassium *tert*-butoxide in THF, and 80 mg of 1,4,7,10,13,16-hexaoxacyclooctadecane (18-crown-6 ether) in a glass vial. The resulting mixture was then heated at 40 °C and stirred for 40 h in an inert atmosphere. After cooling to room temperature, 200 mL of dichloromethane was added to the reaction mixture, and the organic solution was washed with water three times and dried with anhydrous magnesium sulfate. The organic phase was concentrated to 5 mL of solvent and then precipitated in hexanes. The PTEO was stored inside N_2-filled glovebox prior to use.

3.3.4 Electrochemical Characterization

All electrochemical analyses were carried out using 0.1 M NaCl in ultrapure (18.2 MΩ·cm) water. The cyclic voltammetry (CV) measurements were performed using a three-electrode set-up with Ag/AgCl as the reference electrode, a platinum coil as the counter electrode, and gold as the working electrode with an active area of 10 mm^2 on a VersaSTAT 3 Workstation. The voltage was swept from −0.1 V to +0.9 V relative to the reference electrode. The spectroelectrochemical measurements were recorded using a custom-built system combining a Biologic SP-150 potentiostat and an Agilent Cary 5000 UV/Vis-NIR spectrophotometer, and tin-doped indium oxide-coated (ITO-coated) glass was used as the working electrode.

3.3.5 Surface Characterization

Atomic force microscopy (AFM) images were acquired with a Veeco Dimension 3100 atomic force microscope operating in tapping mode. The probe tips were fabricated by Budgetsensors (Tap150AI-G), and they had a resonant frequency of 150 kHz and a force constant of 5 N m^{-1}.

3.3.6 OECT Device Fabrication and Characterization

OECT devices were fabricated following previously reported processes with minor adjustments.[20] Briefly, the Ti/Au electrodes were patterned on a glass substrate using photolithography using LOR 3A and AZ1518 bilayer resists. Two 1 µm-thick Parylene C (PaC) conformal coatings were deposited using the SCS Labcoater (PDS 2010) with A-174 silane and 1.5% Micro-90 aqueous solution as an adhesion promoter between the first PaC layer and the glass and as an anti-adhesion promoter between PaC layers, respectively. The PaC layers were patterned with a reactive ion etcher (March Jupiter II) using photolithographically patterned AZ9260 photoresist mask to expose the active channel area. Polymer solutions were prepared by mixing stock solutions of PTEO and P3HT dissolved in chloroform at predetermined ratios. PTEO-OH was prepared by quenching PTEO with a phenyl hydrazine solution overnight. For the OECT characterization of the P3HT-PTEO-OH films, 1% (by weight) 3-glycidoxypropyltrimethoxysilane (GOPS) was added to prevent dissolution of PTEO-OH during OECT operation. The polymer thin films were deposited using a spin coater by coating at 2,000

rpm for 60 s. Then, the second layer of PaC was removed, and the devices were rinsed with water. Device performance measurements were carried out with a three-point geometry on a Keysight B2902A sourcemeter where 200 µL of 0.1 M aqueous NaCl was drop cast on top of the channel to serve as the electrolyte. A pellet-type Ag/AgCl reference electrode (E205, Warner Instruments) was used as gate electrode immersed in the electrolyte. The transconductance of the device (gm) was extracted by taking the first derivative of the drain current-gate voltage (I_D-V_G) transfer curves and normalizing these data using the channel dimensions.

3.4 Results and Discussion

3.4.1 Electrochemical Analysis

To determine how the electrochemical activity of the polymeric film in aqueous media is altered upon polymer blending, cyclic voltammetry (CV) measurements were acquired (Figure 3.1a). We first evaluated pristine P3HT and PTEO films to compare their electrochemical activity in aqueous media. A highly regioregular (i.e., > 90 % head-to-tail couplings) P3HT film showed a trivial electrochemical activity where the activity is likely only at the electrolyte-polymer interface. This is attributed to the relatively high crystallinity and the hydrophobic nature of the semiconducting polymer, which inhibits penetration of highly hydrated chloride anions.[69]

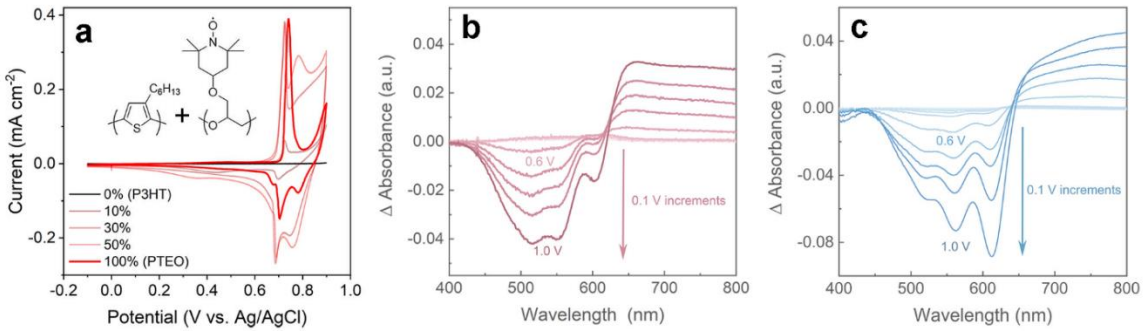

Figure 3.1 (a) Cyclic voltammetry of the P3HT-PTEO films of select blend ratios ranging from 0% (P3HT, black) to 100% (PTEO, red) acquired at a scan rate of 25 mV s^{-1}. The voltammograms of pristine P3HT and PTEO thin films are highlighted. The inset image shows chemical structures of P3HT and PTEO. Absorbance changes recorded upon electrochemical biasing for (b) a neat P3HT film and (c) a thin film containing equal weight fractions of P3HT and PTEO. The spectra are plotted with the neutral polymer as the reference.

On the other hand, the PTEO thin film showed prominent redox peaks characteristic of the TEMPO radicals with the oxidation peak located at +0.74 V (vs. Ag/AgCl).[73,74] PTEO has a hydrophilic, PEO-like backbone, which promotes the penetration of hydrated chloride anions into the polymer film upon biasing.[69]

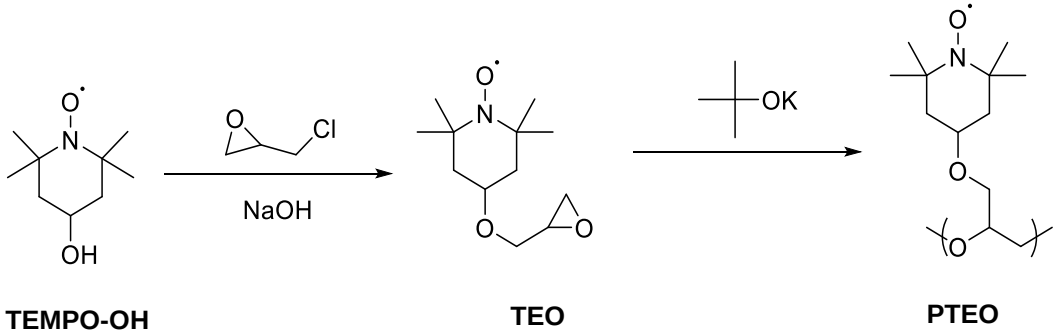

Scheme 3.1. Synthetic route for the creation of PTEO.

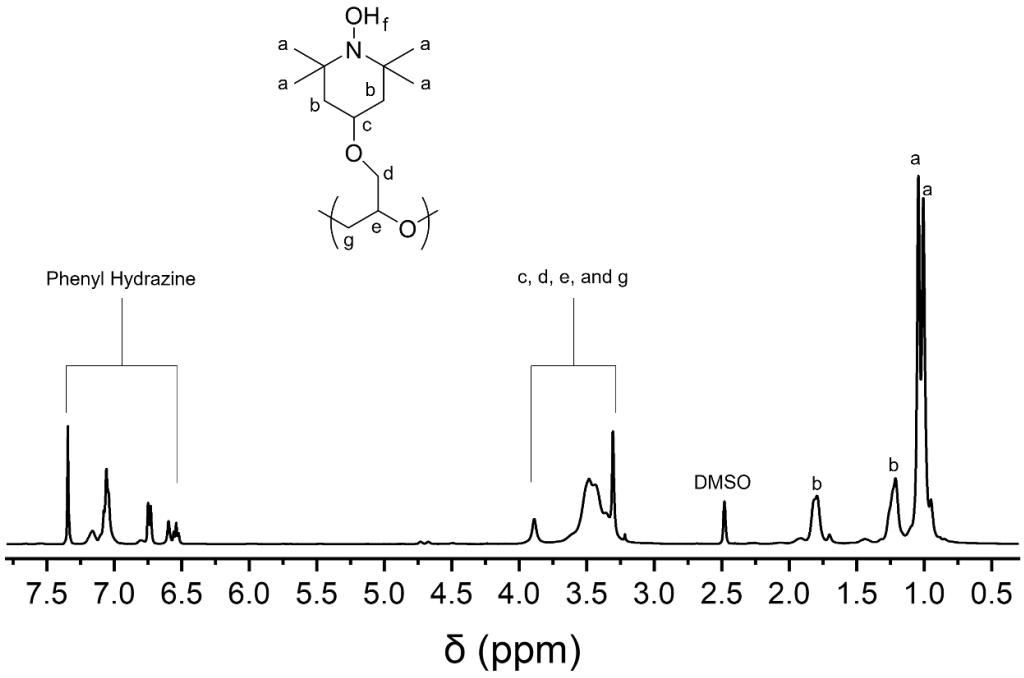

Figure 3.2.[1]H NMR spectrum of PTEO quenched with phenyl hydrazine. Deuterated DMSO was used as solvent.

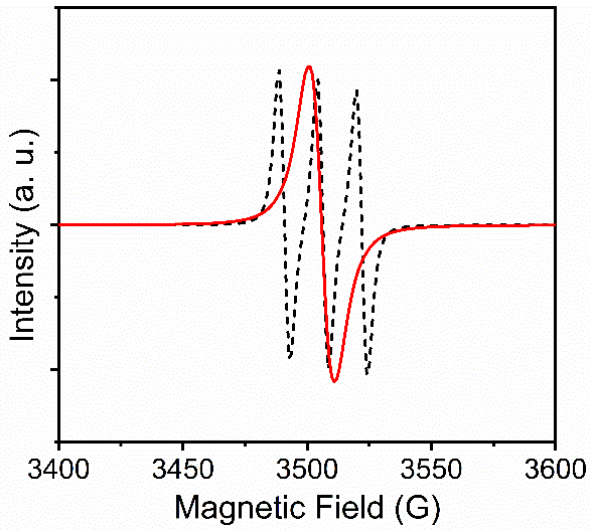

Figure 3.3. EPR spectra of the starting reagent, TEMPO-OH (black dashed line), and PTEO (red solid line) in chloroform. The final radical density of PTEO with respect to TEMPO-OH was 95% of the total possible repeat units.

Next, we examined the interaction of the two redox sites in the blend films (Figure 3.4). The characteristic peaks of the TEMPO radicals emerged at loadings as low as 2.5% PTEO, by weight. As the PTEO loading was increased, another oxidation peak at +0.78 V (vs. Ag/AgCl), corresponding to oxidation of P3HT, was also observed in the films of >30% PTEO (by weight), which indicates improved ion injection through the PTEO phase and enhanced electrochemical activity of the P3HT domains because of increased PTEO content in the thin films. Notably, the TEMPO oxidation peaks were slightly shifted to a lower potential of +0.72 V. We reason that the slight reduction in the TEMPO oxidation potential is associated with the improved packing density of PTEO in the blended matrix. Cyclic voltammetry scans of the 80% PTEO (by weight) blend film revealed splitting of the TEMPO oxidation peak into two distinct peaks at +0.71 V and +0.73 V, corresponding to TEMPO oxidation peaks in the blended matrix and in the PTEO-rich domains, respectively (Figure 3.5). These findings support the idea that the TEMPO redox sites present in the ion-conducting domain (i.e., the PTEO phase) can act as an ion injection trigger to allow doping of the organic active layer for mixed conduction applications.

Spectroelectrochemical measurements of pristine P3HT (Figure 3.1b) and PTEO-containing blend films (Figure 3.1c) further validate the role of PTEO in enhancing the electrochemical doping of P3HT. Changes in the absorption profile upon biasing can be directly attributed to P3HT doping, because the visible light absorption of PTEO thin films is extremely

small relative to that of P3HT. The absorbance of the P3HT films show maximum absorbances at 515 nm (λ_{max}) and two slight shoulders at 550 nm and 600 nm (Figure 3.6), consistent with previous reports.[69,75] As the oxidation potential applied to the film exceeds +0.5 V (vs Ag/AgCl), absorbance in the visible region gradually decreases, while absorbance in the near infrared (NIR) wavelength regime increases, indicating the loss of neutral segments within the polymer and the formation of polarons along the macromolecular chain, respectively. These changes are represented in the form of a difference spectrum with respect to the neutral polymer film for improved clarity. The small changes in the absorbance spectra in Figure 3.1b confirm the low degree of doping, presumably confined to the polymer-electrolyte interface for the pristine P3HT thin film.

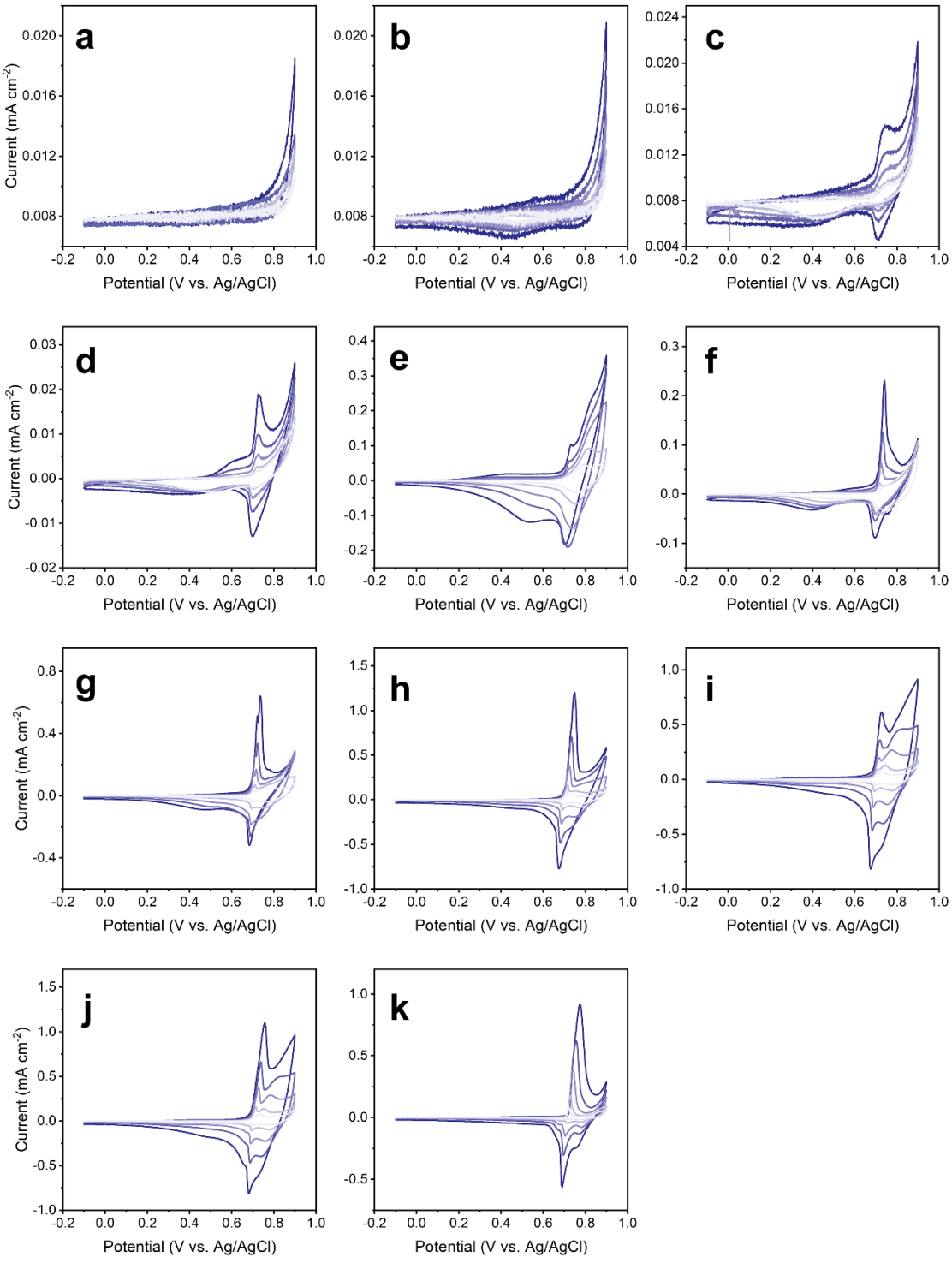

Figure 3.4. Cyclic voltammograms of the polymer blends containing PTEO weight percentages of: (a) 0% (i.e., pristine P3HT), (b) 1%, (c) 2.5%, (d) 5%, (e) 7.5%, (f) 10%, (g) 20%, (h) 30%, (i) 40%, (j) 50%, and (k) 100 % (i.e., pristine PTEO) at scan rates of 5, 10, 25, 50, and 100 mV s^{-1}. Here, the darker the line color indicates an increasing scan rate.

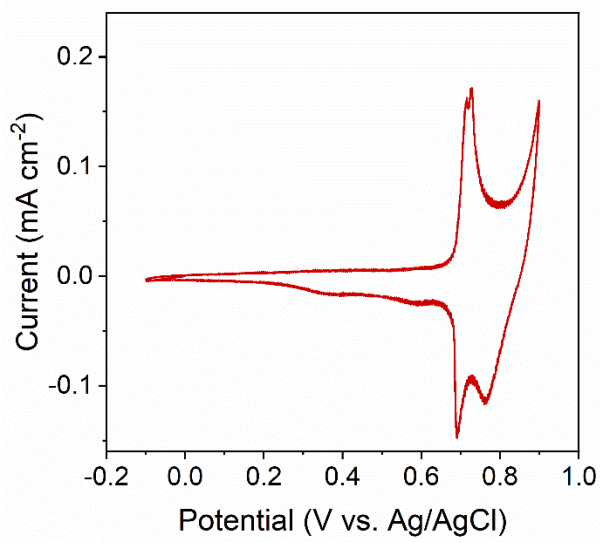

Figure 3.5. Representative cyclic voltammogram of an 80% PTEO (by weight) thin film where the sweeping rate was 25 mV s-1.

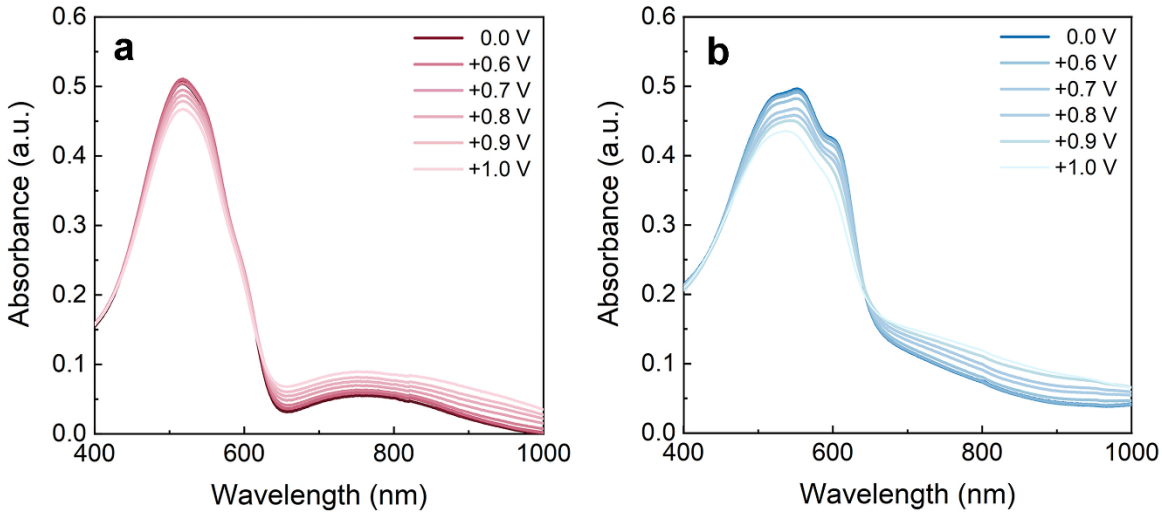

Figure 3.6. Absorbance spectra of (a) a P3HT thin film and (b) a thin film containing 5% PTEO (by weight) in 0.1 M NaCl(aq) with varying applied potentials ranging from 0 V to +1 V (vs. Ag/AgCl).

In contrast, blend films with equal proportions of P3HT and PTEO, exhibit enhanced doping at similar potentials (Figure 3.1c). While little difference is observed between the onset potential for P3HT doping in both neat and blend films, the blend films show increases in the extent of electrochemical doping at each potential step once the doping threshold is surpassed.

Another key feature is the influence of the radical polymer on P3HT aggregation, as revealed from the absorbance profile of the undoped P3HT-PTEO blend film. The presence of the polar PEO-like chains of PTEO induces planarity of P3HT polymer chains and increases intra-chain exciton coupling, as shown by the red-shifted absorbance spectrum and the high $A_{0\text{-}0}/A_{0\text{-}1}$ peak ratio, respectively. Similar phenomena have been previously reported in P3HT and other conjugated polymers blended with PEO-like polar polymers.[76–79] The red-shifted absorbance onset of the torsionally ordered P3HT overlaps with the polaron band in the electrochemically doped-blend films, obscuring clear distinction of the polaron band. These observations provide insights on the effect of blending PTEO on the physicochemical and electrochemical properties of P3HT.

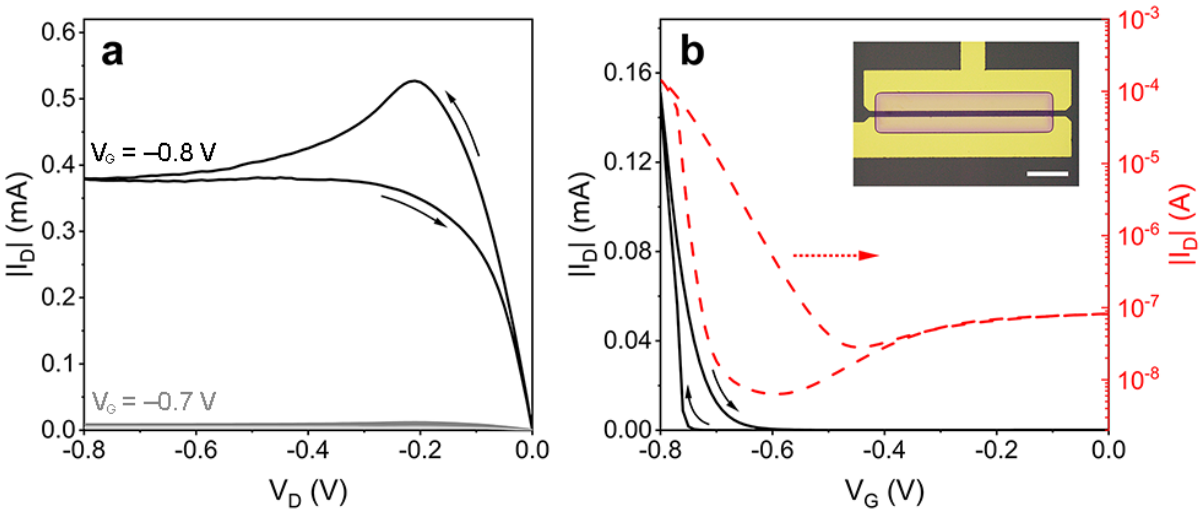

Figure 3.7. (a) Representative forward and reverse output curves of the 5% PTEO (by weight) blend OECT using 0.1 M NaCl aqueous electrolyte and a pellet-type Ag/AgCl reference electrode. The voltage values correspond to the gate voltage values at which the measurements occurred. (b) The transfer curve was recorded with V_D = –0.8 V. All measurements were taken with a scan rate of 10 mV s^{-1}. The red curve in panel (b) are the same data as the black curve of panel (b); however, they are plotted on a logarithmic axis to highlight the ON/OFF ratio of the OECT. The inset of panel (b) shows an optical microscopic image of an OECT channel where the scale bar represents 100 µm.

3.4.2 Steady-state OECT Device Characterization

Both output and transfer characterization measurements of the P3HT-PTEO blend transistors showed large current modulation, whose magnitudes were consistent with OECT accumulation mode operation (Figure 3.7). While the output current profile in the reverse sweep

resembled that of a typical electrolyte-gated organic field effect transistor (EGOFET) consisting of a saturation region followed by a linear region, the forward sweep showed the current rise above what would be considered a saturation regime current. The gate-source current (I_G) was recorded to ensure that that this unusual profile was not the result of the leak current, and this was confirmed with a much smaller magnitude of the I_G (Figure 3.8). Moreover, the location of this peak in the forward sweep coincides with the oxidation of the TEMPO radical in the corresponding I_G curve (Figure 3.9).

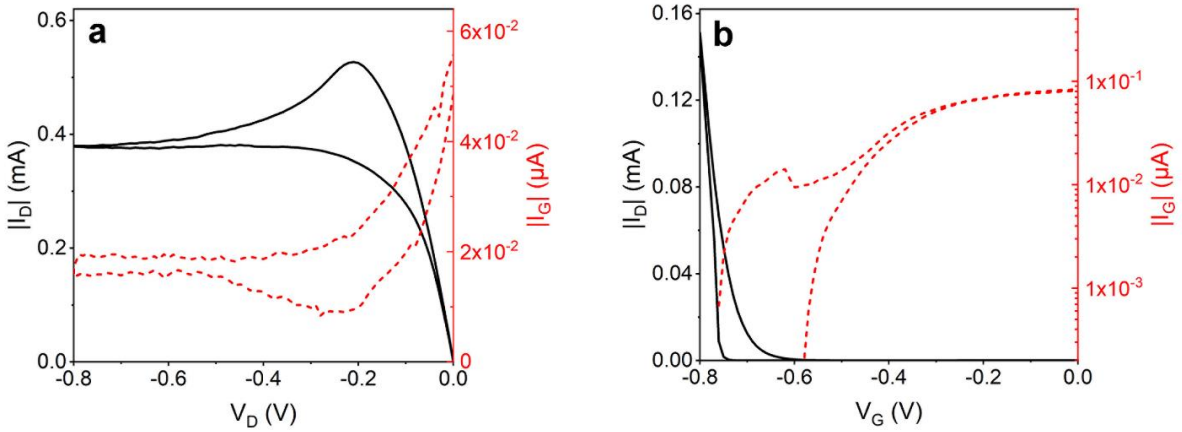

Figure 3.8. I_D (black, left axis) and I_G (red, right axis) as a function of (a) drain voltage (V_G = –0.8 V) and (b) gate voltage (V_D = –0.8 V) for 5% PTEO (by weight) OECT thin films.

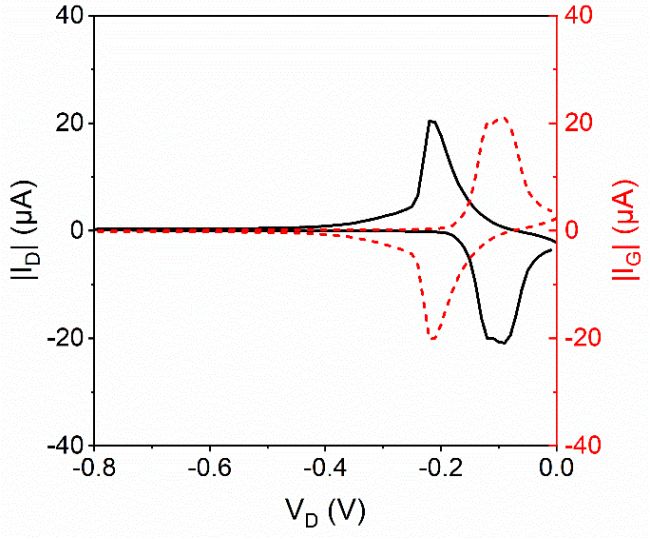

Figure 3.9. Output curve of pristine PTEO OECT at a gate voltage of V_G = −0.8 V. The I_D (black, left axis) and the I_G (red, right axis) were equal in magnitude but opposite in direction, suggesting the recorded current was due to ionic conduction.

The threshold voltage (V_T) in the forward sweep also coincides with the oxidation onset of TEMPO radical, giving rise to an extremely steep current modulation in the forward sweep with a high ON/OFF ratio of ~10^4 (Figure 3.7b). As observed in the CV traces, while P3HT has a higher oxidation peak potential than PTEO, typical current modulation starts to emerge at lower gate voltages than observed for the blend.[80] The incorporation of TEMPO moieties into the P3HT channel, on the other hand, suppresses the current modulation at lower V_G. The recorded I_D below the onset potential for the TEMPO radical oxidation (V_G = −0.7 V) was significantly lower than that under V_G = −0.8 V. More importantly, the characteristic peak in the forward sweep was absent. This serves as strong indication that the V_T is governed by the presence of a radical moiety, and the presence of the redox-active radicals can act as a trigger for ion injection for mixed conduction applications.

The effect of the blend composition on the OECT performance was probed by recording transfer curves of P3HT-PTEO blends over a range of PTEO loadings with the specific information for each polymer blend composition summarized in Table 3.1.

Table 3.1. OECT Steady-state Performance and Film Thickness at Various PTEO Loadings.

PTEO weight loading (%)	g_m (mS)[1]	d (nm)[2]	μC* (F cm^{-1} V^{-1} s^{-1})	V_T (V)
0	0.15 ± 0.03	50 ± 1	7.6 ± 1.3	-0.62
1	0.16 ± 0.04	50 ± 2	8.1 ± 1.5	-0.62
2.5	0.3 ± 0.09	51 ± 2	15 ± 4	-0.71
5	3.1 ± 0.1	51 ± 2	151 ± 7	-0.72
7.5	2.8 ± 0.1	52 ± 2	135 ± 7	-0.72
10	2.8 ± 0.2	62 ± 2	113 ± 8	-0.73
20	3.5 ± 0.2	89 ± 5	97 ± 9	-0.73
30	3.2 ± 0.3	90 ± 5	90 ± 10	-0.73
40	3.1 ± 0.4	98 ± 8	80 ± 12	-0.72
50	3.7 ± 0.7	152 ± 14	61 ± 13	-0.72

[1] *The reported values represent the average and error across three distinct devices.*
[2] *The film thickness, as determined using profilometry.*

The figure-of-merit (μC*) was extracted using the following equation derived from the Bernards Model.[81]

$$\mu C^* = \frac{L}{Wd}\frac{g_m}{(V_g - V_T)} = \frac{L}{Wd}\frac{1}{(V_g - V_T)}\frac{\partial I_D}{\partial V_G}$$

Here, L, W, and d represent the active channel area dimensions: the channel length, width, and thickness, respectively. The μC* values were extracted and plotted against the blend composition (Figure 3.10a). The figure of merit for the pristine P3HT OECT devices was 7.6 ± 1.3 $F\,V^{-1}\,cm^{-1}\,s^{-1}$, on the same order of magnitude as previous reports.[69] As the PTEO loading was varied, the μC* slowly rose in magnitude until drastically increasing at a loading of 5%, by weight. The highest μC* was observed at the 5% PTEO (by weight) blend, with a value of 151 ± 7 $F\,V^{-1}\,cm^{-1}\,s^{-1}$, which is the highest reported value for P3HT-containing OECTs.[75,82,83] To further examine the impact of the TEMO radicals, P3HT blended with quenched PTEO (i.e., PTEO-OH) was also tested in the OECT setup (Figure 3.11 and Table 3.2). Here only a slight increase in to 13 ± 2.6 $F\,V^{-1}\,cm^{-1}\,s^{-1}$ was observed at 10% (by weight) PTEO-OH. The discrepancy in the metrics suggests the redox activity TEMPO radicals increases the overall OECT performance. One contributing factor in this drastic improvement was the difference between the operating V_G and V_T of the blend active layer. The introduction of PTEO into the P3HT active layer shifted the apparent V_T from −0.62 V (0%) to −0.72 V (7.5%) in the blended OECTs (Figure 3.10b). In contrast, the apparent V_T converged to a lower value of −0.42 V for P3HT/PTEO-OH OECTs. We note that the threshold voltage values determined from the transfer curves are slightly higher than the onset potential of the corresponding blend films observed in the CV traces.[69] Although the V_T of the blend film is rather high, this sharp onset is an appealing feature for transistor-type device whose main function is to serve as a switch. As more PTEO was added to the blend, however, a gradual reduction in the μC* was observed. This could be reasoned with the idea that the overall hole mobility decreased in the blend film, and this outweighed the volumetric capacitance contribution.

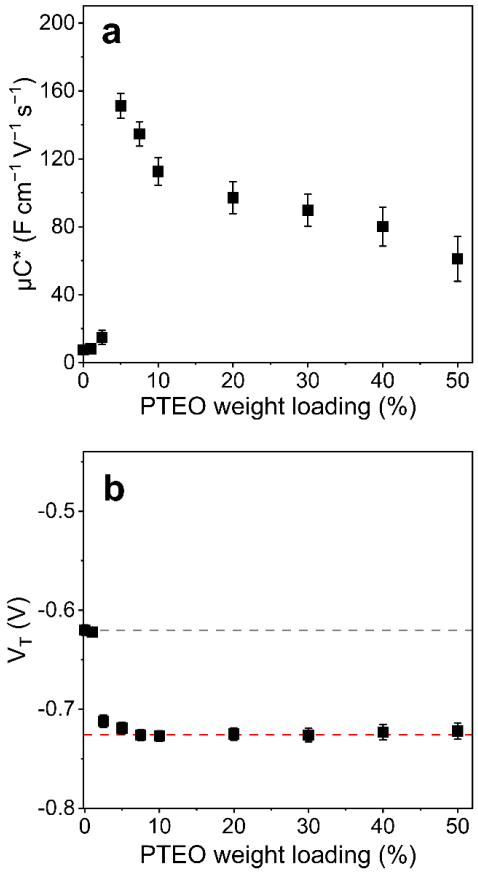

Figure 3.10. (a) Calculated μC* as a function of PTEO loading as extracted from respective transfer curves. The figure-of-merit peaked at 5% with the value of 151 ± 7 $F\,V^{-1}\,cm^{-1}\,s^{-1}$, followed by a decaying plateau at moderate loadings. (b) A shift in the threshold voltage V_T was observed at values as low as 2.5% PTEO (by weight) in the blend films, converging to about −0.72 V at loadings of ≥ 7.5% PTEO (by weight) in the thin film. The data were averaged over three separate devices, and the error bars represent the values that are one standard deviation from that average value.

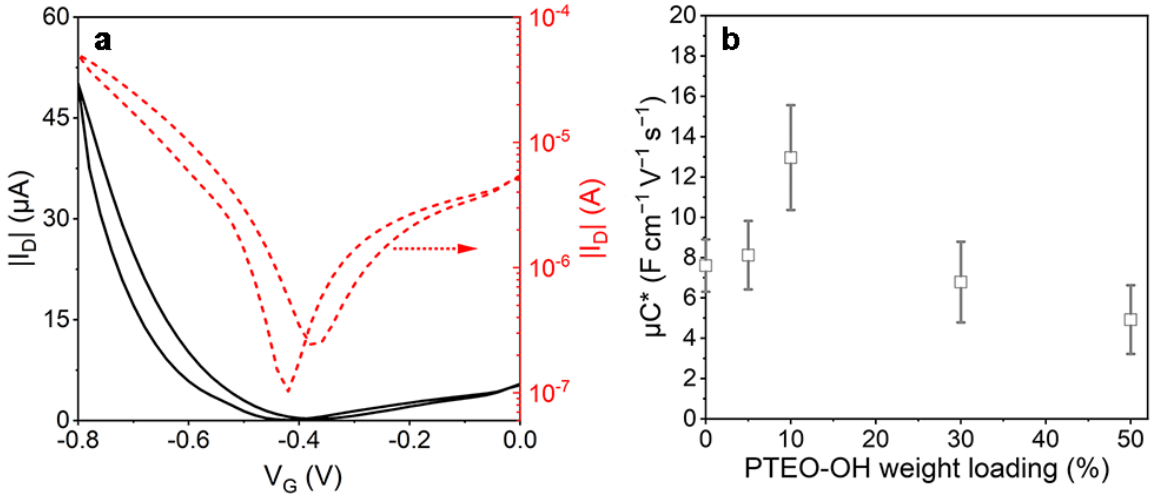

Figure 3.11. (a) Transfer curve recorded for a 5% PTEO-OH (by weight) OECT thin film at V_D = −0.8V. (b) Calculated μC* as a function of PTEO-OH loading as extracted from respective transfer curves. The data points represent the averaged values over three devices.

Table 3.2. OECT Steady-state Performance and Film Thickness at Various PTEO-OH Loadings.

PTEO-OH weight loading (%)	g_m (mS)[1]	d (nm)[2]	μC* (F cm^{-1} V^{-1} s^{-1})	V_T (V)
0	0.15 ± 0.03	50 ± 1	7.6 ± 1.3	-0.62
5	0.38 ± 0.08	52 ± 2	8.1 ± 1.7	-0.44
10	0.76 ± 0.15	62 ± 4	13 ± 2.6	-0.42
30	0.68 ± 0.21	106 ± 15	6.8 ± 2.0	-0.42
50	0.67 ± 0.12	142 ± 17	4.9 ± 1.7	-0.42

[1] *The reported values represent the average and error across three distinct devices.*
[2] *The film thickness, as determined using profilometry.*

3.4.3 Transient Behaviors of the Blended OECTs

The time-elapsed current responses of the blended OECTs were recorded by pulsing the gate voltage and comparing the transient response to the normalized I_D response; these data revealed that the response kinetics improved with an increasing PTEO weight loading (Figure 3.12a). At lower PTEO loadings (i.e., at values ≤ 7.5%, by weight), the I_D did not saturate at the end of the 200 s pulse. Conversely, when the amount of PTEO was increased, the normalized I_D achieved reached saturation. Another consequence of blending was a significant reduction in the switching delay from ~35 s for pristine P3HT to ~3 s for the blended device (Figure 3.12b) containing equal masses of PTEO and P3HT. This improved kinetic response is attributed to the increase in the ion percolating network (i.e., the PTEO weight loading), allowing higher flux of ions to dope P3HT backbones.

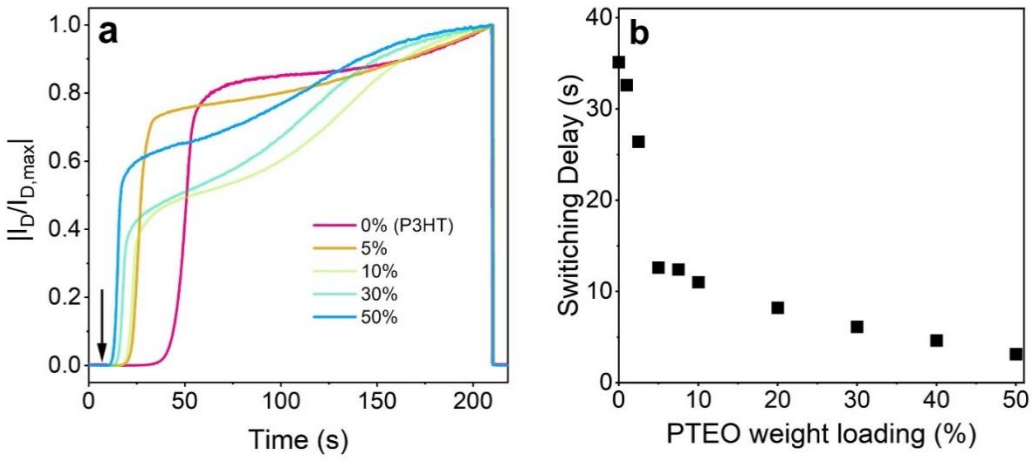

Figure 3.12. (a) Normalized transient responses with a V_G of −0.8 V sourced at t = 10 s for 200 s at a constant V_D = −0.8 V of the thin films showed that increasing the PTEO loading improved the overall transient kinetics of the blend OECTs. (b) The switching delay decreased inversely with increasing PTEO loading.

3.4.4 AFM Analysis of the P3HT-PTEO Films

To better correlate the inverse behavior regarding the steady-state performance and transient responses of the blend OECTs, the topographies of the blend films were imaged using atomic force micrography (AFM, Figure 3.13). As commonly seen, P3HT nanofibrils were observed in the pristine P3HT film (Figure 3.13a). When PTEO was blended with P3HT at 1% and 2.5% loadings (by weight), P3HT nanofibrils were still observed, but these fibrils decreased in both number and size as the PTEO blocked the crystallinity of the P3HT domains. In fact, these fibrils were observed up to the 5% blend film (Figure 3.13b). Based on the effect of blend ratio on the steady-state performance and the response kinetics, we put forward that the 5% blend represents the threshold loading of PTEO to establish a percolating structure throughout the blend film through which ions are transported easily to allow for doping of the P3HT. The decrease in μC* at 7.5% and higher loadings can be explained with the emerging phase separation in the two polymer domains (Figure 3.13c). Because PTEO showed little in terms of electrical current when swollen with aqueous electrolyte, the PTEO domain is primarily ionic conducting. Thus, hole transport is predominantly governed by the P3HT domains. As more PTEO was blended with P3HT, the PTEO domains grew both in number and size (Figure 3.13d). which would disrupt the connectivity of the P3HT domains and the overall hole mobility.

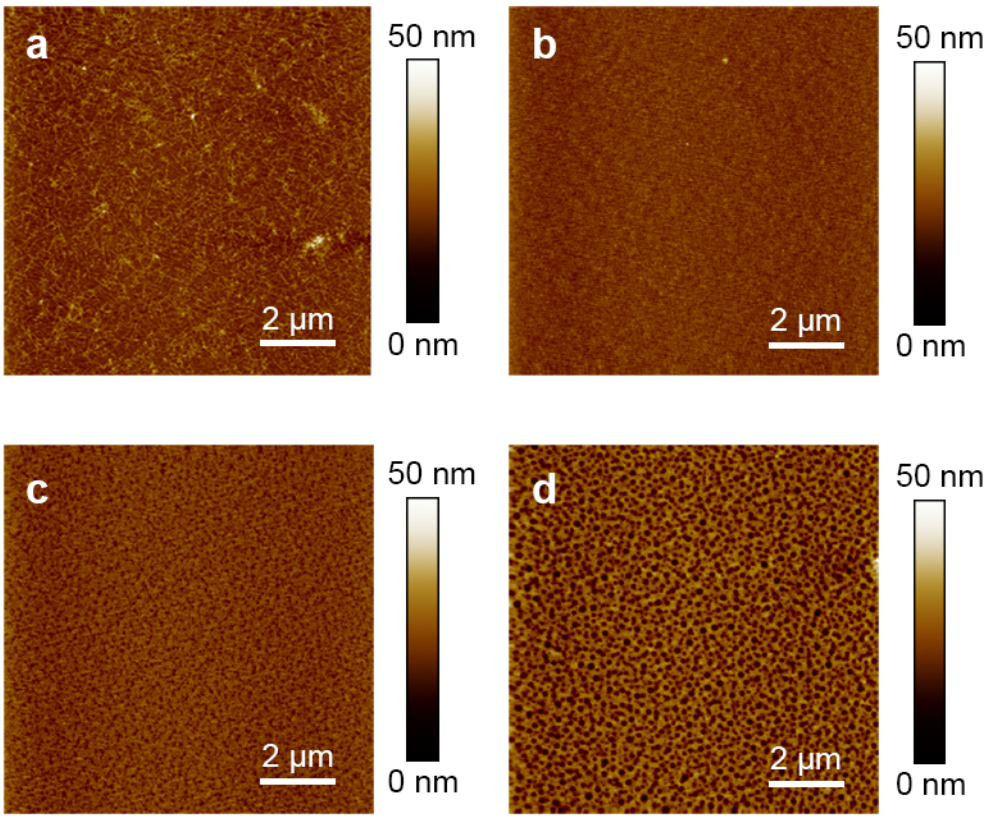

Figure 3.13. AFM topographical images of blend films at select PTEO loadings. Uniform distribution of nanofibril networks characteristic of semicrystalline P3HT can be found in the (a) 0% (i.e., pristine P3HT) and (b) 5% PTEO blends. At loadings of (c) 7.5%, domains of PTEO (black) emerged, and they grew at higher loadings, such as (d), which represents a film of 20% PTEO.

In conclusion, the incorporation of an open-shell macromolecule into a common conjugated model polymer demonstrated the potential advantage of incorporating redox-active stable radicals into OECT devices in conjunction with conjugated polymers. Specifically, PTEO operated as a handle by which to precisely control ion (i.e., dopant) injection at a distinct operating voltage, and this resulted in a maximum steady-state performance where μC* was > 150 F cm^{-1} V^{-1} s^{-1}. The redox activity of nitroxide radical groups dictated the threshold voltage of the overall blend film at which current was modulated even at small loadings. Transient responses and morphological characterization showed that there exists a trade-off between the steady-state performance and the transient response of the blend OECTs as the loading was further increased. The present strategy to blend a conjugated polymer semiconductor and an ionically conductive radical polymer counterpart can be achieved via a variety of different

chemistries. That is, in theory, an ionically conductive, redox-active conjugated polymer could be designed and be used in place of PTEO. However, the intrinsically amorphous nature of the nonconjugated, hydrophilic backbone with redox-active TEMPO sites makes PTEO a particularly attractive macromolecular candidate. Thus, we put forward that the incorporation of stable radicals offers a new archetype in designing high-performance next-generation organic mixed conductors for OECT applications.

3.5 References

(1) Turner, A. P. F. Biosensors: Sense and Sensibility. *Chem. Soc. Rev.* **2013**, *42* (8), 3184–3196.

(2) Rivnay, J.; Owens, R. M.; Malliaras, G. G. The Rise of Organic Bioelectronics. *Chem. Mater.* **2014**, *26* (1), 679–685.

(3) Zhang, M.; Lin, P.; Yang, M.; Yan, F. Fabrication of Organic Electrochemical Transistor Arrays for Biosensing. *Biochim. Biophys. Acta - Gen. Subj.* **2013**, *1830* (9), 4402–4406.

(4) Rivnay, J.; Inal, S.; Collins, B. A.; Sessolo, M.; Stavrinidou, E.; Strakosas, X.; Tassone, C.; Delongchamp, D. M.; Malliaras, G. G. Structural Control of Mixed Ionic and Electronic Transport in Conducting Polymers. *Nat. Commun.* **2016**, *7* (1), 1–9.

(5) Inal, S.; Malliaras, G. G.; Rivnay, J. Benchmarking Organic Mixed Conductors for Transistors. *Nat. Commun.* **2017**, *8* (1), 1767.

(6) Hansen, K. A.; Nerkar, J.; Thomas, K.; Bottle, S. E.; O'Mullane, A. P.; Talbot, P. C.; Blinco, J. P. New Spin on Organic Radical Batteries-An Isoindoline Nitroxide-Based High-Voltage Cathode Material. *ACS Appl. Mater. Interfaces* **2018**, *10* (9), 7982–7988.

(7) Fahlman, M.; Fabiano, S.; Gueskine, V.; Simon, D.; Berggren, M.; Crispin, X. Interfaces in Organic Electronics. *Nat. Rev. Mater.* **2019**, *4* (10), 627–650.

(8) Chung, J.; Khot, A.; Savoie, B. M.; Boudouris, B. W. 100th Anniversary of Macromolecular Science Viewpoint: Recent Advances and Opportunities for Mixed Ion and Charge Conducting Polymers. *ACS Macro Lett.* **2020**, *9* (5), 646–655.

(9) Khodagholy, D.; Curto, V. F.; Fraser, K. J.; Gurfinkel, M.; Byrne, R.; Diamond, D.; Malliaras, G. G.; Benito-Lopez, F.; Owens, R. M. Organic Electrochemical Transistor Incorporating an Ionogel as a Solid State Electrolyte for Lactate Sensing. *J. Mater. Chem.* **2012**, *22* (10), 4440–4443.

(10) Parlak, O.; Keene, S. T.; Marais, A.; Curto, V. F.; Salleo, A. Molecularly Selective Nanoporous Membrane-Based Wearable Organic Electrochemical Device for Noninvasive Cortisol Sensing. *Sci. Adv.* **2018**, *4* (7), eaar2904.

(11) Kuhlbusch, T. A. J.; Asbach, C.; Fissan, H.; Göhler, D.; Stintz, M. Nanoparticle Exposure at Nanotechnology Workplaces: A Review. *Part. Fibre Toxicol.* **2011**, *8* (1), 22.

(12) Leung, C. H.; Wu, K. J.; Li, G.; Wu, C.; Ko, C. N.; Ma, D. L. Application of Label-Free Techniques in Microfluidic for Biomolecules Detection and Circulating Tumor Cells Analysis. *TrAC - Trends Anal. Chem.* **2019**, *117*, 78–83.

(13) Williamson, A.; Ferro, M.; Leleux, P.; Ismailova, E.; Kaszas, A.; Doublet, T.; Quilichini, P.; Rivnay, J.; Rõzsa, B.; Katona, G.; et al. Localized Neuron Stimulation with Organic Electrochemical Transistors on Delaminating Depth Probes. *Adv. Mater.* **2015**, *27* (30), 4405–4410.

(14) Gerasimov, J. Y.; Gabrielsson, R.; Forchheimer, R.; Stavrinidou, E.; Simon, D. T.; Berggren, M.; Fabiano, S. An Evolvable Organic Electrochemical Transistor for Neuromorphic Applications. *Adv. Sci.* **2019**, *6* (7), 1801339.

(15) Khodagholy, D.; Doublet, T.; Quilichini, P.; Gurfinkel, M.; Leleux, P.; Ghestem, A.; Ismailova, E.; Hervé, T.; Sanaur, S.; Bernard, C.; et al. In Vivo Recordings of Brain Activity Using Organic Transistors. *Nat. Commun.* **2013**, *4* (1), 1–7.

(16) Gualandi, I.; Tonelli, D.; Mariani, F.; Scavetta, E.; Marzocchi, M.; Fraboni, B. Selective Detection of Dopamine with an All PEDOT:PSS Organic Electrochemical Transistor. *Sci. Rep.* **2016**, *6* (1), 1–10.

(17) Stříteský, S.; Marková, A.; Víteček, J.; Šafaříková, E.; Hrabal, M.; Kubáč, L.; Kubala, L.; Weiter, M.; Vala, M. Printing Inks of Electroactive Polymer PEDOT:PSS: The Study of Biocompatibility, Stability, and Electrical Properties. *J. Biomed. Mater. Res. - Part A* **2018**, *106* (4), 1121–1128.

(18) Inal, S.; Rivnay, J.; Hofmann, A. I.; Uguz, I.; Mumtaz, M.; Katsigiannopoulos, D.; Brochon, C.; Cloutet, E.; Hadziioannou, G.; Malliaras, G. G. Organic Electrochemical Transistors Based on PEDOT with Different Anionic Polyelectrolyte Dopants. *J. Polym. Sci. Part B Polym. Phys.* **2016**, *54* (2), 147–151.

(19) Khodagholy, D.; Gurfinkel, M.; Stavrinidou, E.; Leleux, P.; Herve, T.; Sanaur, S.; Malliaras, G. G. High Speed and High Density Organic Electrochemical Transistor Arrays. *Appl. Phys. Lett.* **2011**, *99* (16), 227.

(20) Rivnay, J.; Leleux, P.; Sessolo, M.; Khodagholy, D.; Hervé, T.; Fiocchi, M.; Malliaras, G. G. Organic Electrochemical Transistors with Maximum Transconductance at Zero Gate Bias. *Adv. Mater.* **2013**, *25* (48), 7010–7014.

(21) Bihar, E.; Deng, Y.; Miyake, T.; Saadaoui, M.; Malliaras, G. G.; Rolandi, M. A Disposable Paper Breathalyzer with an Alcohol Sensing Organic Electrochemical Transistor. *Sci. Rep.* **2016**, *6* (1), 1–6.

(22) Nilsson, D.; Kugler, T.; Svensson, P. O.; Berggren, M. An All-Organic Sensor-Transistor Based on a Novel Electrochemical Transducer Concept Printed Electrochemical Sensors on Paper. *Sensors Actuators, B Chem.* **2002**, *86* (2–3), 193–197.

(23) Coppedè, N.; Tarabella, G.; Villani, M.; Calestani, D.; Iannotta, S.; Zappettini, A. Human Stress Monitoring through an Organic Cotton-Fiber Biosensor. *J. Mater. Chem. B* **2014**, *2* (34), 5620–5626.

(24) Lin, P.; Yan, F.; Chan, H. L. W. Ion-Sensitive Properties of Organic Electrochemical Transistors. *ACS Appl. Mater. Interfaces* **2010**, *2* (6), 1637–1641.

(25) ElMahmoudy, M.; Inal, S.; Charrier, A.; Uguz, I.; Malliaras, G. G.; Sanaur, S. Tailoring the Electrochemical and Mechanical Properties of PEDOT:PSS Films for Bioelectronics. *Macromol. Mater. Eng.* **2017**, *302* (5), 1600497.

(26) Kayser, L. V.; Lipomi, D. J. Stretchable Conductive Polymers and Composites Based on PEDOT and PEDOT:PSS. *Adv. Mater.* **2019**, *31* (10), 1806133.

(27) Pingree, L. S. C.; MacLeod, B. A.; Ginger, D. S. The Changing Face of PEDOT:PSS Films: Substrate, Bias, and Processing Effects on Vertical Charge Transport. *J. Phys. Chem. C* **2008**, *112* (21), 7922–7927.

(28) Palumbiny, C. M.; Heller, C.; Schaffer, C. J.; Körstgens, V.; Santoro, G.; Roth, S. V.; Müller-Buschbaum, P. Molecular Reorientation and Structural Changes in Cosolvent-Treated Highly Conductive PEDOT:PSS Electrodes for Flexible Indium Tin Oxide-Free Organic Electronics. *J. Phys. Chem. C* **2014**, *118* (25), 13598–13606.

(29) Ouyang, L.; Musumeci, C.; Jafari, M. J.; Ederth, T.; Inganäs, O. Imaging the Phase Separation between PEDOT and Polyelectrolytes during Processing of Highly Conductive PEDOT:PSS Films. *ACS Appl. Mater. Interfaces* **2015**, *7* (35), 19764–19773.

(30) Zhang, S.; Kumar, P.; Nouas, A. S.; Fontaine, L.; Tang, H.; Cicoira, F. Solvent-Induced Changes in PEDOT:PSS Films for Organic Electrochemical Transistors. *APL Mater.* **2015**, *3* (1), 14911.

(31) Nielsen, C. B.; Giovannitti, A.; Sbircea, D. T.; Bandiello, E.; Niazi, M. R.; Hanifi, D. A.; Sessolo, M.; Amassian, A.; Malliaras, G. G.; Rivnay, J.; et al. Molecular Design of Semiconducting Polymers for High-Performance Organic Electrochemical Transistors. *J. Am. Chem. Soc.* **2016**, *138* (32), 10252–10259.

(32) Zeglio, E.; Inganäs, O. Active Materials for Organic Electrochemical Transistors. *Adv. Mater.* **2018**, *30* (44), 1800941.

(33) Rivnay, J.; Inal, S.; Salleo, A.; Owens, R. M.; Berggren, M.; Malliaras, G. G. Organic Electrochemical Transistors. *Nat. Rev. Mater.* **2018**, *3*, 17086.

(34) Savagian, L. R.; Österholm, A. M.; Ponder Jr, J. F.; Barth, K. J.; Rivnay, J.; Reynolds, J. R. Balancing Charge Storage and Mobility in an Oligo (Ether) Functionalized Dioxythiophene Copolymer for Organic-and Aqueous-based Electrochemical Devices and Transistors. *Adv. Mater.* **2018**, *30* (50), 1804647.

(35) Giovannitti, A.; Rashid, R. B.; Thiburce, Q.; Paulsen, B. D.; Cendra, C.; Thorley, K.; Moia, D.; Mefford, J. T.; Hanifi, D.; Weiyuan, D.; et al. Energetic Control of Redox-Active Polymers toward Safe Organic Bioelectronic Materials. *Adv. Mater.* **2020**, *32* (16), 1908047.

(36) Wang, Y.; Zeglio, E.; Liao, H.; Xu, J.; Liu, F.; Li, Z.; Maria, I. P.; Mawad, D.; Herland, A.; Mcculloch, I.; et al. Hybrid Alkyl-Ethylene Glycol Side Chains Enhance Substrate Adhesion and Operational Stability in Accumulation Mode Organic Electrochemical Transistors. *Chem. Mater.* **2019**, *31* (23), 9797–9806.

(37) Sun, H.; Vagin, M.; Wang, S.; Crispin, X.; Forchheimer, R.; Berggren, M.; Fabiano, S. Complementary Logic Circuits Based on High-Performance n-Type Organic Electrochemical Transistors. *Adv. Mater.* **2018**, *30* (9), 1704916.

(38) Giovannitti, A.; Maria, I. P.; Hanifi, D.; Donahue, M. J.; Bryant, D.; Barth, K. J.; Makdah, B. E.; Savva, A.; Moia, D.; Zetek, M.; et al. The Role of the Side Chain on the Performance of N-Type Conjugated Polymers in Aqueous Electrolytes. *Chem. Mater.* **2018**, *30* (9), 2945–2953.

(39) Giovannitti, A.; Sbircea, D. T.; Inal, S.; Nielsen, C. B.; Bandiello, E.; Hanifi, D. A.; Sessolo, M.; Malliaras, G. G.; McCulloch, I.; Rivnay, J. Controlling the Mode of Operation of Organic Transistors through Side-Chain Engineering. *Proc. Natl. Acad. Sci. U. S. A.* **2016**, *113* (43), 12017–12022.

(40) Moser, M.; Savagian, L. R.; Savva, A.; Matta, M.; Ponder, J. F.; Hidalgo, T. C.; Ohayon, D.; Hallani, R.; Reisjalali, M.; Troisi, A.; et al. Ethylene Glycol-Based Side Chain Length Engineering in Polythiophenes and Its Impact on Organic Electrochemical Transistor Performance. *Chem. Mater.* **2020**, *32* (15), 6618–6628.

(41) Moser, M.; Hidalgo, T. C.; Surgailis, J.; Gladisch, J.; Ghosh, S.; Sheelamanthula, R.; Thiburce, Q.; Giovannitti, A.; Salleo, A.; Gasparini, N.; et al. Side Chain Redistribution as a Strategy to Boost Organic Electrochemical Transistor Performance and Stability. *Adv. Mater.* **2020**, *32* (37), 2002748.

(42) Nakahara, K.; Oyaizu, K.; Nishide, H. Organic Radical Battery Approaching Practical Use. *Chem. Lett.* **2011**, *40* (3), 222–227.

(43) Bobela, D. C.; Hughes, B. K.; Braunecker, W. A.; Kemper, T. W.; Larsen, R. E.; Gennett, T. Close Packing of Nitroxide Radicals in Stable Organic Radical Polymeric Materials. *J. Phys. Chem. Lett.* **2015**, *6* (8), 1414–1419.

(44) Rostro, L.; Wong, S. H.; Boudouris, B. W. Solid State Electrical Conductivity of Radical Polymers as a Function of Pendant Group Oxidation State. *Macromolecules* **2014**, *47* (11), 3713–3719.

(45) Oyaizu, K.; Ando, Y.; Konishi, H.; Nishide, H. Nernstian Adsorbate-like Bulk Layer of Organic Radical Polymers for High-Density Charge Storage Purposes. *J. Am. Chem. Soc.* **2008**, *130* (44), 14459–14461.

(46) Aqil, A.; Vlad, A.; Piedboeuf, M. L.; Aqil, M.; Job, N.; Melinte, S.; Detrembleur, C.; Jérôme, C. A New Design of Organic Radical Batteries (ORBs): Carbon Nanotube Buckypaper Electrode Functionalized by Electrografting. *Chem. Commun.* **2015**, *51* (45), 9301–9304.

(47) Wilcox, D. A.; Agarkar, V.; Mukherjee, S.; Boudouris, B. W. Stable Radical Materials for Energy Applications. *Annu. Rev. Chem. Biomol. Eng.* **2018**, *9*, 83–103.

(48) Tan, Y.; Casetti, N. C.; Boudouris, B. W.; Savoie, B. M. Molecular Design Features for Charge Transport in Nonconjugated Radical Polymers. *J. Am. Chem. Soc.* **2021**, *143* (31), 11994–12002.

(49) Sung, S. H.; Bajaj, N.; Rhoads, J. F.; Chiu, G. T.; Boudouris, B. W. Radical Polymers Improve the Metal-Semiconductor Interface in Organic Field-Effect Transistors. *Org. Electron.* **2016**, *37*, 148–154.

(50) Leung, C.-H.; Wu, K.-J.; Li, G.; Wu, C.; Ko, C.-N.; Ma, D.-L. Application of Label-Free Techniques in Microfluidic for Biomolecules Detection and Circulating Tumor Cells Analysis. *TrAC Trends Anal. Chem.* **2019**, *117*, 78–83.

(51) Mukherjee, S.; Boudouris, B. W. An Introduction to Radical Polymers. In *Organic Radical Polymers*; Springer, 2017; pp 1–15.

(52) Suga, T.; Takeuchi, S.; Nishide, H. Morphology-Driven Modulation of Charge Transport in Radical/Ion-Containing, Self-Assembled Block Copolymer Platform. *Adv. Mater.* **2011**, *23* (46), 5545–5549.

(53) Suga, T.; Sakata, M.; Aoki, K.; Nishide, H. Synthesis of Pendant Radical- and Ion-Containing Block Copolymers via Ring-Opening Metathesis Polymerization for Organic Resistive Memory. *ACS Macro Lett.* **2014**, *3* (8), 703–707.

(54) Baradwaj, A. G.; Wong, S. H.; Laster, J. S.; Wingate, A. J.; Hay, M. E.; Boudouris, B. W. Impact of the Addition of Redox-Active Salts on the Charge Transport Ability of Radical Polymer Thin Films. *Macromolecules* **2016**, *49* (13), 4784–4791.

(55) Yu, I.; Jeon, D.; Boudouris, B.; Boudouris, B.; Joo, Y. Mixed Ionic and Electronic Conduction in Radical Polymers. *Macromolecules* **2020**, *53* (11), 4435–4441.

(56) Janoschka, T.; Hager, M. D.; Schubert, U. S. Powering up the Future: Radical Polymers for Battery Applications. *Adv. Mater.* **2012**, *24* (48), 6397–6409.

(57) Nishide, H.; Iwasa, S.; Pu, Y. J.; Suga, T.; Nakahara, K.; Satoh, M. Organic Radical Battery: Nitroxide Polymers as a Cathode-Active Material. *Electrochim. Acta* **2004**, *50* (2-3 SPEC. ISS.), 827–831.

(58) Tomlinson, E. P.; Hay, M. E.; Boudouris, B. W. Radical Polymers and Their Application to Organic Electronic Devices. *Macromolecules* **2014**, *47* (18), 6145–6158.

(59) He, J.; Mukherjee, S.; Zhu, X.; You, L.; Boudouris, B. W.; Mei, J. Highly Transparent Crosslinkable Radical Copolymer Thin Film as the Ion Storage Layer in Organic Electrochromic Devices. *ACS Appl. Mater. Interfaces* **2018**, *10* (22), 18956–18963.

(60) Joo, Y.; Agarkar, V.; Sung, S. H.; Savoie, B. M.; Boudouris, B. W. A Nonconjugated Radical Polymer Glass with High Electrical Conductivity. *Science (80-.).* **2018**, *359* (6382), 1391–1395.

(61) Xie, Y.; Zhang, K.; Monteiro, M. J.; Jia, Z. Conjugated Nitroxide Radical Polymers: Synthesis and Application in Flexible Energy Storage Devices. *ACS Appl. Mater. Interfaces* **2019**, *11* (7), 7096–7103.

(62) Li, F.; Gore, D. N.; Wang, S.; Lutkenhaus, J. L. Unusual Internal Electron Transfer in Conjugated Radical Polymers. *Angew. Chemie - Int. Ed.* **2017**, *56* (33), 9856–9859.

(63) Li, F.; Wang, S.; Zhang, Y.; Lutkenhaus, J. L. Electrochemical Energy Storage in Poly(Dithieno[3,2-b:2′,3′-d]Pyrrole) Bearing Pendant Nitroxide Radicals. *Chem. Mater.* **2018**, *30* (15), 5169–5174.

(64) Wang, S.; Easley, A. D.; Thakur, R. M.; Ma, T.; Yun, J.; Zhang, Y.; Ober, C. K.; Lutkenhaus, J. L. Quantifying Internal Charge Transfer and Mixed Ion-Electron Transfer in Conjugated Radical Polymers. *Chem. Sci.* **2020**, *11* (36), 9962–9970.

(65) Akkiraju, S.; Vergados, J.; Hoagland, L.; Lu, Z.; Anandan, V.; Boudouris, B. W. Design of Mixed Electron-and Ion-Conducting Radical Polymer-Based Blends. *Macromolecules* **2021**.

(66) Frankenstein, H.; Stein, E.; Stolov, M.; Koifman Khristosov, M.; Freger, V.; Frey, G. L. Blends of Polymer Semiconductor and Polymer Electrolyte for Mixed Ionic and Electronic Conductivity. *J. Mater. Chem. C* **2021**, *9* (24), 7765–7777.

(67) Keene, S. T.; van der Pol, T. P. A.; Zakhidov, D.; Weijtens, C. H. L.; Janssen, R. A. J.; Salleo, A.; van de Burgt, Y. Enhancement-Mode PEDOT:PSS Organic Electrochemical Transistors Using Molecular De-Doping. *Adv. Mater.* **2020**, *32* (19).

(68) Yamamoto, S.; Malliaras, G. G. Controlling the Neuromorphic Behavior of Organic Electrochemical Transistors by Blending Mixed and Ion Conductors. *ACS Appl. Electron. Mater.* **2020**, *2* (7), 2224–2228.

(69) Flagg, L. Q.; Bischak, C. G.; Onorato, J. W.; Rashid, R. B.; Luscombe, C. K.; Ginger, D. S. Polymer Crystallinity Controls Water Uptake in Glycol Side-Chain Polymer Organic Electrochemical Transistors. *J. Am. Chem. Soc.* **2019**, *141* (10), 4345–4354.

(70) Endo, T.; Takuma, K.; Takata, T.; Hirose, C. Synthesis and Polymerization of 4-(Glycidyloxy)-2, 2, 6, 6-Tetramethylpiperidine-1-Oxyl. *Macromolecules* **1993**, *26* (12), 3227–3229.

(71) Oyaizu, K.; Suga, T.; Yoshimura, K.; Nishide, H. Synthesis and Characterization of Radical-Bearing Polyethers as an Electrode-Active Material for Organic Secondary Batteries. *Macromolecules* **2008**, *41* (18), 6646–6652.

(72) Sato, K.; Sukegawa, T.; Oyaizu, K.; Nishide, H. Synthesis of Poly(TEMPO-Substituted Glycidyl Ether) by Utilizing t-BuOK/18-Crown-6 for an Organic Cathode-Active Material. In *Macromolecular Symposia*; Wiley Online Library, 2015; Vol. 351, pp 90–96.

(73) Li, Y.; Ding, Z.; Li, J.; Wang, K.; Lu, T.; Pan, L. Novel Membrane-Free Hybrid Capacitive Deionization with a Radical Polymer Anode for Stable Desalination. *Desalination* **2020**, *481*, 114379.

(74) Liu, T.; Wei, X.; Nie, Z.; Sprenkle, V.; Wang, W. A Total Organic Aqueous Redox Flow Battery Employing a Low Cost and Sustainable Methyl Viologen Anolyte and 4-HO-TEMPO Catholyte. *Adv. Energy Mater.* **2016**, *6* (3), 1501449.

(75) Flagg, L. Q.; Giridharagopal, R.; Guo, J.; Ginger, D. S. Anion-Dependent Doping and Charge Transport in Organic Electrochemical Transistors. *Chem. Mater.* **2018**, *30* (15), 5380–5389.

(76) Hellmann, C.; Paquin, F.; Treat, N. D.; Bruno, A.; Reynolds, L. X.; Haque, S. A.; Stavrinou, P. N.; Silva, C.; Stingelin, N. Controlling the Interaction of Light with Polymer Semiconductors. *Adv. Mater.* **2013**, *25* (35), 4906–4911.

(77) Kim, T.; Im, J. H.; Choi, H. S.; Yang, S. J.; Kim, S. W.; Park, C. R. Preparation and Photoluminescence (PL) Performance of a Nanoweb of P3HT Nanofibers with Diameters below 100 Nm. *J. Mater. Chem.* **2011**, *21* (37), 14231–14239.

(78) Zhao, K.; Ding, Z.; Xue, L.; Han, Y. Crystallization-Induced Phase Segregation Based on Double-Crystalline Blends of Poly(3-Hexylthiophene) and Polyethylene Glycolsa. *Macromol. Rapid Commun.* **2010**, *31* (6), 532–538.

(79) Dyson, M. J.; Lariou, E.; Martin, J.; Li, R.; Erothu, H.; Wantz, G.; Topham, P. D.; Dautel, O. J.; Hayes, S. C.; Stavrinou, P. N.; et al. Managing Local Order in Conjugated Polymer Blends via Polarity Contrast. *Chem. Mater.* **2019**, *31* (17), 6540–6547.

(80) Parmeggiani, M.; Verna, A.; Ballesio, A.; Cocuzza, M.; Piatti, E.; Fra, V.; Pirri, C. F.; Marasso, S. L. P3HT Processing Study for In-Liquid EGOFET Biosensors: Effects of the Solvent and the Surface. *Sensors (Switzerland)* **2019**, *19* (20), 4497.

(81) Bernards, D. A.; Malliaras, G. G. Steady-State and Transient Behavior of Organic Electrochemical Transistors. *Adv. Funct. Mater.* **2007**, *17* (17), 3538–3544.

(82) Nightingale, J.; Pitsalidis, C.; Pappa, A. M.; Tan, E.; Stewart, K.; Owens, R. M.; Kim, J. S. Small Molecule Additive for Low-Power Accumulation Mode Organic Electrochemical Transistors. *J. Mater. Chem. C* **2020**, *8* (26), 8846–8855.

(83) Romele, P.; Ghittorelli, M.; Kovács-Vajna, Z. M.; Torricelli, F. Ion Buffering and Interface Charge Enable High Performance Electronics with Organic Electrochemical Transistors. *Nat. Commun.* **2019**, *10* (1), 1–11.

4. ALL-PRINTED STRETCHABLE CORNEAL SENSOR ON SOFT CONTACT LENSES FOR NONINVASIVE AND PAINLESS ELECTRODIAGNOSIS*

4.1 Abstract

Electroretinogram (ERG) examinations serve as routine clinical procedures in ophthalmology for the diagnosis and management of many ocular diseases. However, the rigid form factor of current corneal sensors produces a mismatch with the soft, curvilinear, and exceptionally sensitive human cornea, which typically requires the use of topical anesthesia and a speculum for pain management and safety. Here we report a new design of all-printed stretchable corneal sensor built on commercially available disposable soft contact lenses that can intimately and non-invasively interface with the corneal surface of human eyes. The corneal sensor is integrated with soft contact lenses via electrochemical anchoring in a seamless manner that ensures the mechanical and chemical reliability, and thus it enables high-fidelity recording of full-field ERG signals without the need of topical anesthesia or a speculum. The corneal sensor, superior to clinical standards in terms of signal quality and comfortability, is expected to address unmet clinical needs in the field of ocular electrodiagnosis.

4.2 Introduction

Electrophysiological activity of the retina in response to a light stimulus, known as an electroretinogram (ERG), can be recorded at the corneal surface in ophthalmic examinations for the diagnosis or early detection of many ocular diseases such as glaucoma, retinitis pigmentosa, diabetic retinopathy, retinoschisis/detachment, and other congenital degenerations.[1–3] The measurement of ERG signals occurs by contacting a recording electrode directly with either: (i) the corneal surface or (ii) the bulbar conjunctiva while placing a grounding electrode and a reference electrode on the earlobe and forehead, respectively.[4,5] The gold-standard methods in these measurements usually involve the use of contact lens-type devices (e.g., the ERG-Jet lens) that facilitates direct contact to the corneal surface and thereby enables the recording of ERG

* Reprinted with permission from Kim, K.; Kim, H. J.; Zhang, H.; Park, W.; Meyer, D.; Kim, M. K.; Kim, B.; Park, H.; Xu, B.; Kollbaum, P. All-Printed Stretchable Corneal Sensor on Soft Contact Lenses for Noninvasive and Painless Ocular Electrodiagnosis. Nat. Commun. 2021, 12 (1), 1–11. Copyright 2022 Springer Nature.

signals with relatively higher amplitudes than conjunctival electrodes.[6] However, these devices are made up of a thick, rigid contact lens with non-optimal geometries (in particular, anteriorly-protruding bumps and large outer curvature for human eyes), resulting in discomfort to both the cornea and eyelid despite ocular topical anesthesia. This discomfort is not easily tolerated by children and adults with poor cooperation, and thereby general anesthesia or sedation is often required for these patients.[7,8] In cases of patient refusal of anesthesia or sedation, hook-type conjunctival devices [e.g., the Dawson Trick Litzkow (DTL) fiber] can alternatively be used, but the signal quality is significantly compromised (e.g. < 46%) due to its far distance from the cornea, limiting the interpretability of the obtained data.[9,10]

Newer versions of contact lens-type devices (e.g., the Burian-Allen lens) include a built-in speculum that prevents blinking, and therefore, enhance the safety and ease-of-use of these devices from the practitioner standpoint.[11] However, the bulky size of the built-in speculum creates its own discomfort and thereby limits its use for children or adults with small eyelid fissures.[12] Moreover, these devices are expensive, and therefore, they are often reused multiple times across different patients, requiring a thorough disinfection process in which the practitioner may lack complete confidence especially with ongoing issues of easily transferable viruses [e.g., the Coronavirus disease 2019 (COVID-19)]. Due to these reasons, these devices are only used in rare instance and on sedated patients.[13] Recent technological advances demonstrate the feasibility of fabricating flexible sensors on soft contact lenses (SCLs) made of hydrogel silicone or Parylene-C by exploiting the unique properties of nanomaterials (e.g., graphene and nanowires) to provide enhanced on-eye transparency, oxygen permeability, and flexibility.[14–16] However, their practical application in human eyes remains impeded due to the lack of mechanical reliability (for lens handling, fitting, cleaning, and inadvertent eye rubbing) and chemical stability (for long-term lens storage and multiple disinfection cycles). Therefore, there is a critical opportunity to develop and evaluate a safe, easy-to-use, comfortable, cost-effective, and reliable corneal sensor for the measurement of ERG signals in human eyes.

Here, we report on the design of an all-printed stretchable corneal sensor applied to commercially available disposable SCLs (Figure 4.1a). The corneal sensor includes a circular serpentine trace of conduction paths located at the outer peripheral edge of a SCL, allowing light to pass unobstructed through the center lens region. Electrochemical deposition and subsequent adhesion of the corneal sensor to a SCL promotes the mechanical robustness against thousands

cycles of folding and scrubbing and also the chemical stability with lens cleaning and disinfecting solutions. In addition, this approach is applicable to various materials and designs of SCLs that offer excellent biocompatibility, softness [mechanical modulus (E) = 0.2-2 MPa], transparency (~100%), oxygen permeability (10-200 Dk/t), wettability (water content = 30-80%), and are able to fit a variety of corneal shapes (8.3-9.0 mm base curve radii).[17,18] The corneal sensor is also linked to a simultaneously-printed elastomeric wire for external connection to a data acquisition system. The connection wire is lightweight (~1.4 mg cm^{-1}) and highly stretchable (up to 350%), and thereby can efficiently accommodate blinking and eye rotational movements (e.g. on average around ± 4 mm). The resulting device conforms to the corneal anterior surface in human eyes as much as a bare SCL does and provides better comfortability than current clinical standards. These aspects enable the high-fidelity recording of full-field ERG responses in a non-invasive manner without the need of corneal anesthesia or a speculum. The results of the first human tests demonstrate the feasibility of the corneal sensor in a standard ocular electrodiagnostic setting.

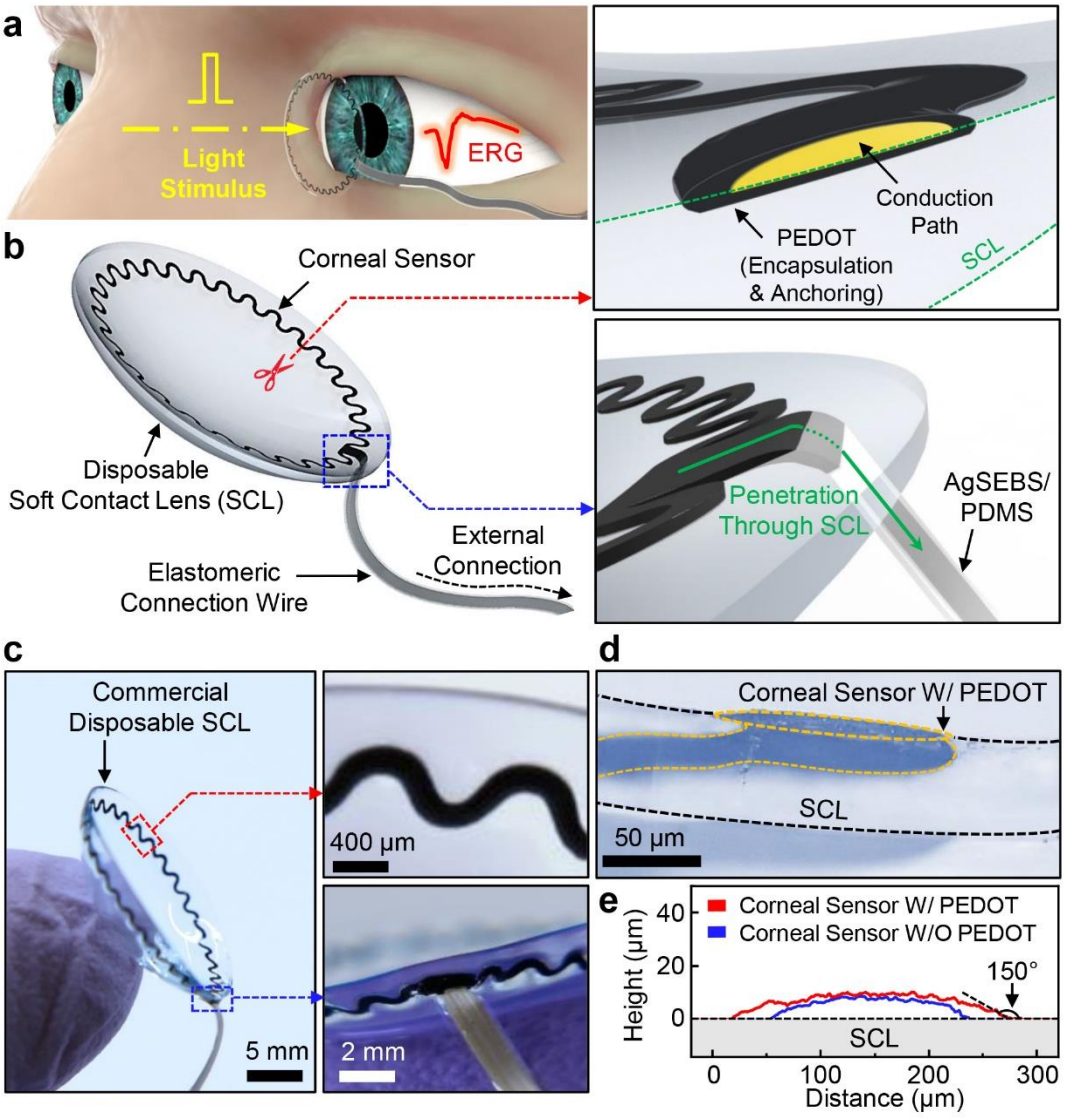

Figure 4.1. (a) Schematic illustration of ERG recording in response to a light stimulus from a human eye using the corneal sensor. (b) Schematic illustrations of the corneal sensor, with inset images highlighting the embedded encapsulation and anchoring layers (top panel) and its seamless integration with the connection wire (bottom panel). (c) Photographs of the corneal sensor, with inset images highlighting the embedded serpentine layout (top panel) and its seamless integration with the connection wire (bottom panel). (d) Cross-sectional microscope image of the corneal sensor. **e**, Surface topology of the corneal sensor with and without a poly(3,4-ethylenedioxythiophene) (PEDOT) layer.

4.3 Methods

4.3.1 Automated Dispenser-Printing Process

A glass substrate (i.e., a plain microscope slide, Dow Corning) was cleaned in a bath of acetone and isopropyl alcohol (IPA) with sonication for 30 minutes each, followed by exposure to UV-ozone for 10 minutes. A water-soluble PVA (10 wt% of Mowiol 4-88 in DI water) was spun coat on the glass substrate at 1,000 rpm for 30 seconds to serve as a sacrificial layer, and then baked at 100°C for 30 minutes. In parallel, the formulated PDMS ink was prepared by mixing the base solution (DOWSIL SE1700, Sylgard 184, Dow Corning) and curing agent with a weight ratio of 1:1:0.2. The formulated AgSEBS ink was prepared by dissolving 1.5 g of SEBS (H1221, Asahi Kasei) in 1.5 g of tetrahydrofuran (Aldrich) and 4 g of 1,2-dichlorobenzene (Aldrich) and mixing 8 g of Ag flakes (2-5 μm, Inframat Advanced Materials) with a planetary centrifugal mixer (Thinky, ARE-310). Direct writing of the PDMS ink was carried out on the glass substrate coated with the PVA sacrificial layer to define the bottom encapsulation layer. For this, a stainless-steel tip (Nordson EFD) with the inner diameter of 200 μm was used by applying the pneumatic pressure and printing speed at 25 psi and 8 mm s^{-1}, respectively. Following thermal annealing of the printed PDMS ink at 70°C for 30 minutes, another direct writing of the AgSEBS ink was carried out to define the conduction paths. For this, a stainless-steel tip with the inner diameter of 150 μm was used by applying the pneumatic pressure and printing speed of 35 psi and 8 mm s^{-1}, respectively. The entire structure was then heated at 70°C for 1 hour. Finally, one more direct writing of the PDMS ink was carried out to define the top encapsulation layer, followed by annealing at 70°C for 30 minutes. The entire structure was then immersed in DI water to dissolve the underneath PVA layer, allowing the corneal sensor to be released from the glass substrate. The conduction paths (i.e., AgSEBS) within the corneal sensor was then plated with Au in a 24 K pure gold plating solution for 30 seconds by using a general plating kit (Gold Plating Services) at the applied voltage of 3 V. After rinsing with DI water, the Au-coated corneal sensor was then transferred to the inner surface of a SCL, while the elastomeric connection wire was penetrated out through the SCL on the edge. Different types of commercially available disposable SCLs (Frequency 55 from CooperVision, ACUVUE Oasys from Johnson & Johnson, and Biotrue OneDay from Bausch & Lomb) were tested in this study.

4.3.2 Electrochemical Printing Process

The as-printed corneal sensor was immersed in DI water containing 0.02 M EDOT (Sigma Aldrich) and 0.1 M sodium *p*-toluenesulfonate salt (Sigma Aldrich) for 30 minutes, while its connection wire was connected to a working electrode. The electrochemical polymerization of PEDOT was subsequently carried out with a platinum (Pt) counter electrode and Ag/AgCl reference electrode by applying the bias voltage at 1 V for 4 minutes. The complete device was then immersed in DI water for 30 minutes, followed by thorough rinsing with a lens saline solution (Sensitive Eyes, Bausch & Lomb) to remove residual EDOT and salts. Furthermore, the device was immersed in a cleansing kit containing a 3% H_2O_2 formula (ClearCare®, Alcon) overnight for disinfection. The surface topology and thickness of the device were characterized using a P-7 surface profilometer (KLA-Tencor) and scanning electron microscope (SEM; S-4800, Hitachi), respectively.

4.3.3 Monitoring of Electrochemical Impedance

The electrochemical impedance of the device was measured using a VersaSTAT 3 potentiostat analyzer (Princeton Applied Research) with a standard three-electrodes configuration in a PBS solution (pH = 7.4) at room temperature. A LowProfile platinum electrode (PINE Research) and LowProfile Ag/AgCl electrode (PINE Research) were used to serve as the counter and reference electrode, respectively. A 10 mV rms AC voltage was applied at varied frequencies ranging from 0.1 Hz to 100 kHz during these measurements. To characterize the chemical stability, the device was stored in either lens cleaning solution, PBS, or an artificial tear solution. Prior to each test, the device was rinsed with PBS for 1 minute and immersed in a new PBS for 30 minutes.

4.3.4 Electrical and Electrochemical Measurements under Repeated Stretching

The device was loaded on a chuck of a tensile testing machine (ESM303, Mark-10) and then stretched to a prescribed stretching ratio. The device was stretched and released at the elongation rate of 10-20% per minute, while its resistance was simultaneously monitored using a source meter (Keithley 2400). The connection wire was stretched and released at the elongation

rate of 100% per minute. During these tests, the electrochemical impedance of the device was also monitored at every 150 cycles.

4.3.5 Cell Compatibility Evaluation

The device was sterilized with an ethanol-DI water mixture (70:30 v/v) for 30 min, rinsed with Dulbecco's PBS (Gibco), and dehydrated with UV irradiation for 1 hour. The sterilized device was then placed inside a 24-well plate on a concave side facing upwards. Human corneal epithelial cells (HCEpiC, MilliporeSigma) with the density of 1×10^5/well were seeded in a cell media (EpiGRO™ Human Ocular Epithelia Complete Media, MilliporeSigma) for 12 hours, and subsequently incubated in a humid incubator maintained at 37°C with 5% CO_2 for 24 hours. A 3-(4,5-dimethylthiazol-2-yl)-2,5-diphenyltetrazolium bromide (MTT, MilliporeSigma) reagent was added and incubated for 3 hours. Following removal of the cell media, the cells were lysed with dimethylsulfoxide (ATTC). The absorbance of each well was measured using a microplate reader (Synergy™ NEO, BioTek) at the wavelength of 575 nm. The statistical analysis was carried out using a one-way ANOVA method with the Tukey's post hoc test implemented in the Origin software (OriginLab) and are expressed as averages ± s.e.m. (n = 5)

4.3.6 FEA Analysis

The FEA analysis was conducted through the ABAQUS/Standard package. In the FEA model, the corneal sensor was strongly bonded to the SCL to mimic their monolithic integration. The mechanical modulus (E) and Poisson's ratio of the corneal sensor and the SCL was 810 kPa and 0.4, and 14 MPa and 0.1, respectively. C3D4 elements were utilized mesh refinements in the corneal sensor to capture the local stress concentration. For the flipping loading condition, the edge of the corneal sensor was only allowed in-plane deformation, and a vertical force was applied at the bottom. For the folding loading condition, two rigid plates were in contact with the corneal sensor to achieve the complete folding. For the stretching loading condition, the corneal sensor was clamped by two rigid plates at both ends and then stretched under a quasi-static loading state. For the expanding loading condition, a rigid circular plate was bonded at the edge of the corneal sensor and expanded by increasing temperature to control the expanding ratio.

4.3.7 Measurement of Standard Full-field ERG Signals

The measurement of the full-field ERG signals was conducted using an amplifier (PL3516, ADINSTUMENTS) at the sampling rate and resolution of 2 kHz and 0.1 μV, respectively. The corneal sensor and DTL fiber were worn on the left eye of the participant before dark adaptation, while the ERG Jet-lens was necessarily worn after dark adaptation under a dim red light in order to minimize the wearing time due to corneal irritations. The ERG signals (Dark 0.01, Dark 3.0, and Dark 10.0) were measured under a light stimulus for 2 milliseconds with the intensity of 0.01, 3.0, and 10 $cd \cdot s \cdot m^{-2}$, respectively. Under a dim light of 0.01 $cd \cdot s \cdot m^{-2}$ for the Dark 0.01, slowly responding b-waves were observed due to the response time of a rod-driven on-bipolar cell in the retina. For the Dark 3.0, the a-wave appeared before the b-wave, while the amplitude of the b-wave was increased with the faster response of the rod- and cone-driven bipolar cell activity. For the Dark 10.0, the a-waves were more clearly appeared relative to the Dark 3.0. The bandpass filters for the Dark 0.01, Dark 3.0, and Dark 10.0 were ranged from 0.3 to 300 Hz. A different bandpass filter (75-300 Hz) was used for the Dark OP. For the Light 3.0 and Light Flicker, the light adaptation was carried out at 30 $cd \cdot m^{-2}$ for 10 minutes. The Light 3.0 was measured under the background light of 30 $cd \cdot m^{-2}$ and single light stimulus for 2 milliseconds at the intensity of 3.0 $cd \cdot s \cdot m^{-2}$. The Light Flicker was obtained with multiple light stimuli at 30 Hz. The applied bandpass filter was ranged from 0.3 to 300 Hz. The statistical analysis for the amplitude and implicit time of the ERG signals was carried out using a one-way ANOVA method with the Tukey's post hoc test implemented in the Origin software (OriginLab).

4.3.8 Ocular Coherence Tomography (OCT)

The OCT images were acquired prior to and during the application of the device using a Zeiss Visante OCT (Carl Zeiss). The data acquisition was made in corneal high-resolution mode at 16 meridians (e.g., slices).

4.3.9 Slit Lamp Micrograph

The slit lamp biomicroscopic examinations with and without sodium fluorescein installation were performed prior to each testing, with the device in place, and following testing. Magnifications ranging from 10× to 16× were used.

4.4 Results and Discussion

4.4.1 Basic Design, Layout, and Fabrication Strategy

Figure 4.1b presents schematic representations of the overall device design. The corneal sensor is configured into a thin, narrow serpentine trace (250 μm-wide × 10 μm-thick × 66 mm-long) and positioned on the inner surface of a commercially available disposable SCL facing the corneal surface. A conductive biocompatible polymer, poly(3,4-ethylenedioxythiophene) (PEDOT) doped with tosylate,[19–21] is electrochemically printed around the entire outer surface of the corneal sensor in order to provide a thin encapsulation layer and promote anchoring to the SCL (Figure 4.1b, top inset image). The corneal sensor is monolithically linked to an elastomeric connection wire (1 mm-wide × 120 μm-thick × > 5 cm-long) that is comprised of formulated elastomers, such as silver flake-filled polystyrene-b-poly(ethylene-co-butylene)-b-polystyrene (AgSEBS) and fumed silica nanoparticle-filled polydimethylsiloxane (PDMS).[22,23] Here, the connection wire penetrates through the SCL for seamless integration (Figure 4.1b, bottom inset image). Figure 4.1c shows the overall size and design configuration of the resulting device built upon a disposable SCL (ACUVUE Oasys, Johnson & Johnson; center thickness of 70 μm).

Figure 4.2 shows schematic illustrations of the entire procedure for fabricating the corneal sensor. The fabrication begins with an automated dispenser-printing tool equipped on a three-axis computer-controlled translation stage (Nordson EFD, resolution: 1 μm, repeatability: +/-3 μm). This printing tool allows for direct writing of elastomeric inks (e.g., the formulated AgSEBS and PDMS) on a glass substrate coated with a water-soluble polyvinyl alcohol (PVA) layer. This printing technique provides the versatility to write multiple layers of linear and curvilinear traces uniformly at the microscale (> 100 μm in width, > 10 μm in thickness) in a series of pre-programmed steps, enabling batch production (> 10 units per batch). The next step involves removing the water-soluble PVA layer with deionized (DI) water, followed by electroplating the conduction path (i.e., AgSEBS) with gold (Au) not only to promote electrical conductivity but also to enhance scratch resistance and chemical stability within aqueous media.[24] The as-printed corneal sensor is then transferred to the inner surface of a SCL, while the elastomeric connection wire is inserted out through the SCL. The serpentine trace of the corneal sensor is stretched when contacted to the curvilinear surface of the SCL until it accommodates the interfacial stress, thereby avoiding any surface discontinuity.[25] The next step involves an

electrochemical polymerization of 3,4-ethylenedioxythiophene (EDOT) to form a thin PEDOT layer over the Au-coated surface (Figure 4.3). Finally, the resulting device is thoroughly washed with a preservative-free saline solution, followed by an overnight sterilization process with a commercial disinfection hydrogen peroxide (H_2O_2) solution. Details of the materials and fabrication procedures are shown in Methods section.

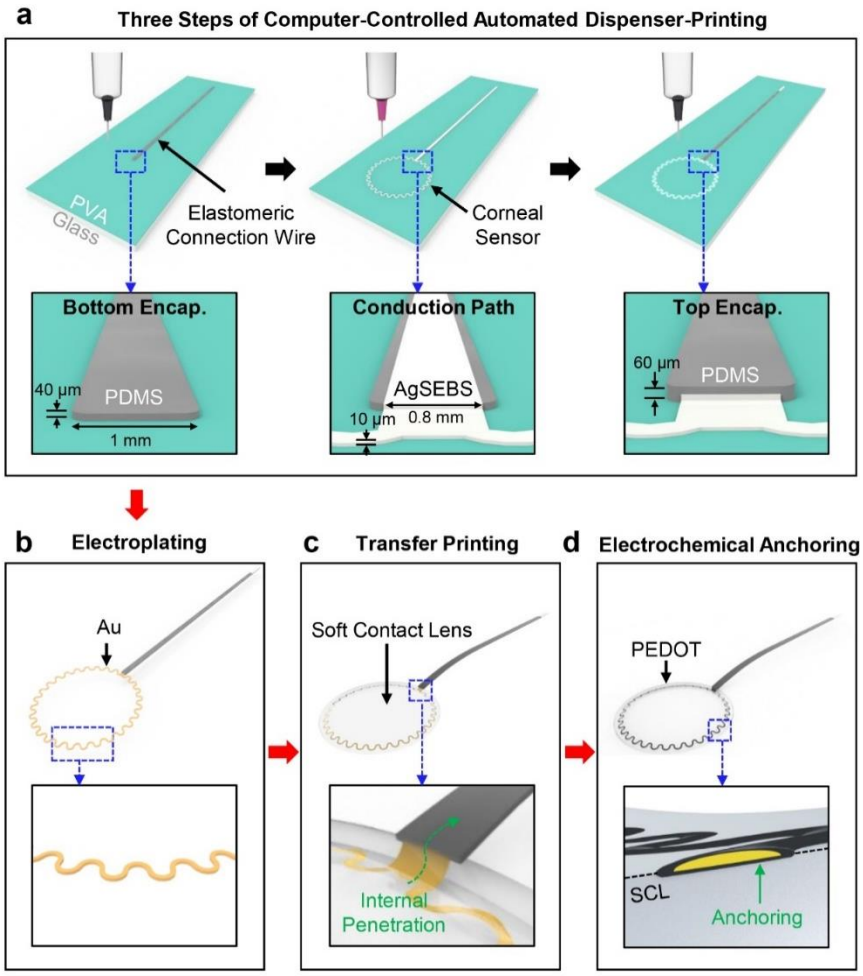

Figure 4.2. (a) A series of computer-controlled automated dispenser-printing processes for the fabrication of the corneal sensor on a temporary glass substrate coated with a water-soluble PVA layer. The bottom magnified images show the dimensions of each printed layer. (b) Electroplating process of the conduction path (i.e., AgSEBS layer) with Au. The bottom magnified image highlights the change of color to gold after the electroplating process. (c) Transfer printing process of the entire structure from the temporary glass substrate to the inner surface of a SCL. The bottom magnified image highlights the connection wire inserted out through the SCL for seamless integration, (d) Electrochemical polymerization of EDOT to form a PEDOT layer over the corneal sensor. The bottom magnified image highlights the monolithic anchoring of the corneal sensor to the SCL.

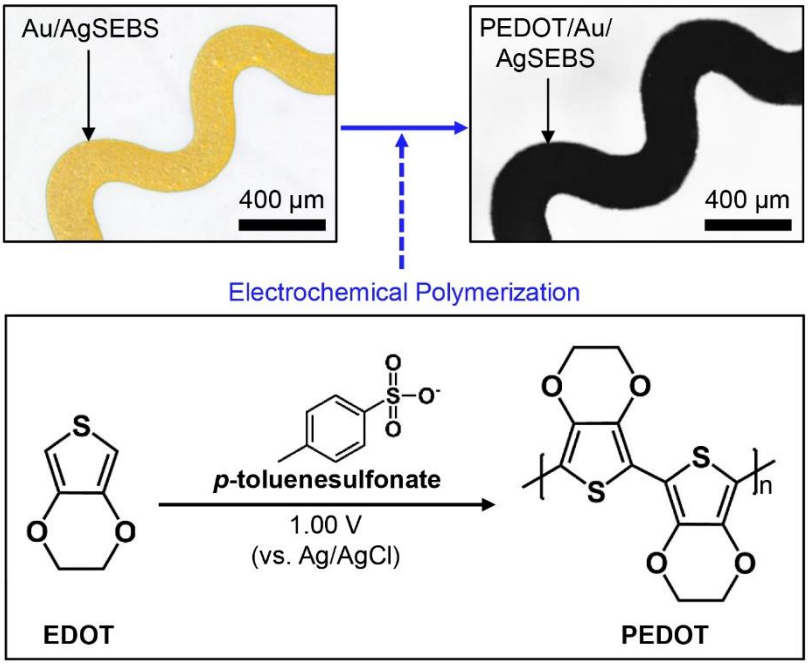

Figure 4.3. Enlarged microscope images of the corneal sensor before (top left image) and after (top right image) the electrochemical polymerization of PEDOT, with a scheme of the electrochemical polymerization process (bottom image).

The cross-sectional microscope image in Figure 1d shows that the electrochemically grown PEDOT layer conformed the surface of the corneal sensor and seamlessly penetrated the SCL. Figure 1e shows the surface topology of the corneal sensor with (red line) and without (blue line) a PEDOT layer, of which the electrochemical processing time was fixed at 4 minutes. The results indicate that the peak heights remained below 10 µm, while the formation of the PEDOT layer occurred predominantly at the edge of the corneal sensor due to uneven current distribution across the round surface.[26] Consequently, a gradual taper angle of ≤ 30° was created at the edge of the PEDOT layer, offering enhanced conformal contact to the corneal surface. These features are important to minimize irritation to the cornea, while reducing the edge stress.[27] The corresponding results of the gradually tapered PEDOT layer as a function of varied electrochemical processing time ranging from 1 to 4 minutes are summarized in Figure 4.4. These observations were reproducible across different types (e.g., materials, water content, and ionicity) of commercially available disposable SCLs (Figure 4.5).

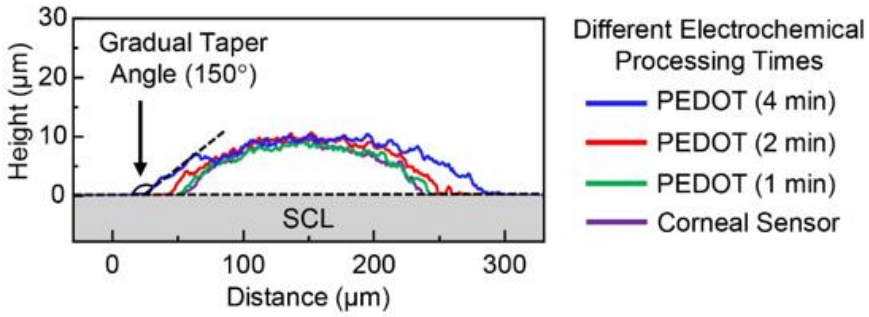

Figure 4.4. Surface topology of the corneal sensor with a PEDOT layer prepared at different electrochemical processing times.

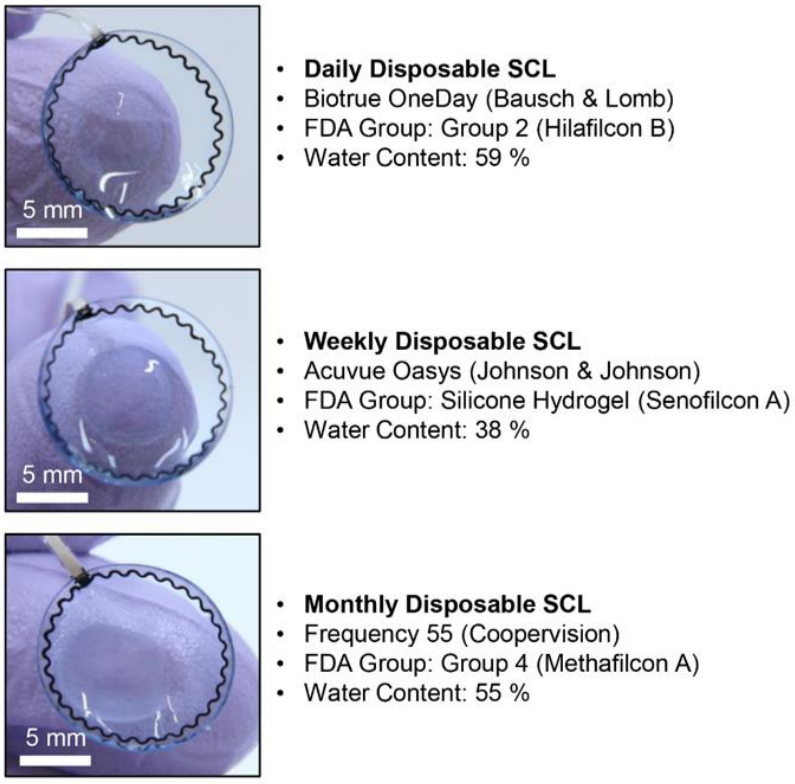

Figure 4.5. Photographs of the corneal sensor applied to daily, weekly, and monthly disposable SCLs from the top. The commercial name, water content, and classification by the U.S. Food and Drug Administration (FDA) of each SCL are denoted.

4.4.2 Mechanical and Chemical Characterization

The experimental results in Figure 4.6a show that the corneal sensor provides a similar modulus (E = 790 ± 140 kPa) to a bare control SCL (blue line; ACUVUE Oasys, Johnson & Johnson), while the bare corneal sensor (without the SCL) provides > 2 times lower modulus (green line; E = 374 ± 47 kPa). The low modulus of the bare corneal sensor allows its addition to a SCL without substantially altering the mechanical properties of the lens itself, which would otherwise perform differently. In fact, the bare corneal sensor is at least 7 times thinner than the SCL (> 70 μm-thick) and takes only 8% of the total surface area of the SCL on the peripheral edge to further minimize the effect on overall lens performance. For instance, the corneal sensor was stretched without failure even after the SCL was torn into two pieces at the maximum strain of ~100% (Figure 4.7). The results also show that the monolithically integrated elastomeric connection wire (purple line; E = 420 ± 41 kPa) is virtually as soft as the bare corneal sensor, and therefore should have minimal effect on blinking or eye movements. This wire was stretched up to 350% prior to its mechanical failure, while the relative change in resistance ($\Delta R/R_0$) remained below 2.7 (Figure 4.6b). A representative cross-sectional scanning electron microscope (SEM) image of the wire is shown in Figure 4.8. The mechanical and electrical properties of the wire were negligibly changed after > 1,500 cycles of stretching at 50% (Figure 4.6c, top panel), resulting in well-maintained electrochemical impedance of the corneal sensor (Figure 4.6c, bottom panel). These assessments were consistent with experimental observations by twisting the wire up to 1,440° for more than 1,500 cycles (Figure 4.6d). The electrochemical impedance remained sufficiently low at 18.2 ± 3.8 Ω even against tapping, swinging, and spinning of the connection wire (Figure 4.9), implying that the effect of motion artifacts on signal quality is insignificant.

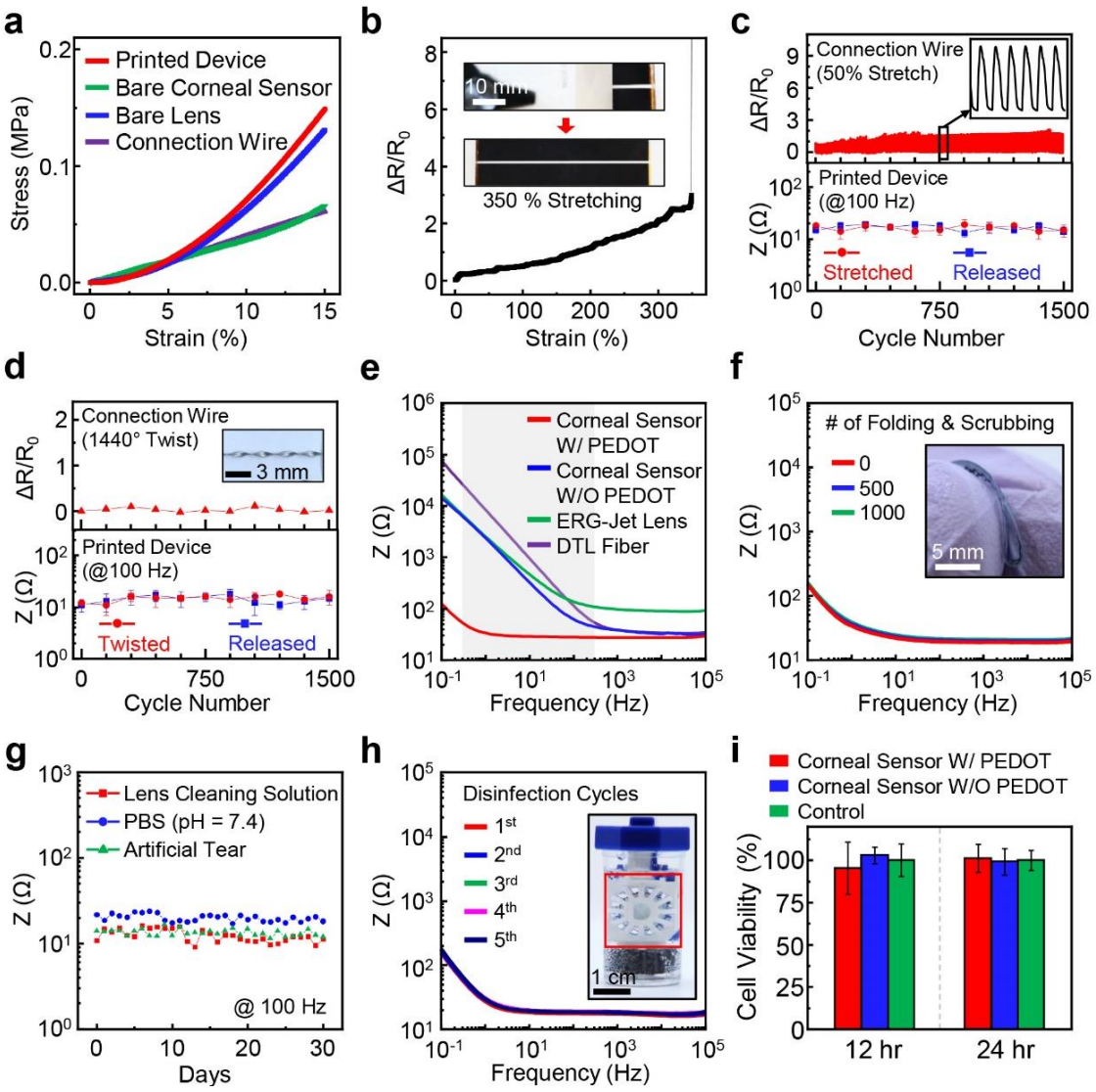

Figure 4.6. (a) Average stress-strain curves for the corneal sensor, the bare corneal sensor (without the SCL), the bare SCL, and the connection wire. (b) Relative change in resistance ($\Delta R/R_0$) of the connection wire under stretching up to 350%. The inset images show the stretched wire. (c) $\Delta R/R_0$ of the connection wire under 1,500 cycles of stretching at 50% (top panel) and the consequent change in the electrochemical impedance of the corneal sensor at every 150 cycles (bottom panel). (d) $\Delta R/R_0$ of the connection wire under 1,500 cycles of twisting up to 1,440° (top panel) and the consequent change in the electrochemical impedance of the corneal sensor at every 150 cycles (bottom panel). (e) Electrochemical impedance of the corneal sensor as a function of frequency by comparison with current clinical standards. (f) Electrochemical impedance of the corneal sensor under 1,000 cycles of folding and scrubbing. (g) Electrochemical impedance of the corneal sensor immersing in several aqueous media for 30 days. (h) Electrochemical impedance of the corneal sensor for 5 cycles of disinfection processes. The inset image shows a commercial cleansing kit filled with a 3% H_2O_2 formula. (i) Cell viability assay of human corneal epithelial cells (HCEpiC) seeded on the corneal sensor with and without a PEDOT layer by comparison with bare control cells.

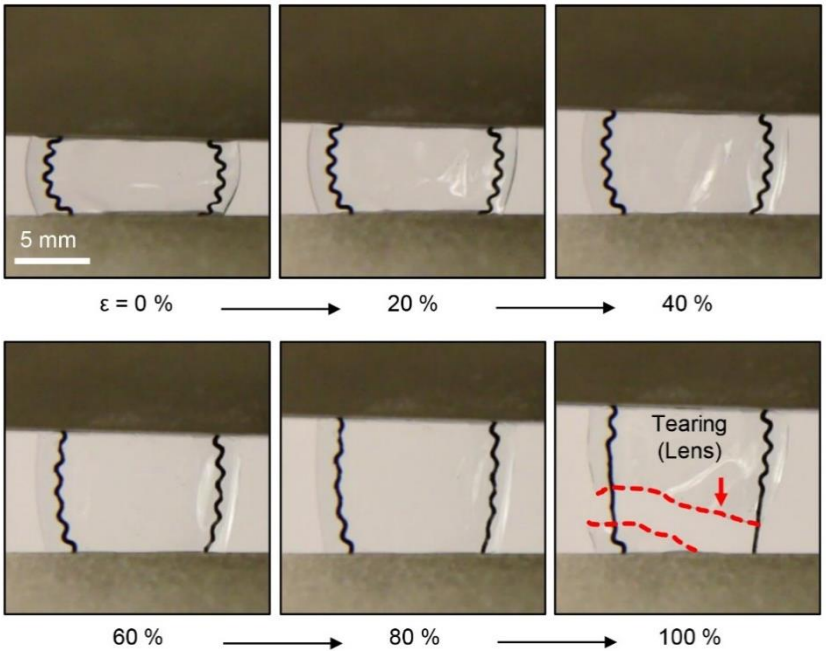

Figure 4.7. A series of photographs for the corneal sensor under stretching until it reaches the failure point.

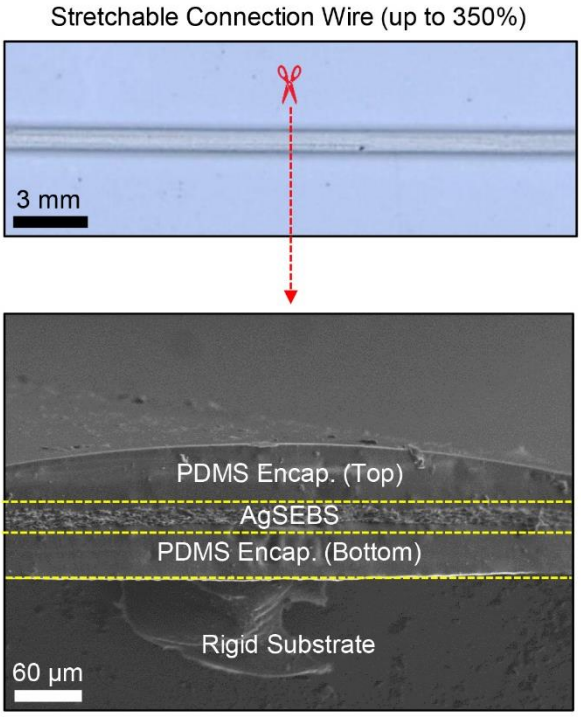

Figure 4.8. Top-view photograph (top inset) and cross-sectional scanning electron microscope (SEM) image (bottom inset) of the connection wire.

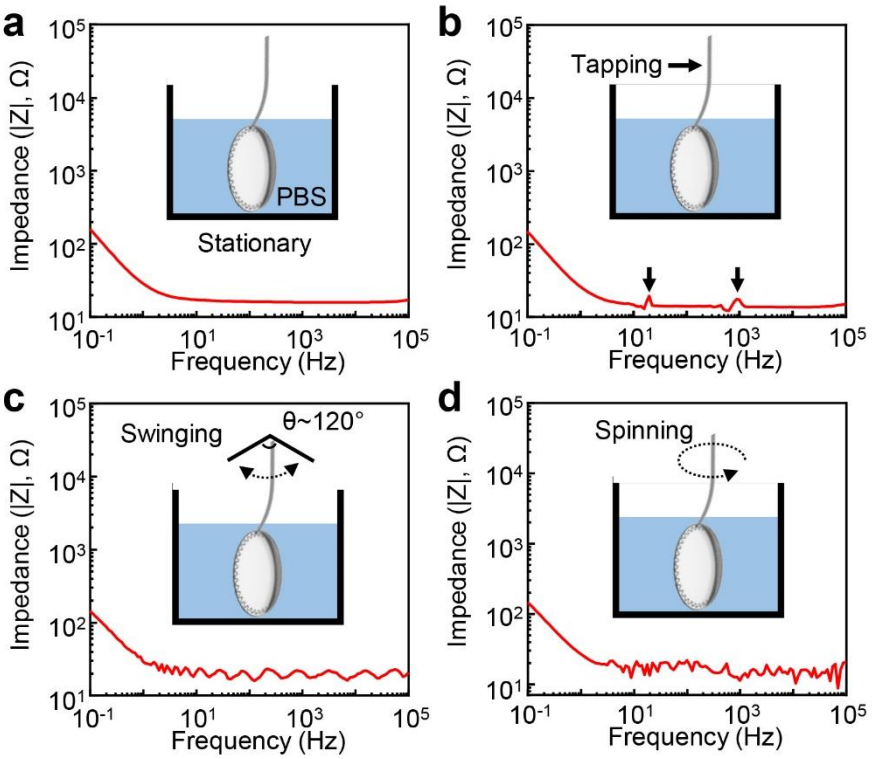

Figure 4.9. Electrochemical impedance of the corneal sensor against tapping, swinging, and spinning of the connection wire, as compared to that under stationary condition.

Figure 4.6e shows experimental measurements for the frequency-dependent electrochemical impedance of the corneal sensor with (red line) and without (blue line) a PEDOT layer in a solution of 1× phosphate buffered saline (PBS, pH = 7.4), by comparison with commonly-used clinical standards, the ERG-Jet lens (LKC Technologies; center lens thickness of 500 μm) and the DTL fiber (Diagnosys; 7 times interwoven fiber with the outer diameter of 0.8 mm).[28] The corneal sensor with a PEDOT layer showed the lowest impedance (< 100 Ω) among the three devices within the typical frequency range of ERG recordings in human eyes (gray highlighted area; 0.3-300 Hz),[29] which would therefore give rise to the high signal-to-noise ratio. These observations were reproducible from device-to-device (Figure 4.9). The impedance of the corneal sensor was nearly unchanged over > 1,000 cycles of folding and scrubbing (Figure 4.6f) and after 30 days of immersion in several aqueous media such as lens cleaning solution (Sensitive Eyes® saline solution, Bausch & Lomb), PBS (pH = 7.4; Gibco), and artificial tear (Refresh Tears® lubricant eye drops, Allergan) at 100 Hz (Figure 4.6g).

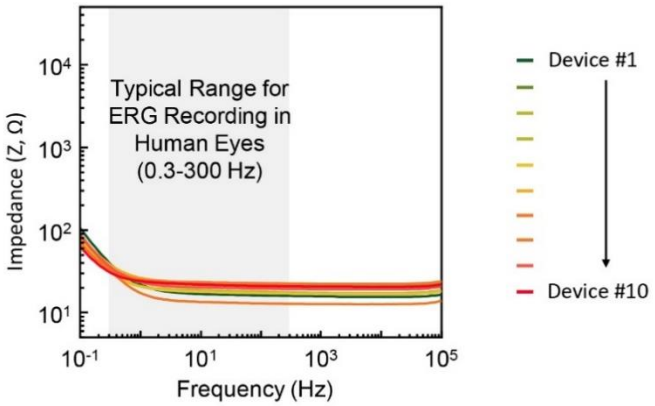

Figure 4.10. Electrochemical impedance of the randomly chosen corneal sensors (n = 10) as a function of frequency. The typical frequency range of ERG recordings in human eyes is highlighted in grey color.

The corresponding results of the impedance as a function of frequency are summarized in Figure 4.11. Figure 4.6h confirms that the impedance was negligibly changed throughout the multiple disinfection cycles (> 5 times) by immersing the corneal sensor in a cleansing kit (inset image) filled with a 3% H_2O_2 formula (ClearCare®, Alcon) for 12 hours each. During these disinfection cycles, no evidence of visual changes in the appearance of the corneal sensor was observed (Figure 4.12). The impedance was also well-maintained under other harsh environmental conditions such as a temperature cycling between 30°C and 80°C and multiple dehydrations in ambient condition for at least 5 hours each (Figure 4.13). The impedance was slightly decreased at high temperature (> 60°C).

Time-dependent cytotoxicity of the corneal sensor to human corneal cell lines is an essential consideration to identify any adverse responses in vitro.[30,31] Figure 4.6i shows a cell viability assay of human corneal epithelial cells (HCEpiC) that were seeded on the surface of the corneal sensor with (red bars) and without (blue bars) a PEDOT layer in a culture medium (EpiGRO™ Human Ocular Epithelia Complete Media, MilliporeSigma) at 37.5°C. For all cases, the cell viabilities were retained over 95% throughout the entire assay period (24 hours) without substantial differences relative to bare control cells (green bars). The results imply that the corneal sensor would provide little risk for the development of corneal inflammation during ERG examination. The results also confirm that there was no residual EDOT present after the washing and disinfecting processes.

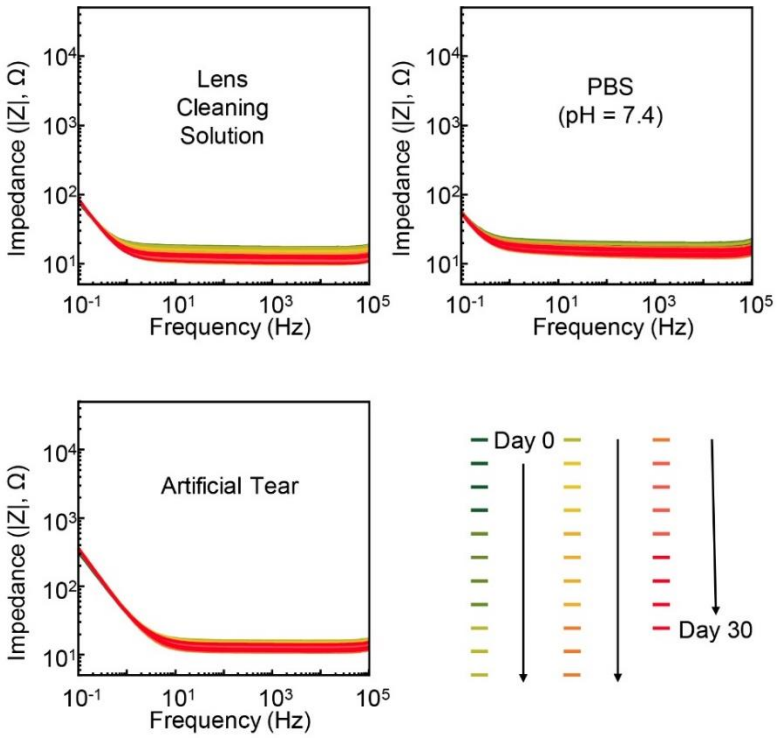

Figure 4.11. Electrochemical impedance of the corneal sensor immersing in a lens cleaning solution (top left graph), PBS (pH = 7.4; top right graph), and artificial tear (bottom left graph) for 30 days.

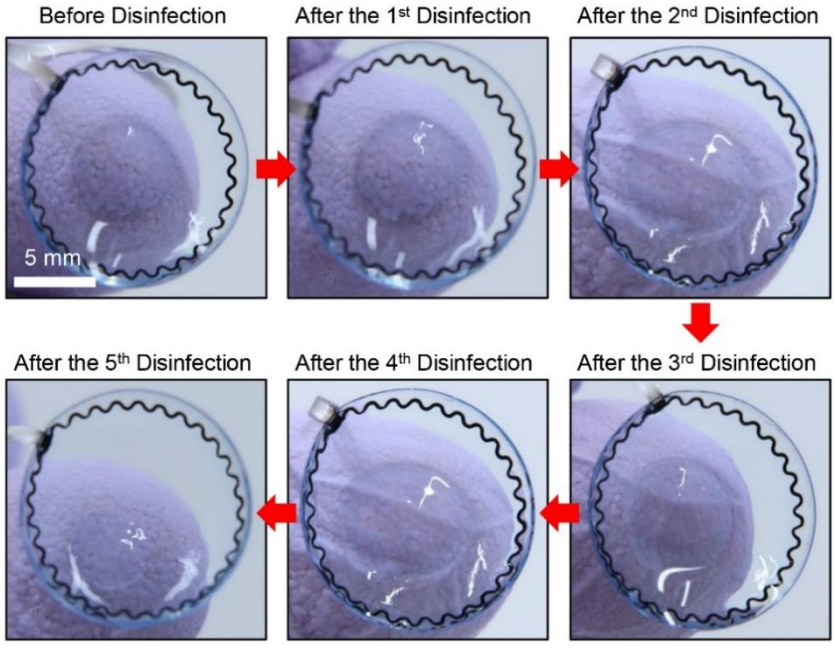

Figure 4.12. A series of photographs of the corneal sensor throughout the 5 cycles of disinfection process using a 3% H_2O_2 formula (ClearCare®, Alcon) over 12 hours each.

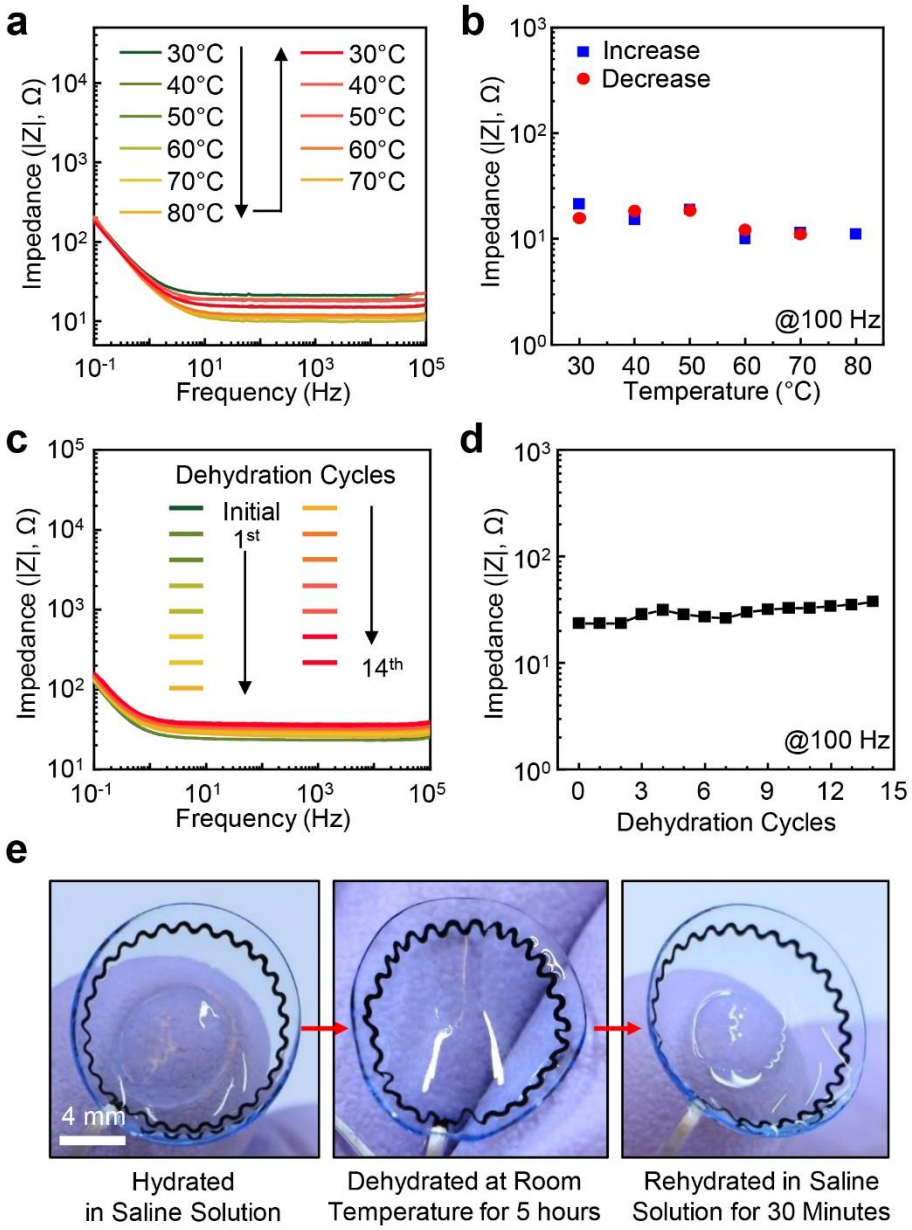

Figure 4.13. (a), Electrochemical impedance of the corneal sensor against a temperature cycling between 30°C and 80°C. (b) The corresponding results with the fixed frequency of 100 Hz. (c) Electrochemical impedance of the corneal sensor against multiple dehydrations in ambient condition for at least 5 hours each. (d) The corresponding results with the fixed frequency of 100 Hz. (e) Optical images of the corneal sensor throughout a cycle of dehydration and rehydration.

4.4.3 Mechanics Analysis under Various Loading Conditions

The low mechanical modulus of the corneal sensor reduces risk for mechanical failure against various loading conditions required for lens handling, cleaning, storage, and fitting. Figure 4.14 summarizes experimental (left column) and finite element analysis (FEA; middle column) results of the corneal sensor under four different loading conditions: (a) flipping, (b) folding, (c) stretching (up to 40%), and (d) expanding (up to 10%). For control comparisons, the corresponding FEA results for the corneal sensor without the SCL is shown in the right column of Figure 4.14. The results show that the maximum principal strain (ε_{max}) of the corneal sensor remained lower than ~10% under these loading conditions. For example, when completely flipped over, the corneal sensor experienced little deformation with the maximum strain of < 1% (Figure 4.14a). When folded in half along the symmetric axis, the maximum strain (< 10%) was concentrated at the folding line of the corneal sensor (Figure 4.14b). When stretched uniaxially and expanded uniformly, the results consistently showed that the maximum strain was remained below 10% (Figure 4.14c, d). For all cases, the maximum strains of the corneal sensor were higher than the bare corneal sensor (without the SCL) by several factors, indicating that the mechanical deformations occurred primarily on the SCL rather than the corneal sensor itself. These findings also imply that the effect of the bare corneal sensor on the intrinsic mechanical properties of the SCL was insignificant.

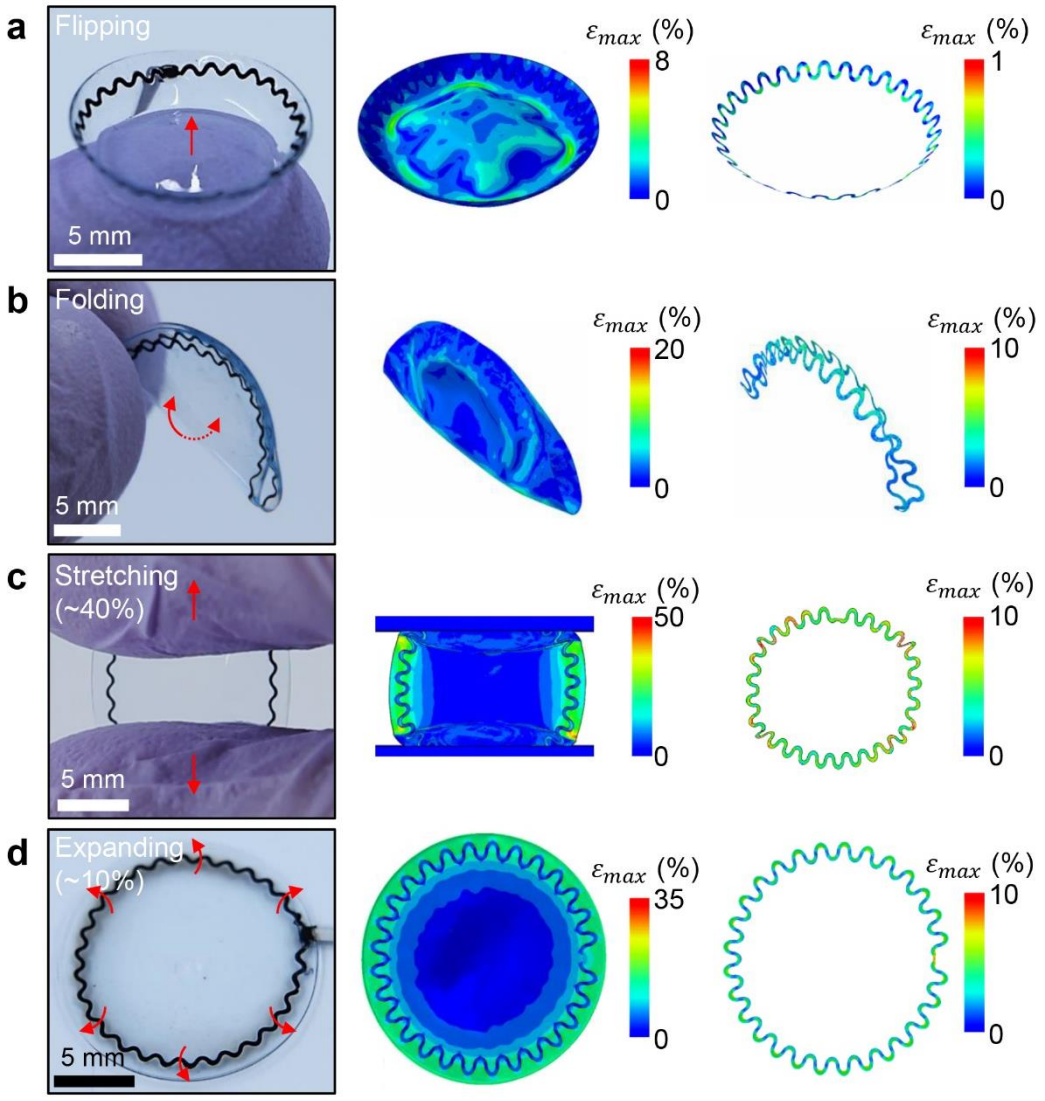

Figure 4.14**.** Photographs (left column) and finite element analysis (FEA) results (middle column) of the corneal sensor under four different loading conditions: (a) flipping, (b) folding, (c) stretching (up to 40%), and (d) expanding (up to 10%). The right column shows the corresponding FEA results of the bare corneal sensor without the SCL.

4.4.4 Real-time ERG Recording in Human Eye

To demonstrate the feasibility and measurement validity in the human eye, a pilot evaluation of the corneal sensor was conducted by clinical research-trained personnel on a healthy adult participant (a 45-year-old male) who had no history of ocular disease. The tests on the human subject were conducted in a university ophthalmic clinic in accordance with Good Clinical Practice (GCP) standards and university regulations. Prior to and following ERG recordings, visual acuity, participant-reported comfort ratings, ocular coherence tomography (Visante, Zeiss), and slit lamp biomicroscopic (SL120, Zeiss) measures of ocular health and lens fit were acquired. The slit lamp biomicroscopic measures were acquired with normal white lights as well as sodium fluorescein installation (1 mg; Fluorets ophthalmic strips, Bausch and Lomb), which highlights any area of damage on the corneal epithelial surface. The ERG recordings were acquired with the corneal sensor and two comparator controls; the ERG-Jet lens and DTL fiber.[28]

Figure 4.15a demonstrates the process of ERG recordings where the participant was seated upright in front of a Ganzfeld stimulator (RETI-port/scan 21, Roland Consult), which generated a series of short wavelength stimuli in low luminance conditions (~0.001 cd m^{-2}).[29] The corneal sensor was inserted on the left eye of the participant without topical anesthesia or a speculum, and the participant was asked to blink normally. Biomicroscopic examination revealed a mobile, well-fit lens with good centration, coverage, and movement (Figure 4.15b, top panel). Both the corneal sensor and the connection wire had little impact on blinking or eye movements with the gaze angle of up to ± 40° (which most commonly occur), resulting that the lens movements were as smooth as a bare SCL. In a temporal gaze larger than these angles (which is not common in normal eye movements), the wire temporarily adhered to the wet conjunctival epithelium and prevented the lens from continuing to rotate with the eye. This impact could be minimized by selective inferior placement of the wire. For control comparisons, the ERG-Jet lens and the DTL fiber were also tested on the same eye of the participant, and thereby can eliminate the effect of different size and shape of human eyeballs on ERG signals (Figure 4.15b, middle and bottom panels, respectively).[32] In this study, the Burian-Allen ERG electrode was not included due to the high discomfort and low tolerance experienced by the participant. Prior to the implementation of the ERG-Jet lens, the eye was anesthetized with one drop of 0.5% proparacaine hydrochloride and then moistened with 0.5% methylcellulose in order to reduce discomfort. No speculum was used, but the participant was not able to fully blink with the lens in

due to the 4 built-in anterior bumps (yellow circles; 1.5 mm-wide and 2.5 mm-long each) preventing complete eyelid closure.[6] The base curve radius of the lens was 7.9 mm, which is slightly flat relative to the central corneal curvature of the participant (7.7 mm). Care was taken to ensure adequate alignment of the lens over the pupil center during measurements, but as is typical for any rigid lens, it moved around 1-1.5 mm on the eye.[33] As the last control measure, the DTL fiber was gently placed across the bulbar conjunctiva above the lower eyelid without topical anesthesia.[34] Figure 4.15c shows representative images of anterior segment ocular coherence tomography (AS-OCT), confirming the conformational alignment of the corneal sensor with the cornea upon insertion (middle inset) and after 1 hour of the wear (right inset). On the other hand, the corresponding AS-OCT images using the ERG-Jet lens could not be acquired due to the unstable contact of the device to the anterior corneal surface and the built-in bumps preventing axial instrument focus. Participant-reported comfort was assessed prior to and during each use of the devices employing a simple 100-point numeric scale,[31,35] where a rating of '1' represented extremely uncomfortable/intolerable and a rating of '100' perfectly comfortable/not noticeable at all. Prior to testing, the participant provided a rating of 95 with his habitual soft contact lenses (Dailies Aqua Comfort Plus, Alcon), compared with a rating of 98 with no contact lens at all. The DTL fiber was given a rating of 88 versus the corneal sensor of 86 (both without topical anesthesia). Alternatively, the ERG-Jet lens with topical anesthesia was given a numeric rating of 42.

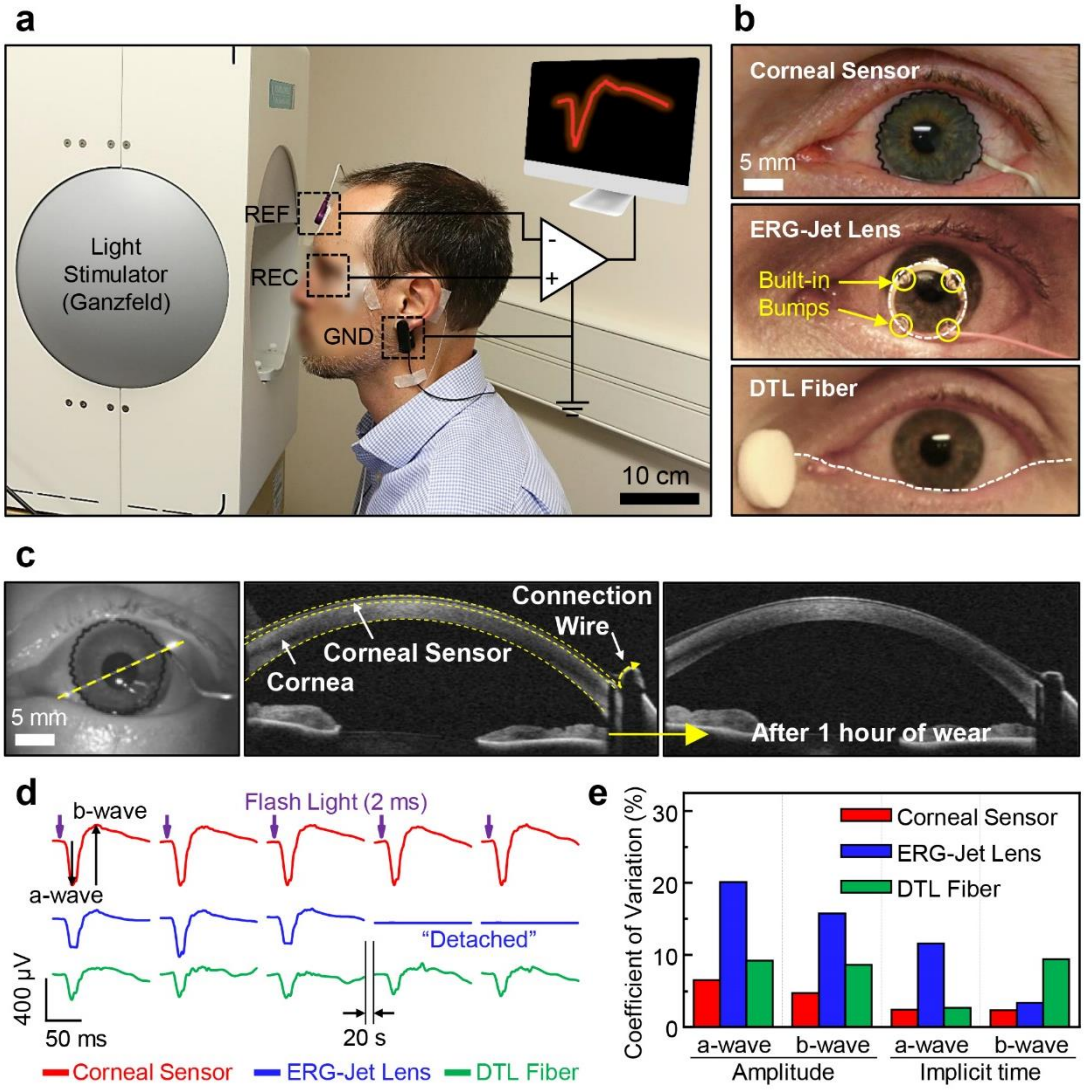

Figure 4.15. (a) Measurement setting for ERG recordings using a Ganzfeld stimulator in scotopic conditions. (b) Photographs of the eye worn with the corneal sensor (top panel) by comparisons with the ERG-Jet lens (middle panel) and DTL fiber (bottom panel). The yellow circles denote the 4 built-in bumps of the ERG-Jet lens. The white dotted line denotes the outer trace of the DTL fiber. (c) Photograph (left inset) and the corresponding anterior segment ocular coherence tomography (AS-OCT) images of the corneal sensor worn on the cornea upon insertion (middle inset) and after 1 hour of the wear (right inset). (d), Full-field ERG signals acquired from the three different devices under the light intensity of 10.0 $cd \cdot s \cdot m^{-2}$. (e) Coefficient of variation (CV) of the amplitudes and implicit times of the a- and b-waves extracted from at least 8 recordings.

These pilot tests revealed the following important findings. (i) The corneal sensor conformed well to the cornea when on the eye, whereas the ERG-Jet lens created a gap between the corneal sensor and the cornea of about 500 μm (the sum of the lens thickness and a thick aqueous tear layer between the posterior lens and anterior cornea) due to its relatively flat

curvature. (ii) The corneal sensor remained centered on the cornea, whereas the ERG-Jet lens was systematically decentered. (iii) The corneal sensor was rated to be much more comfortable and easier to use than the ERG-Jet lens even without the use of topical anesthesia, and in line with the DTL fiber that was not in contact with the cornea. (iv) The external connection wire of the corneal sensor was thin (120 µm-thick), lightweight (1.4 $mg \cdot cm^{-1}$), and sufficiently soft (E = 420 kPa) enough to avoid any interruption from blinking and eye movements. On the other hand, the polyvinyl chloride (PVC)-coated lead cable of the ERG-Jet lens was considerably thicker (0.6 mm-dia.), heavier (8.6 $mg \cdot cm^{-1}$), and stiffer (E = 1.3 GPa), making it difficult to align the lens to the pupil center and capture consistent ERG signals. These experimental observations obtained with the ERG-Jet lens and the DTL fiber are consistent with previous reports.[11,28,36]

Following application of the devices, and prior to ERG recording, the participant was asked to sit in the low luminance room (< 0.001 $cd \cdot m^{-2}$) for at least 20 minutes. The participant was then asked to gaze at a fixation spot inside the Ganzfeld bowl to maintain a constant amount of light transmission to the retina and minimize interference that could be generated upon ocular movements.[37] The participant's head was kept within 5 cm from the Ganzfeld bowl opening. The pupil size was continuously monitored using an infrared (IR) camera inside the Ganzfeld dome (Figure 4.16).

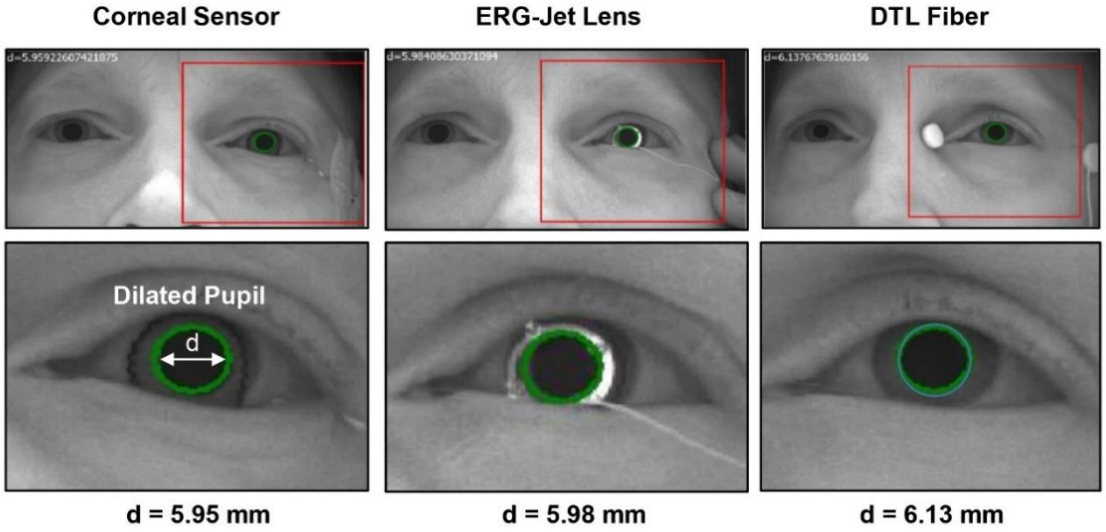

Figure 4.16. Representative IR images of the left eye of the participant worn with the corneal sensor (left column) by comparisons with the ERG-Jet lens (middle column) and the DTL fiber (right column). The diameter of the fully dilated pupil is noted below each image.

Figure 4.15d shows representative ERG signals obtained by consecutively illuminating a white flashing stimulus (10.0 $cd \cdot s \cdot m^{-2}$) for 2 milliseconds at the interval of 20 seconds to allow the pupil to fully dilate again. For all devices, the results showed typical scotopic ERG waveforms with characteristic a-wave (i.e., the first negative wave reflecting the function of photoreceptor) and b-wave (i.e., the following positive wave reflecting the activity of rod bipolar cells).[38] The corresponding coefficient of variation (CV) of the amplitudes and implicit times of the ERG waveforms is summarized in Figure 4.15e. It is clear that the corneal sensor provided the highest signal amplitude of the a- and b-waves, while the measurements were most consistent (CV < 6.4%) without noticeable blinking artifacts (Table 4.1). These results suggest that the corneal sensor was more intimately interfaced with the corneal surface than other devices, despite blinking and eye movements. By contrast, the measurements with the ERG-Jet lens were unstable, resulting in the highest CV (> 15.7%) in amplitudes. In addition, the use of corneal anesthetic agents might further reduce the amplitudes and prolong the implicit times.[39,40] As expected, the DTL fiber showed the lowest amplitude signals due to the far distance away from the cornea, and the measurements were prone to variations by blinking artifacts (CV > 10% in amplitudes).

Table 4.1. Comparisons of the average amplitudes and implicit times of the a- and b-waves extracted from full-field ERG signals acquired using the three different devices used in this study. The corresponding coefficient of variation (CV) for each amplitude and implicit time is noted.

		This Work	ERG-Jet	DTL Fiber
a-wave	Amplitude CV*	402.6 µV 6.4%	296.4 µV 20.1%	219.2 µV 9.2%
	Implicit Time CV	18.3 ms 2.4%	20.1 ms 11.6%	17.3 ms 2.6%
b-wave	Amplitude CV	557.4 µV 4.7%	374.5 µV 15.7%	276.5 µV 8.6%
	Implicit Time CV	54.1 ms 2.3%	52.8 ms 3.3%	51.8 ms 9.3%

The visual acuity of the participant (20/15) remained unchanged prior to and following testing with each of the devices. Upon slit lamp biomicroscopic examination with sodium fluorescein installation prior to testing, the participant had only minor, non-clinically significant superficial punctate staining (common to minor end of day dryness with soft lens wear).

Following wear of the corneal sensor for > 1 hour, the punctate staining had resolved. However, a non-clinically significant minor indentation arcuate staining (~1 mm in extent) was present in one quadrant of the superior cornea which mirrored the location and orientation of the serpentine trace of the corneal sensor. This staining resolved within 2 hours post lens removal.

4.4.5 Standard Full-field ERG Recording in Human Eye

The international society for clinical electrophysiology of vision (ISCEV) standard for full-field clinical ERG signals specifies 6 responses based on the adaptation state of human eyes and the flash strength: (i) Dark-adapted 0.01 ERG (rod ERG), (ii) Dark-adapted 3.0 ERG (combined rod-cone standard flash ERG), (iii) Dark-adapted 3.0 oscillatory potentials, (iv) Dark-adapted 10.0 ERG (strong flash ERG), (v) Light-adapted 3.0 ERG (standard flash 'cone' ERG), and (vi) Light-adapted 30 Hz flicker ERG.[41] The ISCEV encourages the use of additional ERG protocols for testing beyond the minimum standard for clinical ERG signals, which are abbreviated as Dark 0.01, Dark 3.0, Dark OP, Dark 10.0, Light 3.0, and Light Flicker, respectively. The standard ERG waveforms with characteristic amplitudes and implicit times are noted in Figure 4.18.

Figure 4.17a shows representative measurement results of the standard full-field ERG signals that were sequentially measured using the corneal sensor (red lines) by comparison with the ERG-Jet lens (blue lines) and the DTL fiber (green lines).[28] The ERG recordings by using the corneal sensor showed consistent results of the highest amplitudes throughout the entire testing period (typically no more than 30 minutes), while providing better comfort of wear than other devices. The detailed analyses of the each full-field ERG waveform are shown in Methods section. Figure 1.17b shows a summary of the average amplitudes (left column) and implicit times (right column) obtained from at least 8 repeated recordings for each ERG protocol. The results obtained from a one-way analysis of variance (ANOVA) confirm that the amplitudes of the corneal sensor were significantly higher than those of other devices ($p < 0.0001$), while the implicit times remained statistically unchanged.

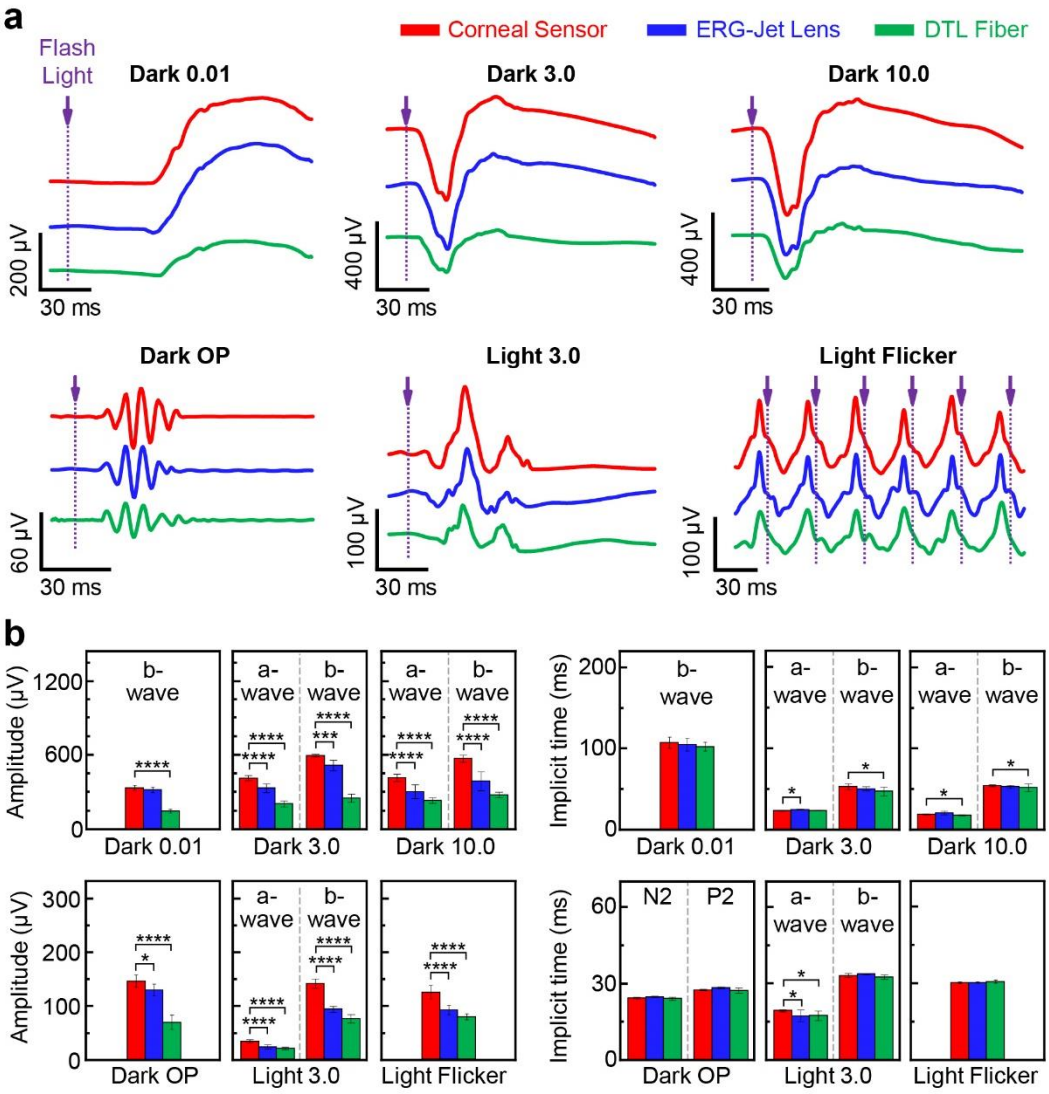

Figure 4.17. (a) ISCEV standard full-field ERG signals acquired from the corneal sensor (red lines) by comparisons with those obtained using the ERG-Jet lens (blue lines) and DTL fiber (green lines). (b) Summary of average amplitudes (left column) and implicit times (right column) extracted from each ERG protocol. For data analysis, a one-way analysis of variance (ANOVA) method with Tukey's post hoc test was used. Significance was set at ****$p < 0.0001$, ***$p < 0.001$, **$p < 0.01$, *$p < 0.1$.

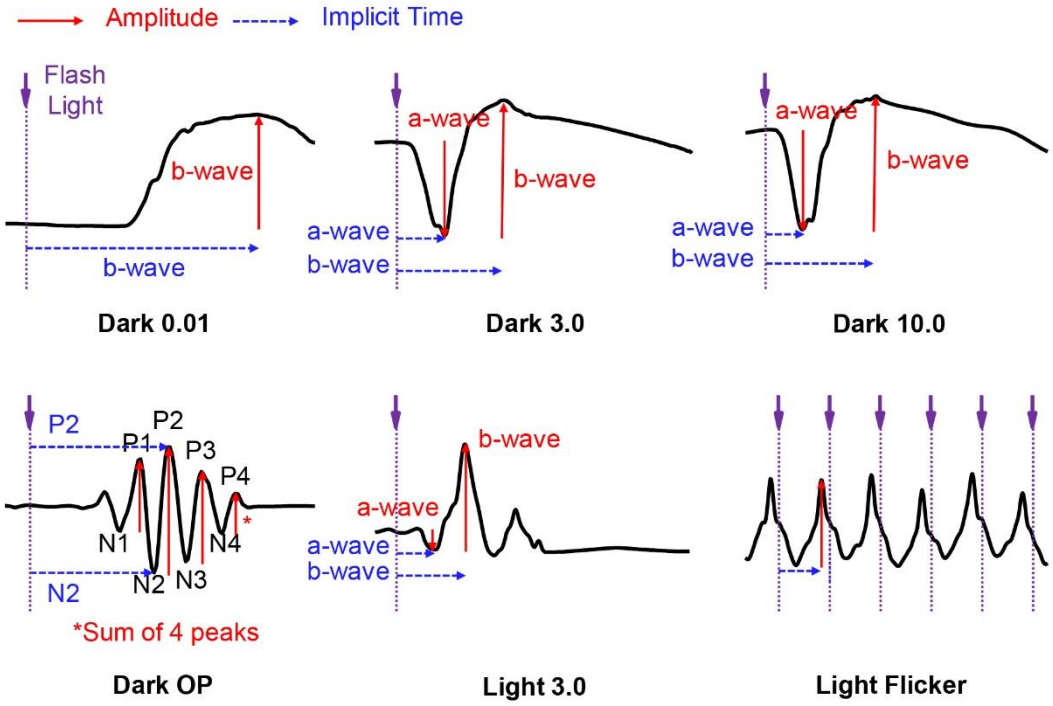

Figure 4.18. The amplitudes (red lines) and implicit times (blue lines) of the a- and b-waves obtained from each ERG protocol are noted. Purple dotted lines indicate the moment of flashing light. In case of the Dark OP, the amplitude is considered as the sum of the 4 red arrows.

The outcomes reported here establish a straightforward mean that enables turning common commercially available disposable SCLs into a functional corneal sensor tailored for *ophthalmic* electrodiagnostic testing in human eyes. The resulting device is thin and deformable and can be printed on a SCL without substantially altering its intrinsic properties in terms of biocompatibility, softness, oxygen permeability, transparency, wettability, and ergonomic curvature. A strategy that utilizes an electrochemical anchoring of the device to SCLs provides a guideline to enhance the mechanical robustness and chemical stability, in order to meet the requirements for lens fitting, handling, cleaning, and disinfection. The use of commercially available SCLs allows the device to form a conformal, seamless contact to the cornea of human eyes, and therefore provides superior comfortability and safety compared to current clinical standards (e.g., the ERG-Jet lens and the Burian-Allen lens). The findings from the first-in-human validation study confirm the ability of the device in high-fidelity recording of standard full-field ERG signals with high signal-to-noise ratio. Importantly, this is accomplished in a manner that allows for natural blinking and eye movements, without the need of topical

anesthesia or use of a speculum. Moreover, the fabrication of the device involves the use of an automated dispenser-printing method that facilitates the exploration of high-throughput batch production, potentially making the final product disposable and affordable for widespread adoption in the future. This work produces a first-of-its-kind corneal sensor platform that may be also tailored for a broad range of ophthalmic and optometric clinical needs such as the continuous monitoring of eye movement and intraocular pressure.[42–44]

4.5 References

(1) Young, B.; Eggenberger, E.; Kaufman, D. Current Electrophysiology in Ophthalmology: A Review. *Curr. Opin. Ophthalmol.* **2012**, *23* (6), 497–505.

(2) Scholl, H. P. N.; Zrenner, E. Electrophysiology in the Investigation of Acquired Retinal Disorders. *Surv. Ophthalmol.* **2000**, *45* (1), 29–47.

(3) Senger, C.; Moreto, R.; Watanabe, S. E. S.; Matos, A. G.; Paula, J. S. Electrophysiology in Glaucoma. *J. Glaucoma* **2020**, *29* (2), 147–153.

(4) Parkinson, J.; Tremblay, F. Obtaining a Contact Lens Acquired Electroretinogram in the Presence of Topical Anesthetic Hypersensitivity. *Doc. Ophthalmol.* **2008**, *116* (3), 245–249.

(5) Mentzer, A. E.; Eifler, D. M.; Montiani-Ferreira, F.; Tuntivanich, N.; Forcier, J. Q.; Petersen-Jones, S. M. Influence of Recording Electrode Type and Reference Electrode Position on the Canine Electroretinogram. *Doc. Ophthalmol. 2006 1112* **2006**, *111* (2), 95–106.

(6) Brodie, S. E. Modified ERG-Jet™ Contact Lens Electrodes for Use in Infants and Toddlers—Update. *Doc. Ophthalmol.* **2018**, *137* (3), 203–205.

(7) Brodie, S. E. Tips and Tricks for Successful Electroretinography in Children. *Curr. Opin. Ophthalmol.* **2014**, *25* (5), 366–373.

(8) Coupland, S. G.; Janaky, M. ERG Electrode in Pedriatic Patients: Comparison of DTL Fiber, PVA-Gel, and Non-Corneal Skin Electrodes. *Doc. Ophthalmol. 1989 714* **1989**, *71* (4), 427–433.

(9) Woo, J.; Jung, S.; Gauvin, M.; Lachapelle, P. The DTL ERG Electrode Comes in Different Shapes and Sizes: Are They All Good? *Doc. Ophthalmol.* **2017**, *135* (2), 155–164.

(10) Esakowitz, L.; Kriss, A.; Shawkat, F. A Comparison of Flash Electroretinograms Recorded from Burian Allen, JET, C-Glide, Gold Foil, DTL and Skin Electrodes. *Eye* **1993**, *7* (1), 169–171.

(11) Rahmani, S.; Ban, T.; Patangay, S.; Park, J. C.; McAnany, J. J.; Hetling, J. R. Evaluation of a Soft, Disposable, Conformal ERG Lens Electrode Prototype vs. Burian-Allen Lens and DTL Fiber Electrodes. *Invest. Ophthalmol. Vis. Sci.* **2017**, *58* (8), 4890–4890.

(12) Mohidin, N.; Yap, M. K. H.; Jacobs, R. J. Electrodes for Multifocal Electroretinography (MfERG): A Comparison of Four Electrodes Types (Elektrod Untuk Elektroretinografi Multifokal (MfERG): Perbandingan Empat Jenis Elektrod). *Sains Malaysiana* **2014**, *43* (7), 1089–1094.

(13) Principles and Practice of Clincial Electrophysiology of Vision. **2006**.

(14) Yin, R.; Xu, Z.; Mei, M.; Chen, Z.; Wang, K.; Liu, Y.; Tang, T.; Priydarshi, M. K.; Meng, X.; Zhao, S. Soft Transparent Graphene Contact Lens Electrodes for Conformal Full-Cornea Recording of Electroretinogram. *Nat. Commun.* **2018**, *9* (1), 1–11.

(15) Wei, S.; Yin, R.; Tang, T.; Wu, Y.; Liu, Y.; Wang, P.; Wang, K.; Mei, M.; Zou, R.; Duan, X. Gas-Permeable, Irritation-Free, Transparent Hydrogel Contact Lens Devices with Metal-Coated Nanofiber Mesh for Eye Interfacing. *ACS Nano* **2019**, *13* (7), 7920–7929.

(16) Vásquez Quintero, A.; Verplancke, R.; De Smet, H.; Vanfleteren, J. Stretchable Electronic Platform for Soft and Smart Contact Lens Applications. *Adv. Mater. Technol.* **2017**, *2* (8), 1700073.

(17) Sapkota, K.; Franco, S.; Lira, M. Daily versus Monthly Disposable Contact Lens: Which Is Better for Ocular Surface Physiology and Comfort? *Contact Lens Anterior Eye* **2018**, *41* (3), 252–257.

(18) Vidal-Rohr, M.; Wolffsohn, J. S.; Davies, L. N.; Cerviño, A. Effect of Contact Lens Surface Properties on Comfort, Tear Stability and Ocular Physiology. *Contact Lens Anterior Eye* **2018**, *41* (1), 117–121.

(19) Sekine, S.; Ido, Y.; Miyake, T.; Nagamine, K.; Nishizawa, M. Conducting Polymer Electrodes Printed on Hydrogel. *J. Am. Chem. Soc.* **2010**, *132* (38), 13174–13175.

(20) Kim, B. G.; Lim, J. H.; Kim, J. Y.; -, al; Frances Glover, C.; Watson, T.; Bryant, D.; Obeidat, A. M.; Rastogi -, A. C.; Asplund, M.; et al. Toxicity Evaluation of PEDOT/Biomolecular Composites Intended for Neural Communication Electrodes. *Biomed. Mater.* **2009**, *4* (4), 045009.

(21) He, H.; Zhang, L.; Guan, X.; Cheng, H.; Liu, X.; Yu, S.; Wei, J.; Ouyang, J. Biocompatible Conductive Polymers with High Conductivity and High Stretchability. *ACS Appl. Mater. Interfaces* **2019**, *11* (29), 26185–26193.

(22) Wang, S.; Xu, J.; Wang, W.; Wang, G. J. N.; Rastak, R.; Molina-Lopez, F.; Chung, J. W.; Niu, S.; Feig, V. R.; Lopez, J.; et al. Skin Electronics from Scalable Fabrication of an Intrinsically Stretchable Transistor Array. *Nat. 2018 5557694* **2018**, *555* (7694), 83–88.

(23) Wehner, M.; Truby, R. L.; Fitzgerald, D. J.; Mosadegh, B.; Whitesides, G. M.; Lewis, J. A.; Wood, R. J. An Integrated Design and Fabrication Strategy for Entirely Soft, Autonomous Robots. *Nat. 2016 5367617* **2016**, *536* (7617), 451–455.

(24) Vafaiee, M.; Vossoughi, M.; Mohammadpour, R.; Sasanpour, P. Gold-Plated Electrode with High Scratch Strength for Electrophysiological Recordings. *Sci. Reports 2019 91* **2019**, *9* (1), 1–11.

(25) Sim, K.; Chen, S.; Li, Z.; Rao, Z.; Liu, J.; Lu, Y.; Jang, S.; Ershad, F.; Chen, J.; Xiao, J.; et al. Three-Dimensional Curvy Electronics Created Using Conformal Additive Stamp Printing. *Nat. Electron. 2019 210* **2019**, *2* (10), 471–479.

(26) Takamatsu, T.; Chen, Y.; Yoshimasu, T.; Nishizawa, M.; Miyake, T.; Takamatsu, T.; Chen, Y.; Yoshimasu, T.; Miyake, T.; Nishizawa, M. Highly Efficient, Flexible Wireless-Powered Circuit Printed on a Moist, Soft Contact Lens. *Adv. Mater. Technol.* **2019**, *4* (5), 1800671.

(27) Lee, C. H.; Ma, Y.; Jang, K. I.; Banks, A.; Pan, T.; Feng, X.; Kim, J. S.; Kang, D.; Raj, M. S.; McGrane, B. L.; et al. Soft Core/Shell Packages for Stretchable Electronics. *Adv. Funct. Mater.* **2015**, *25* (24), 3698–3704.

(28) Yin, H.; Pardue, M. T. Performance of the DTL Electrode Compared to the Jet Contact Lens Electrode in Clinical Testing. *Doc. Ophthalmol. 2004 1081* **2004**, *108* (1), 77–86.

(29) Robson, A. G.; Nilsson, J.; Li, S.; Jalali, S.; Fulton, A. B.; Tormene, A. P.; Holder, G. E.; Brodie, S. E. ISCEV Guide to Visual Electrodiagnostic Procedures. *Doc. Ophthalmol.* **2018**, *136* (1), 1–26.

(30) Horwath-Winter, J.; Simon, M.; Kölli, H.; Trummer, G.; Schmut, O. Cytotoxicity Evaluation of Soft Contact Lens Care Solutions on Human Conjunctival Fibroblasts. *Ophthalmologica* **2004**, *218* (6), 385–389.

(31) Vijay, A. K.; Fadli, Z.; Lakkis, C.; Coles-Brennan, C.; Willcox, M. D. P. In Vitro Compatibility of Contact Lenses with Corneal Epithelial Cells. *Eye Contact Lens* **2018**, *44*, S283–S290.

(32) McAllan, A.; Sinn, J.; Aylward, G. W. The Effect of Gold Foil Electrode Position on the Electroretinogram in Human Subjects. *Vision Res.* **1989**, *29* (9), 1085–1087.

(33) Wolffsohn, J. S.; van der Worp, E.; de Brabander, J.; Bakker, E.; Bangma, I.; Beerten, R.; Beks, P. A. C.; Bennett, E.; Bliekendaal, J.; Borst, W.; et al. Consensus on Recording of Gas Permeable Contact Lens Fit. *Contact Lens Anterior Eye* **2013**, *36* (6), 299–303.

(34) Hébert, M.; Vaegan; Lachapelle, P. Reproducibility of ERG Responses Obtained with the DTL Electrode. *Vision Res.* **1999**, *39* (6), 1069–1070.

(35) Kollbaum, P. S.; Jansen, M. E.; Rickert, M. E. Comparison of Patient-Reported Visual Outcome Methods to Quantify the Perceptual Effects of Defocus. *Contact Lens Anterior Eye* **2012**, *35* (5), 213–221.

(36) García-García, Á.; Muñoz-Negrete, F. J.; Rebolleda, G. Variability of the Multifocal Electroretinogram Based on the Type and Position of the Electrode. *Doc. Ophthalmol.* **2016**, *133* (2), 99–108.

(37) Shimada, Y. Electrooculogram Artifacts in Long Flash Electroretinogram Recordings. *Invest. Ophthalmol. Vis. Sci.* **2018**, *59* (9), 5027–5027.

(38) Gauvin, M.; Lina, J. M.; Lachapelle, P. Advance in ERG Analysis: From Peak Time and Amplitude to Frequency, Power, and Energy. *Biomed Res. Int.* **2014**, *2014*.

(39) Tremblay, F.; Parkinson, J. E.; Lalonde, M. R. Anesthesia and Electroretinography. *Invest. Ophthalmol. Vis. Sci.* **2003**, *44* (13), 1897–1897.

(40) Tremblay, F.; Parkinson, J. E. Alteration of Electroretinographic Recordings When Performed under Sedation or Halogenate Anesthesia in a Pediatric Population. *Doc. Ophthalmol. 2003 1073* **2003**, *107* (3), 271–279.

(41) McCulloch, D. L.; Marmor, M. F.; Brigell, M. G.; Hamilton, R.; Holder, G. E.; Tzekov, R.; Bach, M. ISCEV Standard for Full-Field Clinical Electroretinography (2015 Update). *Doc. Ophthalmol.* **2015**, *130* (1), 1–12.

(42) Kim, J.; Cha, E.; Park, J. U. Recent Advances in Smart Contact Lenses. *Adv. Mater. Technol.* **2020**, *5* (1), 1900728.

(43) Pompe, M. T.; Liasis, A.; Hertle, R. Visual Electrodiagnostics and Eye Movement Recording - World Society of Pediatric Ophthalmology and Strabismus (WSPOS) Consensus Statement. *Indian J. Ophthalmol.* **2019**, *67* (1), 23.

(44) Ho, C. H.; Wong, J. K. W. Role of 24-Hour Intraocular Pressure Monitoring in Glaucoma Management. *J. Ophthalmol.* **2019**, *2019*.

5. SMART SOFT CONTACT LENSES FOR CONTINUOUS 24-HOUR MONITORING OF INTRAOCULAR PRESSURE IN GLAUCOMA CARE*

5.1 Abstract

Continuous monitoring of intraocular pressure, particularly during sleep, remains a grand challenge in glaucoma care. Here we introduce a class of smart soft contact lenses, enabling the continuous 24-hour monitoring of intraocular pressure, even during sleep. Uniquely, the smart soft contact lenses are built upon various commercial brands of soft contact lenses without altering their intrinsic properties such as lens power, biocompatibility, softness, transparency, wettability, oxygen transmissibility, and overnight wearability. We show that the smart soft contact lenses can seamlessly fit across different corneal curvatures and thicknesses in human eyes and therefore accurately measure absolute intraocular pressure under ambulatory conditions. We perform a comprehensive set of in vivo evaluations in rabbit, dog, and human eyes from normal to hypertension to confirm the superior measurement accuracy, within-subject repeatability, and user comfort of the smart soft contact lenses beyond current wearable ocular tonometers. We envision that the smart soft contact lenses will be effective in glaucoma care.

5.2 Introduction

Glaucoma - often called the “silent thief of sight” - gradually steals vision without early warning sign or pain, and it remains the leading cause of irreversible blindness worldwide.[1,2] Currently, the only intervention to delay glaucoma progression is to lower the intraocular pressure (IOP) of eyes under ocular hypertension, and thereby, minimize optic nerve damage (i.e., vision loss).[3,4] Clinical trials in lowering IOP with topical ocular hypotensive medications have been successful in reducing the risk of developing glaucoma.[5,6] However, the rhythm of IOP varies by postural change under ambulatory conditions over both nyctohemeral (i.e., 24-hour) and seasonal (i.e., monthly) periods wherein overnight IOP is typically greater than daytime IOP in a supine position.[7] In turn, ocular hypertension may occur during sleep, without the patient noticing it, even if daytime in-clinic or at-home measurements indicate normal IOP (i.e., 10−21 mmHg). Therefore, glaucoma patients and suspects can benefit from evaluating the

* This work was published in Nature Communications online on September 20, 2022.

24-hour rhythm of IOP on a daily to weekly to monthly basis at home. However, none of current ocular tonometers are effective in continuously monitoring IOP beyond clinic hours, particularly during sleep.

The Goldmann applanation tonometry (GAT) is regarded as the current gold standard for in-clinic IOP measurements, but the need for routine clinic visits remains a significant burden and also has become a particular challenge throughout the ongoing global pandemic.[8] Portable handheld ocular tonometers, such as the I-Care Home (I-Care, Inc.), enable the at-home monitoring of IOP, but their overnight use remains limited particularly during sleep due to the requirement of patients to stay awake during measurements.[9,10] Wearable ocular tonometers, such as the TriggerFish lens (Sensimed, Inc.), enable the continuous monitoring of IOP in both in-clinic and at-home settings, but their long-term use in human eyes remains impeded particularly during sleep due to side effects including foreign body sensation, eye pain, superficial punctate keratitis, corneal epithelial defects, and conjunctival erythema.[11] Moreover, these wearable ocular tonometers are typically equipped with an integrated circuit (IC) chip for wireless communications that is formed on a rigid and stiff semiconductor wafer (i.e., like a piece of glass), thereby posing discomfort and safety risks particularly during sleep.[12]

Ongoing research endeavors enable several types of smart contact lenses by integrating functional nanomaterials (e.g., graphene and metallic nanowires) with contact lenses made of biocompatible polymers (e.g., hydrogel silicones, Parylene-C, and SU-8 resins).[13–20] These smart contact lenses have shown initial success at the laboratory scale, but their pragmatic implementation into human eyes remains impeded due to the lack of mechanical durability (for lens handling and inadvertent eye rubbing), chemical stability (for daily lens cleaning and disinfecting), oxygen transmissibility (for long-term wear), and ergonomic design (for lens fitting in human eyes with different corneal shapes and sizes).[21,22] Moreover, most current smart contact lenses are still necessarily equipped with the stiff IC chip for wireless communications, which would thereby inevitably pose discomfort and safety risks in human eyes particularly during sleep.

On the other hand, there exist various commercial brands of soft contact lenses using ophthalmically compatible silicone hydrogels that offer a high quality of biocompatibility (i.e., FDA-cleared), softness (i.e., 0.2-2 MPa), transparency (i.e., $\geq$ 99%), oxygen transmissibility (i.e., 10-200 Dk t-1), wettability or water content (i.e., 30-80%), ergonomic curvature (i.e., 8.3-9.0

mm in base curve radii), and overnight wearability.[23] These soft contact lenses can seamlessly fit a variety of corneal shapes and sizes in human eyes without significant safety concerns for those even with glaucoma, other ocular diseases, or post-incisional surgeries.[24] Yet, it is currently challenged to fabricate a wireless ocular tonometer on commercial soft contact lenses due to the requirement of high temperatures and corrosive chemicals in current microfabrication processes that are traditionally designed for inorganic materials. Thus, there remains a critical opportunity to extend the applicability of commercial soft contact lenses into a safe and effective sensing platform for the human eye, particularly for the continuous 24-hour monitoring of IOP in glaucoma care. In this work, we introduce a unique class of smart soft contact lenses (SSCL) where a highly soft, thin, and stretchable ocular tonometer is built upon various commercial brands of soft contact lenses for the continuous 24-hour monitoring of IOP even during sleep at home. Importantly, the SSCL will retain the intrinsic lens features including (1) lens power, biocompatibility, softness, transparency, wettability, and oxygen transmissibility for user comfort and clear vision; (2) overnight wearability for continuous IOP monitoring even during sleep; (3) ergonomic curvature fitting across different corneal shapes and sizes in human eyes for high measurement accuracy and within-subject repeatability; (4) mechanical and chemical durability against daily lens cleaning, disinfecting, fitting, and handling for long-term routine use; and (5) disposability after multiple uses through low-cost batch production for wide adoption in clinical practice. Having all these features at the same time is crucial to the success of translating the SSCL into glaucoma care but lacks in current wearable ocular tonometers.

5.3 Methods

All the research in this paper complies with all relevant ethical regulations. Animal procedures adhered to the Association for Research in Vision and Ophthalmology statement for the Use of Animals in Ophthalmic and Vision Research, and were approved by the Purdue Animal Care and Use Committee (protocol number: 2104002136). All human studies were conducted with the presence of clinical research-trained personnel in accordance with Good Clinical Practice (GCP) standards, university regulations, and approved Institutional Review Board (IRB protocol #: 2004308902) at Indiana University.

5.3.1 Device Fabrication

A glass slide (Dow Corning) was cleaned by sonication in a bath of acetone and isopropyl alcohol for 30 minutes each and then exposed to ultraviolet ozone for 10 minutes. A water-soluble polyvinyl alcohol (PVA) solution (10 wt% of Mowiol 4-88 in deionized water) was spin cast on the glass slide at 1,000 rpm for 30 seconds and annealed at 100 °C for 30 minutes. In parallel, the printable PDMS ink was prepared by mixing base solutions (Dowsil SE 1700 & Sylgard 184, Dow Corning, Inc.) and a curing agent with a weight ratio of 5:5:1. The printable AgSEBS ink was prepared by (1) dissolving SEBS (1.5 g; H1221, Asahi Kasei, Inc.) in tetrahydrofuran (1.5 g; Sigma Aldrich, Inc.) and 1,2-dichlorobenzene (4 g; Sigma Aldrich, Inc.) and then (2) mixing with Ag flakes (8 g; average particle size of 2−5 μm; Inframat Advanced Materials, Inc.) using a planetary centrifugal mixer (Thinky, ARE-310). The printable Silbione ink was prepared by mixing A and B components of Silbione® RT Gel4717 (Bluestar Silicones). The as-prepared inks were directly printed into a series RLC resonant circuit (i.e., ocular tonometer) on the glass slide with a water-soluble PVA layer using an automated nozzle injection system (Nordson EFD) equipped on a three-axis computer-controlled translation stage (resolution ≥ 100 μm in line width; repeatability = ± 3 μm; nozzle speed ≤ 4 mm sec^{-1}) as shown in Figure 5.1.[25]

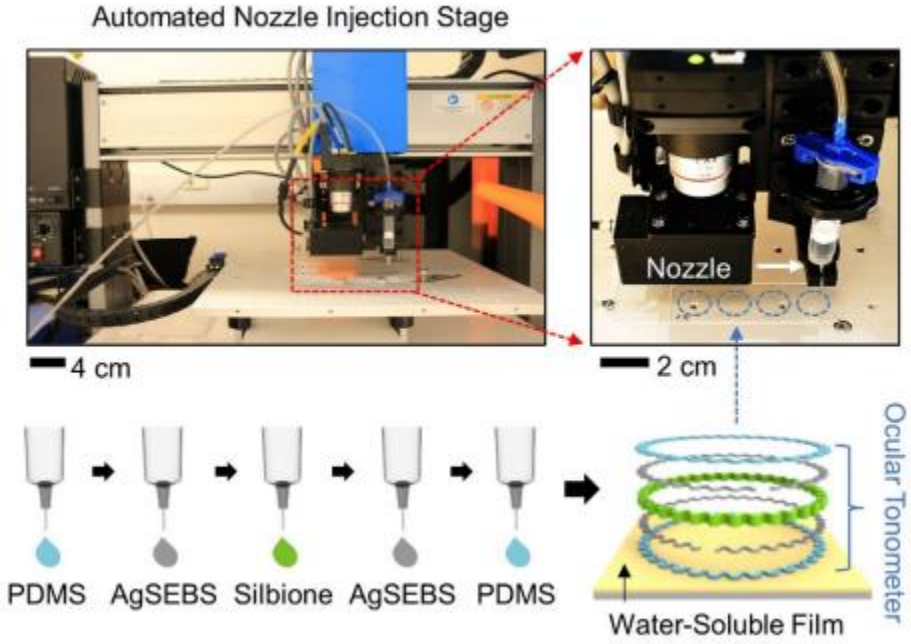

Figure 5.1. Photographs (top panel) and schematic images (bottom panel) of the automated nozzle injection process.

The resulting structure was then immersed in a bath of deionized water to dissolve the PVA layer, allowing the ocular tonometer to be released from the glass slide. The ocular tonometer was placed afloat on the surface of an aqueous reservoir (pH = 8.5) containing a 2 mg of dopamine-hydrochloride per milliliter of 10 mM Tris buffer (Figure 5.2). After approximately 12 hours, thermal annealing was applied at 60 ºC for 30 minutes to complete the in-situ polymerization of the dopamine-hydrochloride into a thin layer of PDA. Here, the serpentine shape of the ocular tonometer was stretched when interfaced with the curved surface of the soft contact lens, which thereby formed an intimate contact at the interface.[26–29] The resulting SSCL was immersed in a saline solution for 30 minutes and also washed with a preservative-free saline solution (Renu; Bausch & Lomb, Inc.). Prior to each test, the SSCL was disinfected with a disinfecting care solution (Clear Care; Alcon Laboratories, Inc.) for at least 6 hours. The surface topology and thickness of the SSCL were characterized using an optical microscope (Eclippse LV100; Nikon, Inc.) and SEM (S-4800; Hitachi, Inc.), respectively. For comparisons, several different types of commercial soft contact lenses were tested in this study, including (1) Air Optix Night & Day Aqua (Alcon, Inc.); (2) Acuvue Oasys (Johnson & Johnson, Inc.); (3) Biofinity (CooperVision, Inc.); and (4) Dailies Total 1 (Alcon, Inc.).

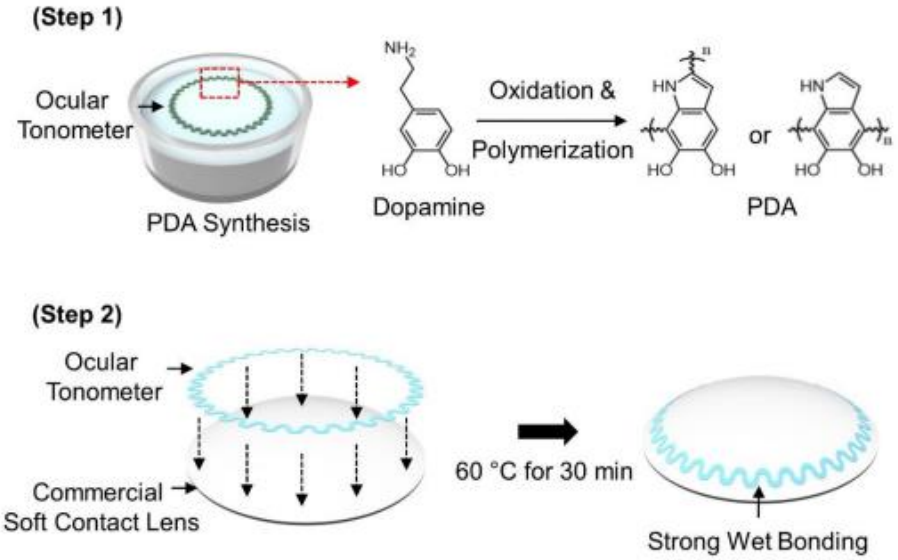

Figure 5.2. Schematic illustrations for the polymerization of dopamine into a PAD adhesive on the bottom surface of the ocular tonometer (top panel) and the subsequent bonding process onto a commercial soft contact lens.

5.3.2 Benchtop Evaluations

Standard tensile tests were conducted to determine the elastic moduli of the SSCL, its bare soft contact lens, and the internal ocular tonometer (without a soft contact lens). The specimens were loaded on the chuck of a tensile testing machine (ESM303, Mark-10) and then stretched from 0 to 15% at the elongation rate of 10−25% per minute. The stress was computed by the equation:

$$\sigma = FD^{-1}T^{-1}$$

Where F is the measured force during the elongation; and D and T are the diameter and thickness of the specimen, respectively. A total of 5 measurements were taken and averaged for each sample. For the measurement of the capacitive response, the SSCL was connected to a LCR meter (E4980AL; Keysight, Inc.) via a conducting (i.e., AgSEBS) wire while increasing the pressure by applying weights (3.3 g or 2.5 mmHg). The capacitive sensitivity (S) of the SSCL is defined by:

$$S = \frac{\delta((C_2 - C_1)/C_0)}{\delta(P_2 - P_1)}$$

Where C_2 and C_1 are the capacitance acquired at sampling events 2 and 1, respectively; C_0 is the initial capacitance; and P_2 and P_1 are the pressure acquired at sampling events 2 and 1, respectively. For the measurement of the relative resistance change, the SSCL was connected to a source meter (Keithley 2400; Keysight, Inc.) via a conducting (i.e., AgSEBS) wire during cyclic stretching up to 10,000 times at the applied strain of 25% and 50% with the elongation rate of 5% per second, respectively. The relative resistance change of each specimen was defined by:

$$R_{\text{Rel}} = \Delta R/R_0$$

Where ΔR is the difference between current resistance and initial resistance; and R_0 is the initial resistance value.

5.3.3 Gas Permeability Tests

The gas permeability of the SSCL was assessed by measuring water vapor transmission.[30] Vials filled with a 1 ml of deionized water were covered with the dehydrated SSCL and the dehydrated bare soft contact lenses of various commercial brands. The gap between the vials and specimens was sealed with a Kapton® tape. For comparison, vials filled with the same amount of

deionized water were also left uncovered and fully covered with a VHB^{TM} tape (3M, Inc.). The weight loss of the water in each vial was measured for 186 hours with an interval of approximately 24 hours. A total of 3 measurements were taken and averaged for each specimen.

5.3.4 Adhesive Strength Measurements

The adhesive strength of the PDA adhesive from the bare soft contact lens was measured using a custom-modified mechanical peeling apparatus (ESM303; Mark-10; high-resolution force gauge of ± 0.25%). The bare soft contact lens was cut into the dimension of 4 × 10 mm and bonded onto the PDMS substrate (i.e., the encapsulation layer of the SSCL) using the PDA adhesive. The PDMS substrate was fixed on a horizontal stage of the mechanical peeling apparatus with a double-sided Kapton tape. The specimen was then pulled vertically at a speed of 0.4 mm sec^{-1}. During the peeling test, both the peeling displacement and force were recorded. A total of 7 measurements were taken and averaged for each specimen. The peeling strength was defined by:

$$W = \frac{F}{L}$$

Where F is the applied force; and L is the contact length. The measurements of the specimens were repeated after (1) disinfecting with a cleansing kit containing a 3% hydrogen peroxide (H_2O_2) cleansing solution (Clear Care; Alcon, Inc.) for 12 hours; (2) dehydrating in an ambient environment (relative humidity = 40%; temperature = 25 °C) for 5 hours; and (3) over-heating in a saline solution maintained at 75 °C for 30 minutes.

5.3.5 Extreme Use Condition Tests

The change in the baseline resonant frequency of the SSCL were monitored against various user mishandling conditions. A total of 3 specimens were tested for 5 cycles of each condition. A total of 6 measurements were taken and averaged for each iteration. For the mechanical deformation tests, the specimens were repeatedly flipped, rubbed, folded, and stretched using an automated tensile testing machine (ESM303, Mark-10) for up to 1,000 times each. In the flipping tests, the specimens were fixed under the tensile testing machine by two grips. Upper and lower probes were driven downwards and upwards by the tensile test machine at a pre-programed speed of 180 mm min^{-1}. In the rubbing tests, the specimens were conformally

fitted on a plastic artificial eyeball (Tanlee) which was fixed on the lower grip of the tensile testing machine. An artificial finger covered with a latex glove was connected to the upper grip and positioned to be in contact with the marginal region of the specimens. The artificial finger was driven to repeatedly rub the surface of the internal ocular tonometer at a speed of 120 mm min^{-1}. In the folding tests, the lower and upper margins of the specimens were fixed by the lower and upper grip of the tensile testing machine, respectively. The specimens were repeatedly folded at the applied strain of 50% through the cyclic linear motion of the upper grip at a speed of 120 mm min^{-1}. In the stretching tests, the specimens were repeatedly stretched at the applied strain of 15% through the cyclic linear motion of the upper grip at a speed of 120 mm min^{-1}. During the measurements, the specimens were constantly hydrated by applying a saline solution in every 10 minutes. For the disinfecting and cleaning tests, the specimens were repeatedly disinfected and cleaned for up to 5 times with 3% H_2O_2 cleansing solution (Clear Care; Alcon, Inc.) and cleaning saline solution (Renu; Bausch & Lomb, Inc.), respectively. For the dehydrating tests, the specimens were placed in an ambient condition (relative humidity = 40%; temperature = 25 °C) for 1 hour and then rehydrated in a saline solution for 20 minutes. For the overheating tests, the specimens were repeatedly heated in an oven at 75 °C for 30 minutes and then rested at room temperature for 1 hour. For the overcooling tests, the specimens were placed in a refrigerator at -4 °C for 30 minutes and then rested at room temperature for 1 hour.

5.3.6 *Ex Vivo* Evaluations in Enucleated Pig Eyes

The enucleated pig eyes (n = 3) were horizontally placed on the table. The central corneal thickness and the corneal curvature of the pig eyes were measured using a pachymeter (Pachmate 2; DGH) and Keratometer, respectively. The anterior chamber of the pig eyes was cannulated with a needle for injecting or removing a saline solution to increase or decrease IOP. A pressure transducer (V6402; Smiths medical, Inc.) was used to monitor the IOP of the eyes as a reference. An infusion needle was connected to a microfluidic syringe pump system (Ultra Micro Pump 3; WPI) to dynamically control the IOP of the pig eyes by the amount of the injected saline. The pressure transducer was connected to a data acquisition platform (USB-6343; National Instruments, Inc.) to instantaneously transport the data to an external computing unit. The real-time IOP variation was plotted using a MATLAB script. The SSCL was conformally fitted on the cornea of the pig eye with a reader coil fixed above the SSCL at a proximity of < 10 mm. The

reader coil was connected to a VNA (FieldFox Handheld Analyzer 9913A; Keysight Technologies, Inc.) to constantly acquire the frequency spectra of the reflection (S11) from the SSCL. Prior to each measurement, the IOP of the pig eyes was stabilized at 6 mmHg for 1 minute. The IOP was increased by the microfluidic syringe pump at an interval of 4 mmHg until the IOP reached 38 mmHg. After stabilizing at 38 mmHg for 1 minute, the IOP was decreased by the microfluidic syringe pump at an interval of 4 mmHg until the IOP reached 6 mmHg. A total of 6 measurements were taken and averaged at each step. The responsivity of the SSCL was defined by:

$$R = |\frac{\partial f}{\partial P}|_{P = P_{\min}}$$

where f is the resonant frequency; P is the IOP value; and $P_{\min}$ is the minimum IOP value. The sensitivity of the SSCL was defined by:

$$S = \frac{R}{f(P = P_{\min})}$$

where R is the responsivity; and $f(P = P_{\min})$ is the resonant frequency at the measured minimum IOP value.

5.3.7 Cell Viability Tests

The specimens (n = 5 each) were sterilized with a mixture of ethanol and distilled water (70:30 v/v) for 30 minutes; rinsed with Dulbecco's PBS (Gibco); and dehydrated with ultraviolet irradiation for 1 hour. The specimens were then placed inside a 24-well plate on a concave side facing upwards. Human corneal epithelial cells (HCEpiC; MilliporeSigma, Inc.) with the density of 1×10^5 per well were seeded on the specimens in a cell media (EpiGRO™ Human Ocular Epithelia Complete Media; MilliporeSigma, Inc.) and then incubated at 37.5 °C with 5% carbon dioxide (CO_2) for 24, 48 and 72 hours. At each time point, recurring well plates from the experiment and control group were taken out from the incubator for cell viability measurement. A 3-(4,5-dimethylthiazol-2-yl)-2,5-diphenyltetrazolium bromide (MTT; MilliporeSigma, Inc.) reagent was added to each well plate and incubated for 3 hours; the cell media was removed; and the cells were lysed with dimethylsulfoxide (ATTC). The light absorbance of each well was measured using a microplate reader (Synergy™ NEO; BioTek, Inc.) at a wavelength of 575 nm. The cell viability values were obtained by normalizing the absorbance values with those of the

control groups. The statistical analysis was carried out using a one-way ANOVA method ($^{****}p < 0.0001$) with the Tukey's post hoc test implemented in the Origin software (OriginLab) and are expressed as averages ± s.e.m ($n = 5$).

5.3.8 *In Vivo* Evaluations in Rabbit Eyes

All animal procedures adhered to the Association for Research in Vision and Ophthalmology statement for the Use of Animals in Ophthalmic and Vision Research and were approved by the Purdue Animal Care and Use Committee (protocol number: 2104002136). A total of 6 female New Zealand white rabbits (6-month-old; Envigo Global Services, Inc.) were included. The rabbits were housed in an animal facility with a 12-hour light/dark cycle. Total 4 out of 6 rabbits were used for the 24-hour biocompatibility study. The SSCL was fitted on one eye while its bare soft contact lens was fitted on the contralateral eye. Complete ophthalmic examinations including Schirmer tear test (Schirmer tear test strip; Merck Animal Health, Inc.), tear film breakup time, fluorescein staining (Ful-Glol; Akorn, Inc.), tonometry (iCare Tonovet Plus; iCare, Inc.), slit lamp biomicroscopy (SL-17; Kowa, Inc.), and indirect ophthalmoscopy (Keeler, Inc.) were performed prior to and after the 24-hour wear of the SSCL and its bare soft contact lens. Any noted abnormality was recorded using a modified Mcdonald-Shadduck semi-quantitative scoring system.[31] AS-OCT (Spectralis; Heidelberg Engineering, Inc.) images were obtained after approximately 1 hour of wearing the SSCL to confirm their conformational alignment with the cornea. After the SSCL or its bare soft contact lens was fitted, the eyelids were partially sutured closed (i.e., partial temporary tarsorrhaphy) with a 4-0 nylon (Ethilon; Ethicon, Inc.). The rabbits were individually housed in each cage and allowed for normal daily activities for 24 hours. The rest of 2 rabbits were used for the 2-week biocompatibility study. Following the baseline complete ophthalmic examinations, the SSCL was fitted on one eye while the contralateral eye served as untreated control. The SSCL was maintained on the eyes for 8 hours per day for 2 weeks. A new clean SSCL was used each day. The rabbits were individually housed in each cage and allowed for normal daily activities. The eyes were monitored daily to inspect for any sign of irritation or inflammation. Complete ophthalmic examinations were followed on days 3, 7, and 14 as compared to their baseline results. At the end of the 24-hour and 2-week biocompatibility studies, the rabbits were humanly euthanized. The eyes and adnexa including upper, lower, and the third eyelids were collected. The collected tissues were routinely

fixed, processed in paraffin, sectioned, and stained with H&E for histopathological analysis and reporting. The histopathology was assessed with a masked fashion using a semi-quantitative scoring system ranging from 0 to 4 (no lesions, minimal, mild, moderate, severe).[32]

5.3.9 *In Vivo* Evaluations in Dog Eyes

All animal procedures adhered to the Association for Research in Vision and Ophthalmology statement for the Use of Animals in Ophthalmic and Vision Research and were approved by the Purdue Animal Care and Use Committee (protocol number: 2104002136). The SSCL was calibrated with the iCare Tonovet Plus in a dog eye (female beagle; 10 months old) to generate an empirical equation with a linear curve fitting. For calibration, the IOP of the dog was monitored with the iCare Tonovet Plus followed by the SSCL in an interval of 2 hours after applying a drop of IOP-lowering medication (0.005% Latanoprost; Bausch & Lomb, Inc.) following the first measurement. A total of 6 measurements were taken and averaged at each time interval to obtain an empirical linear fit. On a different day, the IOP of the dog was continuously monitored for 24 hours using the SSCL and the iCare Tonovet Plus in an interval of 20 minutes. The dogs were not sacrificed. The dog was easier to handle over rabbits for IOP monitoring particularly under ambulatory conditions.

5.3.10 Heat Generation in Long-Term Operation

An enucleated pig eye was horizontally placed with the SSCL fitted on its cornea. A reader coil was placed above the SSCL in a proximity of 5 mm and also connected to a portable VNA. The pig eye was monitored using a high-resolution infrared (IR) camera (A300; FLIR) while the SSCL was under long-term operation for 12 hours.

5.3.11 Ocular Coherence Tomography (OCT)

The OCT images were acquired prior to and during the application of the SSCL or its bare soft contact lens. The data acquisition was made in corneal high-resolution mode at 16 meridians (e.g., slices).

5.3.12 Slit Lamp Biomicroscopy

The movement and centering of the SSCL on human eyes during typical eye activities were evaluated using a slit lamp biomicroscope (SL120; Zeiss). A millimeter reticle in the ocular microscope was utilized for measurements, which was calibrated at ×10 magnification. The eye movements in nasal, temporal, superior, and inferior directions as well as a blink and lens lag upon primary and up gaze lens were evaluated and compared with those of wearing its bare soft contact lens. Prior to and after the application of the SSCL in human eyes, the ocular health of the anterior segment eye (e.g., lids, lashes, conjunctiva, cornea) was also evaluated by a slit lamp biomicroscope examinations with and without sodium fluorescein (1 mg; Fluorets ophthalmic strips; Bausch and Lomb, Inc.). A cobalt blue light was applied. Sodium fluorescein staining was used on the eye before and after 6 hours of wearing the SSCL to stain dead or devitalized cells of the cornea and conjunctiva. Magnifications ranging from ×10 to ×16 were used.

5.3.13 Visual Field Tests

Visual field extent of human eyes was quantified for the naked eye and the same eye wearing the SSCL. The visual field extent was measured using the Octopus 900 Kinetic Perimeter (Haag-Streit) with a III4e target (i.e., area = 64 mm^2; luminance = 318 cd m^{-2}) moving at 5^o per second.

5.3.14 Human Subject Studies

All human studies were conducted with the presence of clinical research-trained personnel in accordance with Good Clinical Practice (GCP) standards, university regulations, and approved Institutional Review Board (IRB protocol #: 2004308902). The human research participants consented to the publication of photos. There was no participant compensation. A total of 3 adult participants (i.e., ages of 46, 32, and 23) were included. The measurements with the SSCL and the iCare Home were completed within 2 hours to avoid unwanted variations of IOP by nyctohemeral rhythm. At each posture, the data was collected after the IOP of each subject was stabilized by staying still and relaxed for 5 minutes. A total of 6 measurements were taken and averaged at each posture for both opened and closed eyes. A total of 4 devices were applied on participant 1; and 1 device was applied on participant 2 and 3 each. The continuous

monitoring of the IOP for participant 1 was conducted at sitting posture by the SSCL and the GAT for 6 hours in an interval of 2 hours. A total of 6 measurements were taken and averaged for each data point. The measurements with the Triggerfish lens on each subject were conducted at the same time of a day on the second day of the measurement with the SSCL to minimize the unwanted variations of IOP by nyctohemeral rhythm. At each posture, the participants stayed still and relaxed until the IOP data was collected automatically in every 5 minutes by the Triggerfish lens. An empirical linear calibration equation was obtained using the SSCL from the participants by capturing the dynamic change of the IOP in response to various body postures including sitting, standing, supine, right lateral, left lateral, and prone. For calibration, the IOP values of the participants were also obtained using the iCare Home at each body posture.

5.4 Results and Discussion

5.4.1 Device Configuration and Working Principle

Figure 5.3a shows the layered schematic view of the SSCL. The internal ocular tonometer is comprised of intrinsically soft and stretchable elastomers, including: (1) polydimethylsiloxane (PDMS) for biocompatible encapsulation; (2) polystyrene-b-poly(ethylene-ran-butadiene)-b-polystyrene (SEBS) embedded with silver (Ag) flakes (AgSEBS) for conducting traces; and (3) Silbione liquid silicone rubber (Bluestar Silicones; East Brunswick, Inc.) with the mechanical modulus (E) of ~5 kPa for a highly compressible dielectric interlayer. These elastomers were directly printed into a series resistor-inductor-capacitor (RLC) resonant circuit through the use of an automated nozzle injection system (Nordson EFD) equipped on a three-axis computer-controlled translation stage (Figure 5.1) in a rapid high-throughput manner (i.e., ≥ 30 units per batch within 30 minutes of printing).

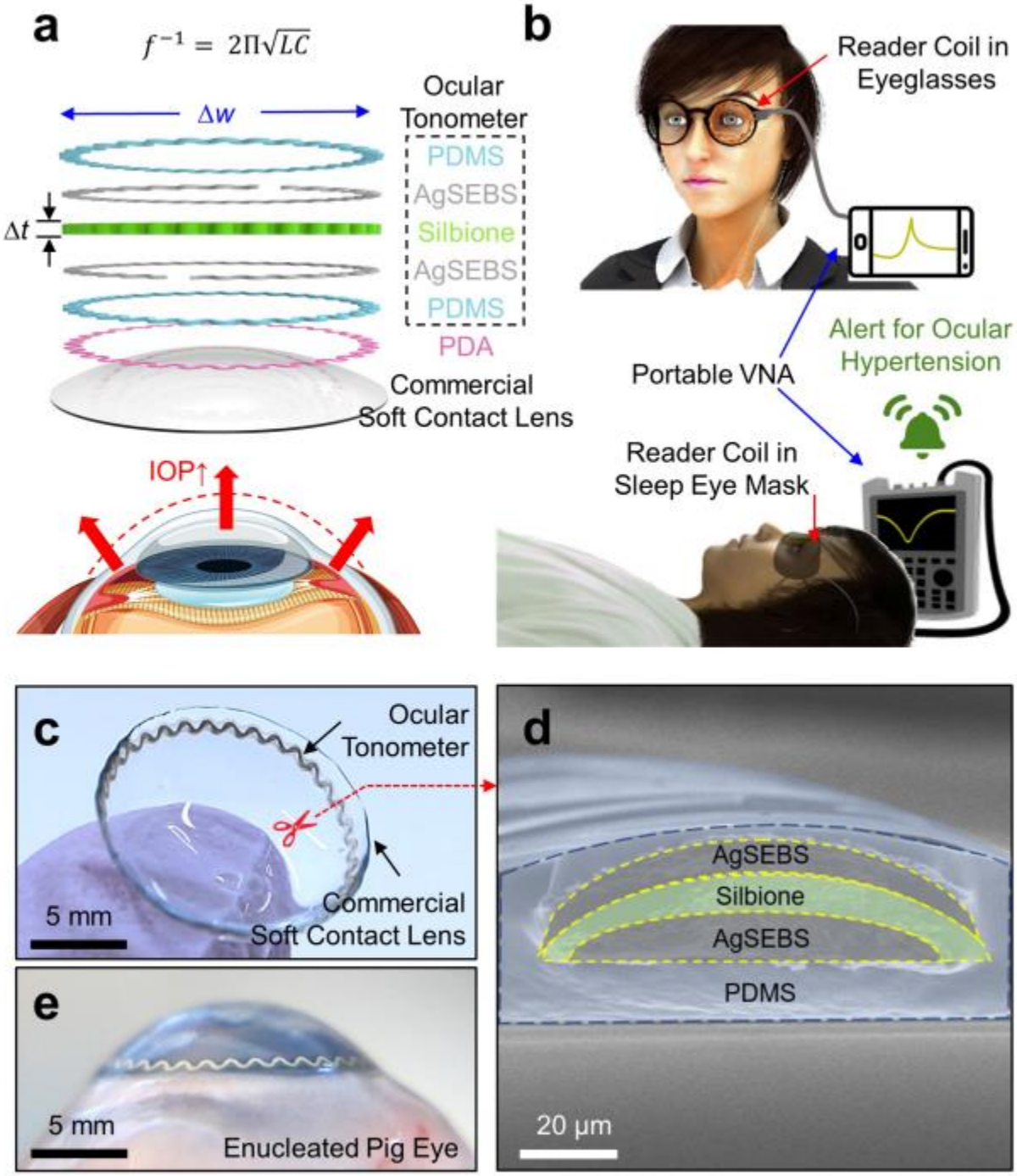

Figure 5.3. Schematics and optical images of the SSCL. (a) Layered schematic view of the SSCL. (b) Data acquisition scheme for the monitoring of daytime (top panel) and nighttime (bottom panel) IOP. (c) Photograph of the SSCL. (d) Cross-sectional SEM image of the SSCL. e Photograph of the SSCL in an enucleated pig eye.

The resulting ocular tonometer was then bonded onto the outer surface of the soft contact lens through the in-situ polymerization of a polydopamine (PDA) adhesive, which is similar to the bonding of marine mussels in nature (Figure 5.2).[33] The in-situ polymerization of the PDA adhesive is irreversible and penetrates into the upper surface of commercial soft contact lenses to form a permanent interaction, which is crucial to ensuring the mechanical durability of the SSCL for long-term routine use.

The underlying working principle of the ocular tonometer is as follows. A rise in IOP causes an increase in the curvature radius of an eye (i.e., approximately 3 μm $mmHg^{-1}$) by which the ocular tonometer is stretched and compressed in the radial and axial (i.e., thickness) directions, respectively.[11] The geometric deformation of the ocular tonometer causes an increase of inductance and capacitance in the RLC resonant circuit, which leads to a detectable decrease in resonance frequency[34]:

$$f^{-1} = 2\Pi\sqrt{LC}$$

Figure 5.3b presents the data acquisition scheme in which the ocular tonometer is inductively coupled to a reader coil in a proximity of less than 10 mm. The reader coil can be embedded within a typical eyeglass frame or sleep eye mask for daytime and nighttime IOP monitoring, respectively. During IOP measurements, the reader coil is wired to a portable vector network analyzer (VNA) that enables the constant acquisition of reflection coefficient (S11) spectrum. Figure 1c provides a photograph of the ocular tonometer built on a commercial soft contact lens (Air Optix Night & Day Aqua; Alcon, Inc.). The ocular tonometer was thin (i.e., 50 μm thick), narrow (i.e., 200 μm wide), and configured into a serpentine (i.e., stretchable) ring shape on the peripheral area and outside surface of the soft contact lens. The inner diameter of the ocular tonometer (i.e., 13 mm) was substantially larger than typical pupil diameter in adults (i.e., 2−8 mm) to assure clear central and peripheral vision in all directions for wearers. Figure 1d presents the cross-sectional scanning electron microscopy (SEM) view of the ocular tonometer. The AgSEBS layers were clearly separated by the Silbione layer, all of which were entirely encapsulated by the PDMS layer. In addition, the PDMS layer exhibited gradually tapered ends at an angle of 10−15° to reduce edge irritation when contact with the inner eyelid (Figure 5.4a). The resulting SSCL was fitted well to an enucleated pig eye that provides an anatomical similarity to the human eye in size and shape (Figure 5.3e).[35] The SSCL formed a highly intimate and seamless interface along the corneal anterior surface of the pig eye by virtue of the

ergonomic design of its bare soft contact lens. This aspect is crucially important to maintain the measurement accuracy and repeatability of the SSCL particularly under ambulatory conditions. Various commercial brands of soft contact lenses were applicable without noticeable difference in overall quality (Figure 5.4b), which have been proven safe for those even with chronic ocular diseases, including glaucoma, or following incisional surgeries.[24] For all cases, the gas permeability of the SSCL remained similar to their bare soft contact lenses (Figure 5.4c).

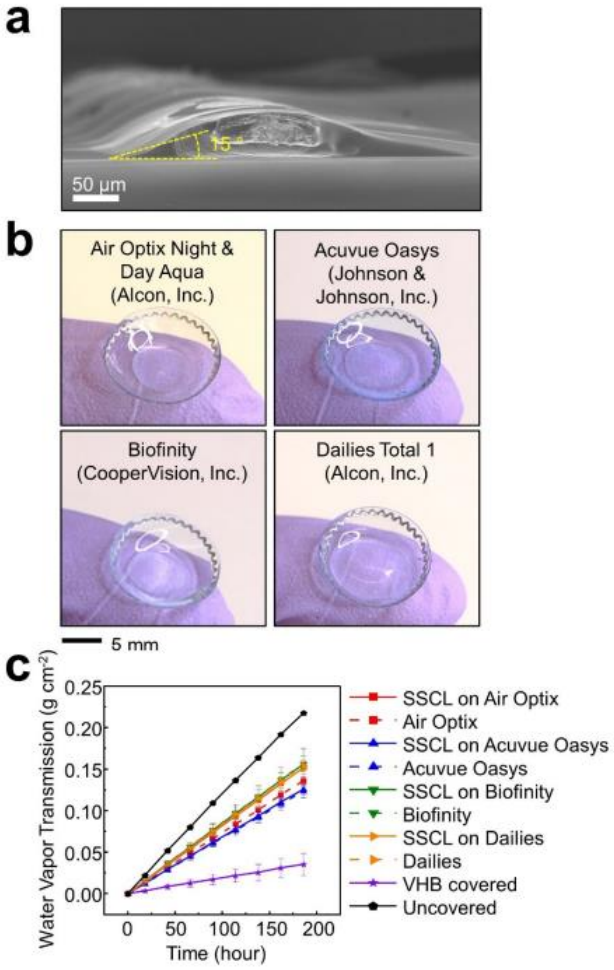

Figure 5.4. Representative cross-sectional SEM image of the internal ocular tonometer. b, Photographs of the SSCL built upon various commercial brands of soft contact lenses. c, Water vaper transmission of the SSCL upon various commercial brands of soft contact lenses as compared to their bare soft contact lenses (n = 3).

5.4.2 Benchtop Evaluations

The SSCL (E = 1.34 ± 0.35 MPa) was as soft as its bare soft contact lens (E = 1.37 ± 0.27 MPa) mainly due to the substantial softness of the internal ocular tonometer (E = 0.08 ± 0.01

MPa) (Figure 5.5a). The SSCL was also stretchable in which the internal ocular tonometer remained intact without mechanical failure under stretching up to > 100 % even after its bare soft contact lens was torn apart at the applied strain of ~90% (Figure 5.6). Figure 5.5b presents that the relative resistance change (ΔR/R0) of the SSCL remained less than 10% and 30% after 10,000 cycles of stretching at 25% and 50%, respectively. Figure 5.5c shows the capacitance response of the SSCL under pressure in a range of 0−40 mmHg, which reflects the typical IOP range of human eyes under normal (i.e., 10−21 mmHg) and hypertension (i.e., 21−40 mmHg) conditions.[36] For comparison, different types of dielectric interlayers, including the Silbione (E ≈ 5 kPa), Ecoflex (E ≈ 30 kPa), and PDMS (E ≈ 640 kPa), were employed in the ocular tonometer. As expected, the use of the softest dielectric interlayer (i.e., Silbione) led to the highest capacitive sensitivity (i.e., 6.8 × 10-4 $mmHg^{-1}$) over others. Details of calculating the capacitive sensitivity are described in the Materials and Methods section.

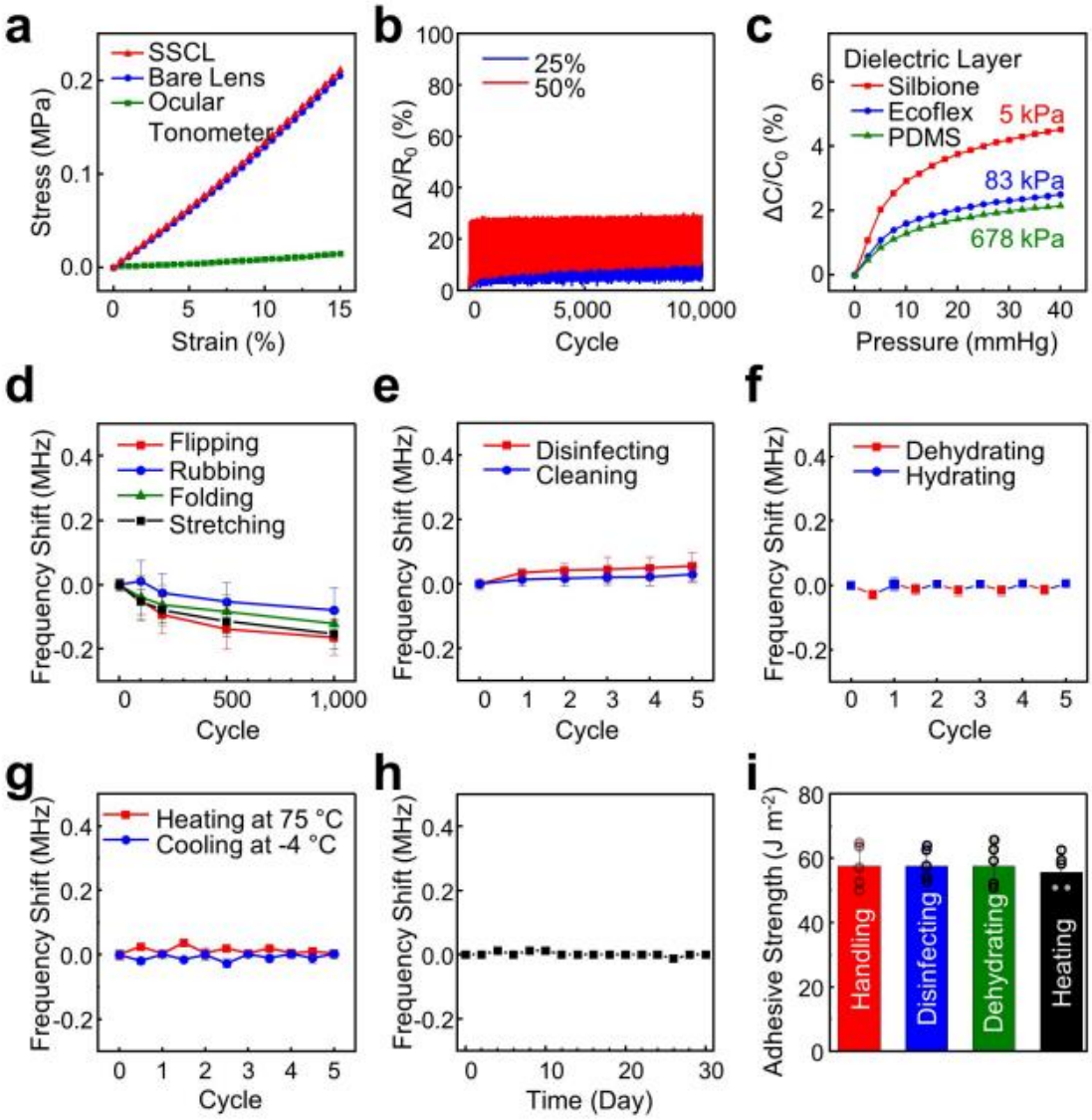

Figure 5.5. Benchtop evaluations. (a) Stress–strain curve for the SSCL (red line), the bare soft contact lens without the ocular tonometer (blue line), and the ocular tonometer without the soft contact lens (green line). (b) Resistance response ($\Delta R/R_0$) of the SSCL following 10,000 cycles of stretching at 25% (blue line) and 50% (red line). (c) Capacitance response ($\Delta C/C_0$) of the SSCL with respect to applied pressure by employing three different dielectric interlayers made of Silbione (red line), Ecoflex (blue line), and PDMS (green line) in the ocular tonometer. (d) Normalized baseline resonant frequency of the SSCL following 1,000 cycles of flipping, rubbing, folding, and stretching; € 5 cycles of disinfecting (red line) and cleaning (blue line); (f) 5 cycles of hydrating (red line) and dehydrating (blue line); (g) 5 cycles of heating and cooling; and (h) soaking in a saline solution for 30 days. (i) Adhesive strength of the PDA layer after multiple cycles of handling, disinfecting, dehydrating, and heating. The error bars represent standard deviations with $n = 5$ for each group.

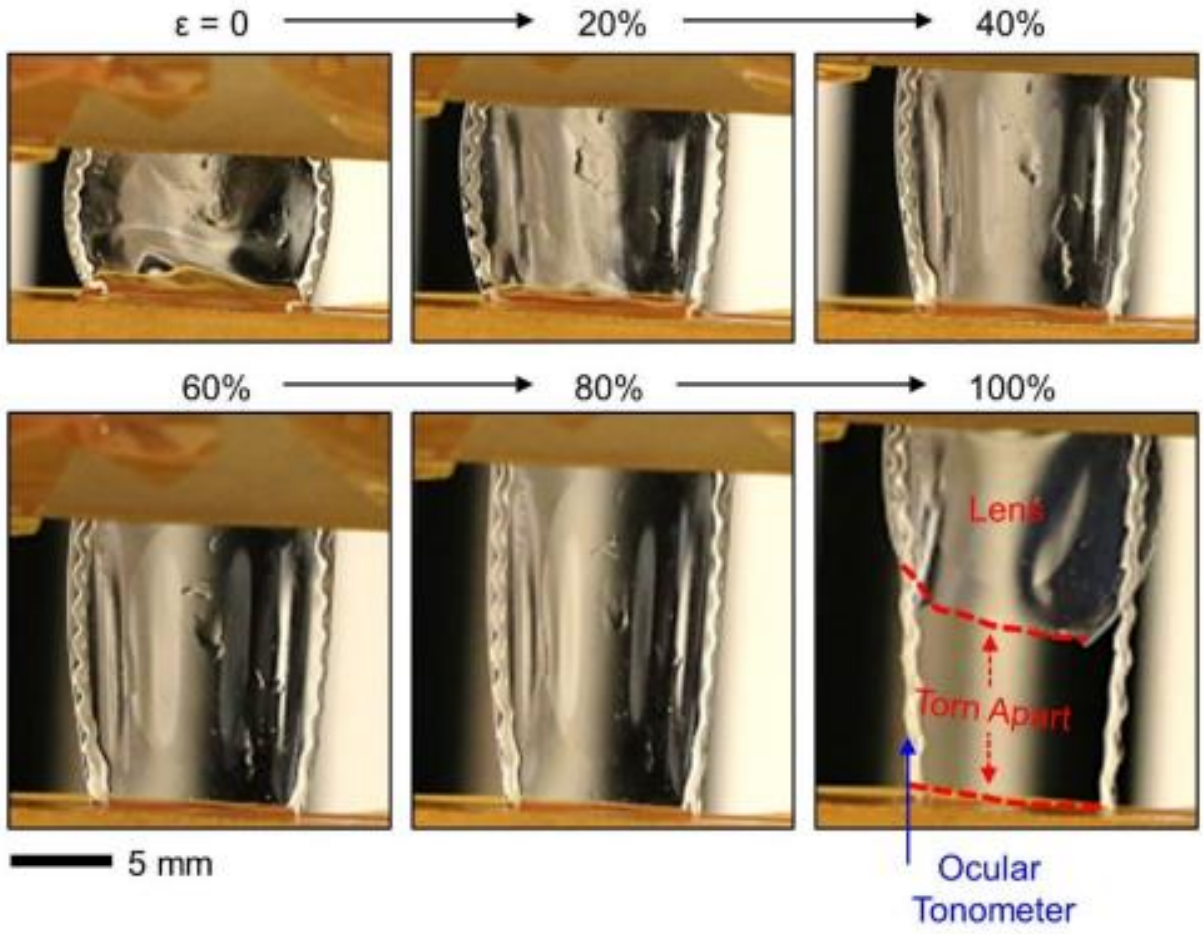

Figure 5.6. Photographs of the SSCLs under stretching up to 100%

The mechanical, electrical, and chemical reliability of the SSCL is an essential consideration for its long-term use against daily lens cleaning, disinfecting, storing, handling, and misuse conditions (e.g., dehydrating and overheating). The SSCL satisfies all these needs. Specifically, the resonant frequency of the SSCL changed barely, or slightly within only ±0.2 MHz, from its baseline following multiple cycles of mechanical deformations such as flipping, rubbing, folding, and stretching (Figure 5.5d); cleaning and disinfecting with commercial solutions (Renu; Bausch & Lomb, Inc. & Clear Care; Alcon Laboratories, Inc.) (Figure 5.5e); 2-hour dehydrating in ambient condition and 20-minute rehydrating in a cleaning saline solution (Renu; Bausch & Lomb, Inc.) (Figure 5.5f); 30-minute significant overheating at 75 °C and 30-minute cooling to -4 °C (Figure 5.5g); and 30-day storing in a saline solution (Renu; Bausch & Lomb, Inc.) (Figure 5.5h). A total of 5 measurements were taken and averaged at each data point with the error bars denoting standard deviations. Importantly, the adhesive strength of the PDA

layer (i.e., 57.55 ± 11.72 J m-2) was also maintained against all these conditions without any notable sign of delamination (Figure 5.5i).

5.4.3 *Ex Vivo* Evaluations in Enucleated Pig Eyes

The wireless sensing performance of the SSCL was evaluated ex vivo in enucleated pig eyes (n = 3). Figure 5.7a schematically illustrates the ex vivo measurement setup that includes two needles to cannulate an enucleated pig eye. The first needle was connected to a syringe pump to modulate the IOP of an enucleated pig eye by infusing and removing saline solution to/from the anterior chamber of the pig eye. The second needle was connected to a pressure gauge (V6402; Smiths Medical, Inc.) to simultaneously measure the IOP for calibration. The SSCL was fitted to the corneal surface of the pig eye and then inductively coupled to a reader coil in a proximity of less than 10 mm (Figure 5.7b). The reader coil was comprised of a wound, enamel-covered copper coil with an outer and inner diameter of 25 and 20 mm, respectively. The resistance and inductance of the reader coil were tuned at 3.5−4.0 Ω and 450−480 μH, respectively. The overall dimension and design of the reader coil were adjusted for optimal impedance matching with the SSCL. During IOP monitoring, the reader coil was wired to a portable VNA (FieldFox Handheld Analyzer 9913A; Keysight Technologies, Inc.; 292 × 188 × 72 mm). A total of 6 measurements were taken and averaged at each data point while the IOP of the pig eye was increased and decreased between 6 and 38 mmHg at an interval of 4 mmHg by infusing and removing saline solution, respectively.

Figure 5.7c presents that the reflection spectra (S11) of the SSCL were clearly shifted in response to ascending and descending IOP of the pig eye with negligible hysteresis. Figure 3d shows the resonant frequency of the SSCL for a total of 3 enucleated pig eyes with different dioptric corneal curvatures (i.e., 38.75, 38.37, and 39.37 D) and thicknesses (i.e., 948, 1,084, and 1,004 μm). Irrespective of the corneal curvature and thickness, an empirical linear fit was obtained for each pig eye with the corresponding responsivity and sensitivity of approximately 0.030 MHz $mmHg^{-1}$ (R2 = 0.98) and 125 ppm $mmHg^{-1}$, respectively. The high measurement accuracy and repeatability of the SSCL were mainly attributed to its seamless and reliable fit to the various corneal curvatures and thicknesses of the pig eyes. For comparison, the results of control experiments with an enucleated cow eye (typical corneal curvature ≥ 26 D) that is dissimilar to the human eye (typical corneal curvature ≥ 40 D) in corneal curvature are

summarized in Figure 5.8a-d. The measurement responsivity of the SSCL was considerably deteriorated due to the geometric discrepancy (i.e., interfacial gap) between the SSCL and the cow eye. Figure 5.7e and f show the effect of the angle (θ) and distance (d) between the SSCL and the reader coil on signal quality. The corresponding reflection spectra are shown in Figure 5.8e and f. No shift in the baseline resonant frequency of the SSCL appeared at $\theta \leq 50°$ and $d \leq$ 10 mm, indicating that the extent of possible user misalignments or displacements can be accommodated without significant degradation in signal quality. The overall performance of the SSCL was also maintained when the reader coil was embedded within an eyeglass frame or a sleep eye mask.

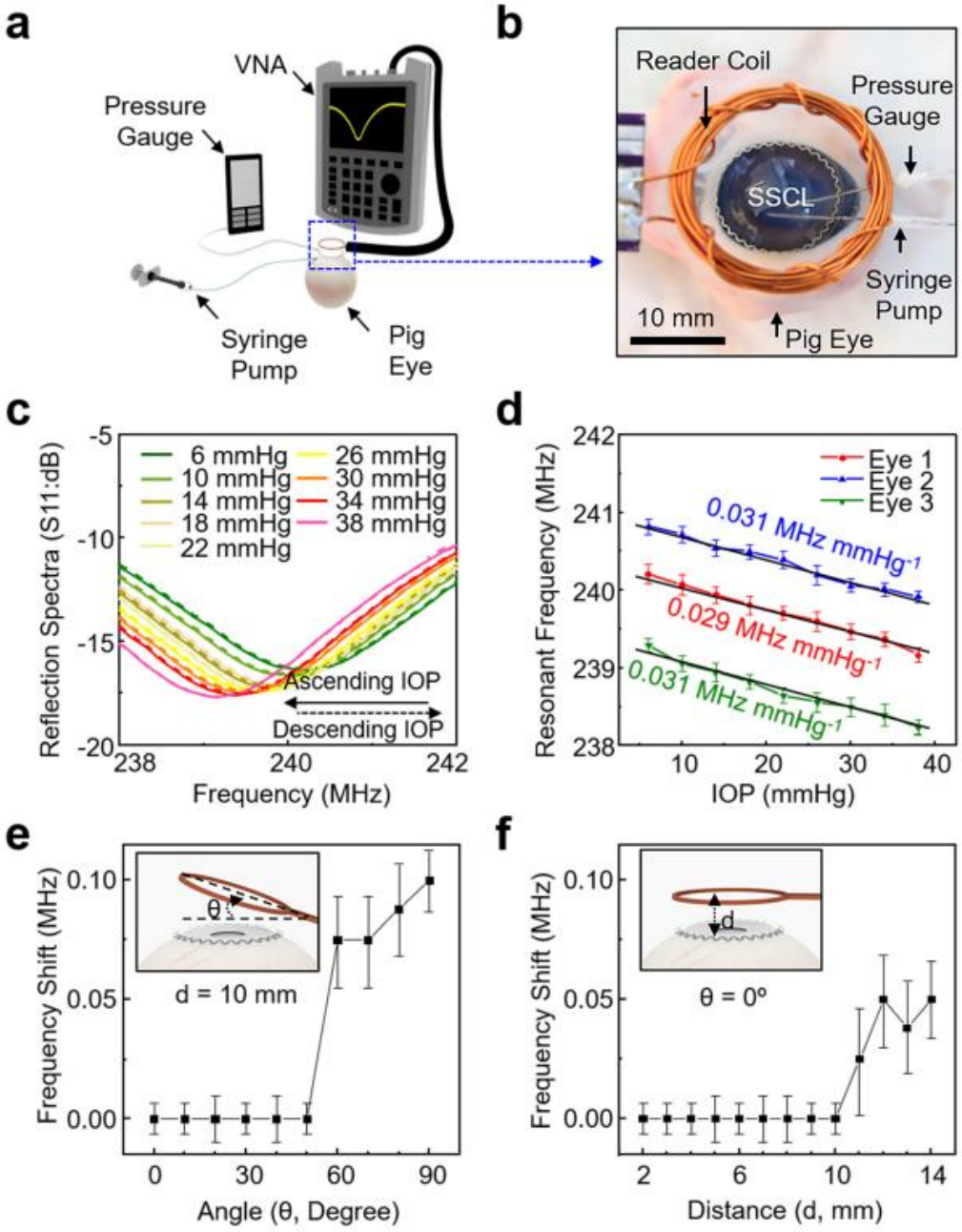

Figure 5.7. *Ex vivo* evaluations in enucleated pig eyes. (a) Schematic view of the ex vivo measurement setup. (b) Photograph of the SSCL in an enucleated pig eye during measurement. (c) Reflection spectra (S11) of the SSCL in response to ascending and descending IOP of the pig eye. (d) Resonant frequency of the SSCL in the response to the IOP of enucleated pig eyes (n = 3). (e) Baseline resonant frequency of the SSCL at various angles with respect to the reader coil (n = 5). (f) Baseline resonant frequency of the SSCL at various distances with respect to the reader coil (n = 5).

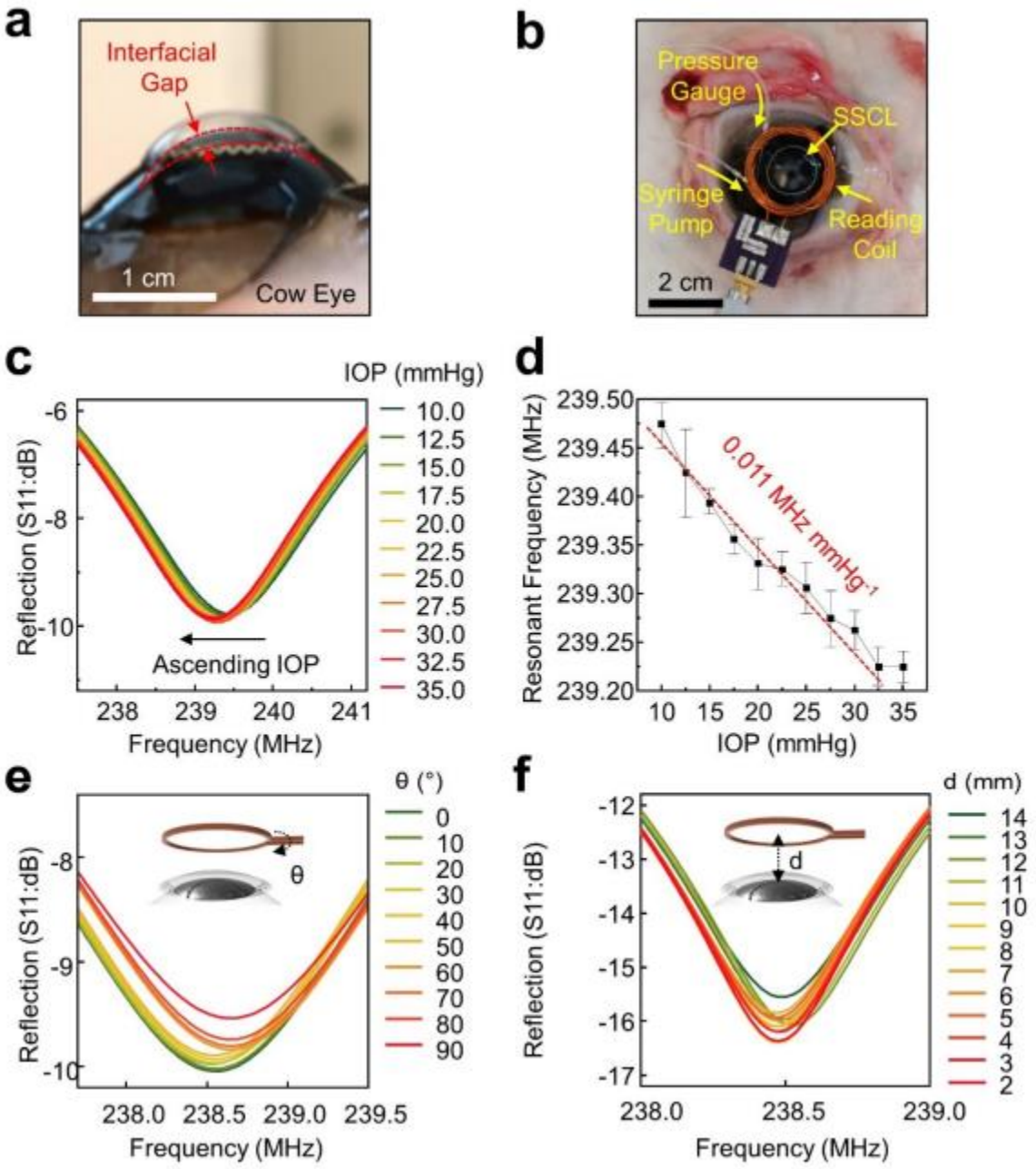

Figure 5.8. (a) Photograph of the SSCL in an enucleated cow eye. (b) Photograph of the SSCL during IOP monitoring. (c) Reflection spectra (S11) of the SSCL in response to ascending IOP of the cow eye. (d) Resonant frequency of the SSCL in response to the IOP of the cow eye (n = 3). (e) Reflection spectra (S11) of the SSCL at various angles with respect to a reader coil. (f) Reflection spectra (S11) of the SSCL at various distances with respect to a reader coil.

5.4.4 Cell Viability and *In Vivo* Evaluations in Rabbit Eyes

The time-dependent cell viability of the SSCL to human corneal cell lines was assessed to identify any adverse response at the cellular level. Specifically, human corneal epithelial cells (HCEpiCs) were cultured in a medium (EpiGRO™ Human Ocular Epithelia Complete Media; MilliporeSigma, Inc.) at 37.5 °C for 72 hours. The cells were seeded on the surface of the SSCL and measured using a MTT (3-(4,5-dimethylthiazol-2-yl)-2,5-diphenyltetrazolium bromide) assay kit (Sigma-Aldrich, Inc.). Details of the cell viability assay are described in the Materials and Methods section. Figure 5.9a shows the experimental results obtained from the SSCL without (blue bars) and with (green bars) the presence of the PDA adhesive as compared to its bare soft contact lens (red bars). The cell viability remained above 95% throughout the assay period without notable differences among the groups (n = 5 for each group). In turn, the SSCL poses little risk of developing corneal inflammation.

The biofouling resistance (i.e., protein accumulation from tear fluid) of the SSCL was also assessed, which is associated with ocular surface inflammatory complications such as giant papillary conjunctivitis.[37] Specifically, proteins were incubated on the SSCL using a 5 mg mL^{-1} of bovine serum albumin-fluorescein conjugate (BSA-FITC A23015; Fisher Scientific, Inc.) in a phosphate buffered saline (PBS; pH 7.4) for 2 hours at 37.5 ºC, and then, the accumulation of proteins was quantified over time via fluorescence imaging. Figure 5.9b presents that the accumulation of proteins over the top surface of the internal ocular tonometer of the SSCL remained lower compared to its bare soft contact lens with $^{**}p < 0.01$ according to a one-way analysis of variance (ANOVA) method with the Tukey's post hoc test. The lower accumulation of proteins over the internal ocular tonometer of the SSCL is likely attributed to the presence of its hydrophobic encapsulation layer (i.e., PDMS). Importantly, the accumulated proteins were cleanly removed after a disinfecting cycle with a commercial solution (Clear Care; Alcon Laboratories, Inc.) for both groups (Figure 5.9c).

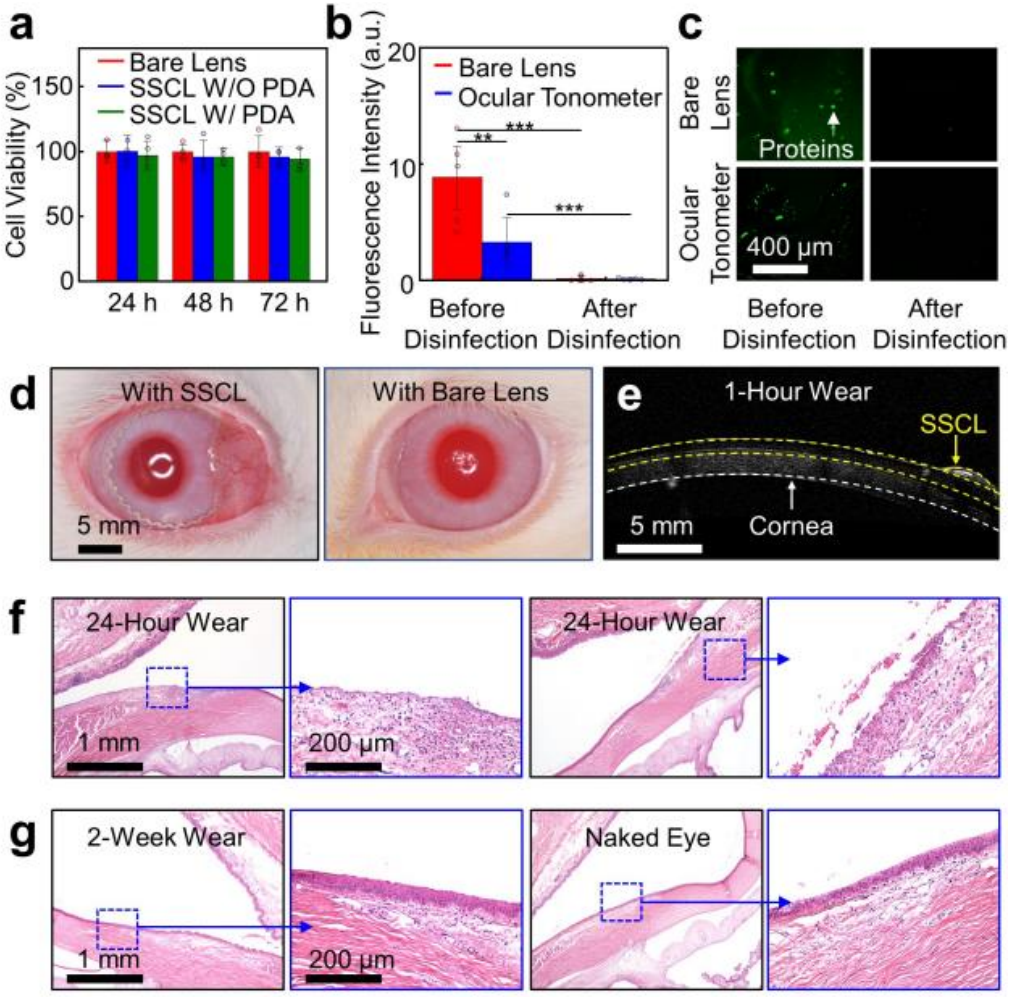

Figure 5.9. Cell viability and *in vivo* evaluations in rabbit eyes. (a) Cell viability assay of HCEpiCs seeded on the SSCL without (blue bars) and with (green bars) the presence of the PDA adhesive as compared to the bare soft contact lens (red bars) (n = 4). (b) Quantified accumulation of proteins on the bare soft contact lens (red bar) and the SSCL (blue bar) before (left column, p = 0.02194 for before disinfection Bare Lens vs. Before disinfection Tonometer, n = 5; p = 0.00115 for before disinfection Bare Lens vs. after disinfection Bare Lens, n = 5) and after (right column, p = 0.00979 for before disinfection Tonometer vs. after disinfection Tonometer, n = 5) disinfection. Significance was set at $^{***}p < 0.01$, and $^{**}p < 0.1$. (c) Representative surface fluorescence image of the bare soft contact lens (top row) and the SSCL (bottom row) before (left column) and after (right column) disinfection. (d) Photographs of the rabbit eye wearing the SSCL (left panel) and the bare soft contact lens (right panel). (e) Representative AS-OCT image of the rabbit eye after 1 hour of wearing the SSCL. (f) Representative photomicrographs of the rabbit eye with H&E staining displaying epithelial erosion and mild mixed inflammation with edema at the limbus after 24-hour wear of the SSCL (left panel) and the bare soft contact lens (right panel). (g) Representative photomicrographs of the rabbit eye with H&E staining displaying no abnormality at the limbus after 2-week wear of the SSCL (left panel) as compare to those of the naked eye (right panel).

The in vivo tissue compatibility and long-term wearability of the SSCL were assessed in rabbit eyes (n = 4) after fitting the SSCL on an eye for 24 hours as compared to its bare soft contact lens on the contralateral eye (Figure 5.9d). The rabbit eye provides an anatomical similarity to the human eye in shape and size.[35] The eyelids were partially sutured (i.e., partial temporary tarsorrhaphy) to improve the lens retention at the corneal surface. Details of the experiments in rabbit eyes are described in the Materials and Methods section. Figure 5.9e provides a representative anterior segment ocular coherence tomography (AS-OCT) image of a rabbit eye after 1 hour of wearing the SSCL, which confirmed its conformational alignment with the cornea. No notable abnormality was observed in 2 out of total 4 rabbits while mild hyperemia (grade 1; modified McDonald-Schadduk system) was noted in the palpebral conjunctiva of the other 2 rabbits without notable differences between the left and right eyes (Figure 5.10a). In addition, no notable abnormality was observed after routine wear of the SSCL for 8 hours a day for up to 2 weeks in rabbit eyes (n = 2), without suturing the eyelids, as compared to the naked eyes (Figure 5.10b).

Figure 5.9f shows the corresponding histopathology images of rabbit eyes after 24 hours of wearing the SSCL on an eye (left panel) and its bare soft contact lens on the contralateral eye (right panel). The rabbit eyes in both groups exhibited minimal to mild lesions (grade 1 to 2) including erosion of the conjunctival epithelium over the limbus with some edema and heterophilic or mixed inflammation. No notable differences were observed between the groups. Only minimal accumulation of heterophils and lymphocytes appeared in the palpebral conjunctiva. In addition, the rabbit eyes after the 2-week routine wear of the SSCL exhibited no or minimal lymphocytic inflammation (grade 1) in the palpebral conjunctiva without notable difference compared to the naked eyes (Figure 5.9g). The minimal inflammation might be background lesions or caused by the partial suture (i.e., partial temporary tarsorrhaphy) which is unassociated with wearing the SSCL. The quantitative assessments of histopathologic inflammation grades in the rabbit cornea and conjunctiva are summarized in Table 5.1.

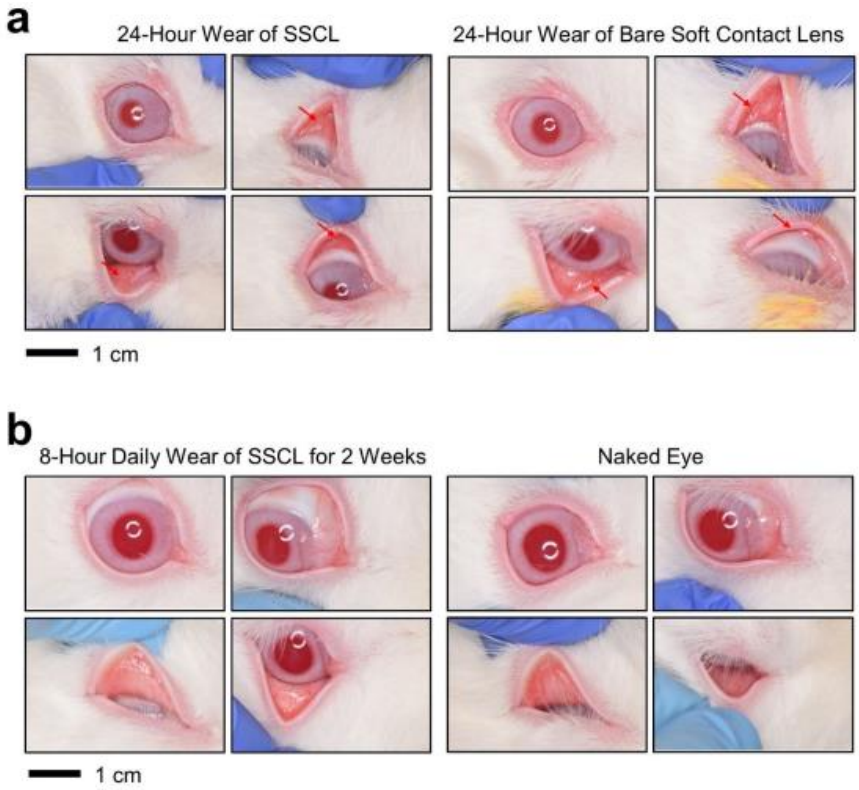

Figure 5.10. (a) Photographs of rabbit eyes after 24-hour wear of the SSCL (left panel) and its bare soft contact lens (right panel). The red arrows indicate the minimal to mild hyperemia of the palpebral conjunctiva. (b) Photographs of rabbit eyes after 8-hour daily wear of the SSCL for 2 weeks (left panel) as compared to the naked eye (right panel). No abnormality was observed.

Table 5.1. Quantitative assessment of histopathologic inflammation grades of the rabbit cornea and conjunctiva

Group I: 24-Hour Continuous Wear		
Animal ID	Right Eye- SSCL*	Left Eye - Bare Lens Control
1	1	2
2	2	1
3	2	2
4	2	1
Group II: 2-Week Wear (8 Hours/Day)		
	Right Eye- SSCL	Left Eye - Untreated Control
5	0	1
6	1	1

*Grades for assessment of inflammation: 0 – None, 1 – Minimal, 2 – Mild, 3 – Moderate, 4 - Severe

5.4.5 *In Vivo* Evaluations in Dog Eyes

The in vivo 24-hour sensing performance of the SSCL was assessed in a dog eye (female beagle; 10 months old) under ambulatory conditions using a dog goggle (V2 Goggle; Rex Specs, Inc.) with a reader coil embedded (Figure 5.11a). The dog eye provides an anatomical similarity to the human eye in shape and size.[36] For calibration, the IOP of the dog eye was also measured with a commercial ocular tonometer (iCare Tonovet Plus; iCare, Inc.) at an interval of 2 hours by applying a drop of an IOP-lowering medication (0.005% Latanoprost; Bausch & Lomb, Inc.) following the first measurement. Figure 5.11b shows the average resonant frequency of the SSCL with respect to the IOP of the dog from a total of 6 measurements at each time interval. An empirical linear fit (i.e., resonant frequency = −0.16 × IOP + 244.11) was obtained with the corresponding responsivity and sensitivity of 0.16 MHz $mmHg^{-1}$ (R2 = 0.88) and 662 ppm $mmHg^{-1}$, respectively. Notably, the responsivity and sensitivity of the SSCL in the dog eye is higher than those in the enucleated pig eyes (Figure 5.7d) mainly due to their fitting quality affected by different corneal rigidity and irregularity of the eyes or the ex vivo setting with the insertion of cannulation needles.[38] The standard measurement errors in the dog eye remained larger than those in the enucleated pig eye due to the continued blinking and eye movements of the dog under ambulatory conditions.

Figure 5.11c presents the calibrated absolute IOP values of the dog eye wearing the SSCL for 24 hours (from 9 am to 9 am on the next day) compared to control measurements using the iCare Tonovet Plus on the same eye in an interval of 20 minutes. The SSCL enabled the continuous 24-hour monitoring of absolute IOP values in the dog eye under ambulatory conditions while the iCare Tonovet Plus required the dog to remain still with its eyes open during the measurements. The measurements with the SSCL exhibited a typical IOP rhythm of the dog eye throughout the day in which its overall trends agreed well with those associated with the iCare Tonovet Plus. No notable degradation in signal quality with the SSCL occurred irrespective of blinking or eye movements of the dog. The outliers of the IOP measurements (e.g. from 9 am to 12 pm) using the iCare Tonovet Plus were mainly attributed to motion artifacts by the excitement of the dog.

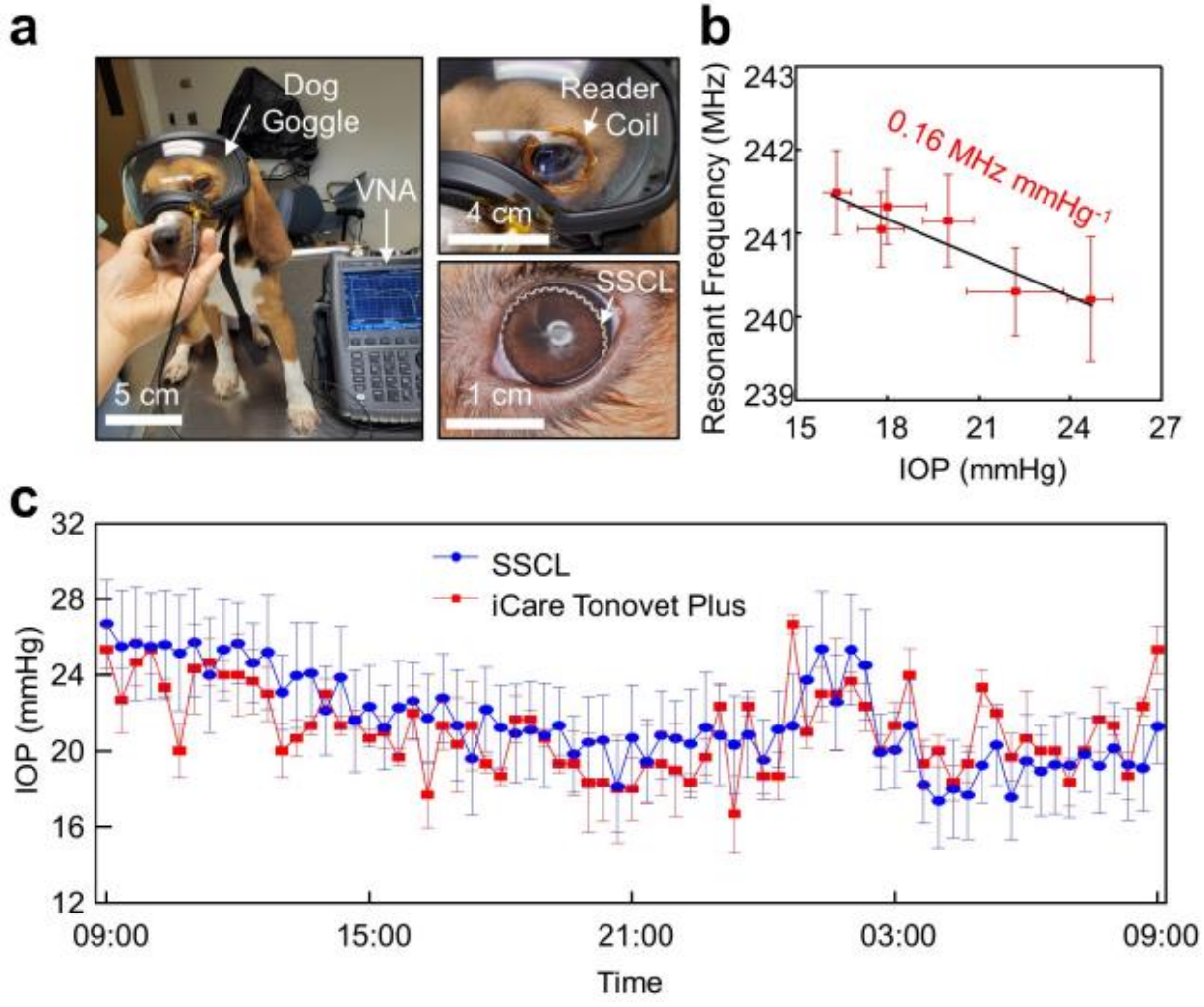

Figure 5.11. *In vivo* sensing performance in dog eyes. (a) Photographs of a dog wearing the SSCL and a dog goggle (V2 Goggle; Rex Specs, Inc.) embedded with the reader coil. (b) Resonant frequency of the SSCL with respect to the IOP values of the dog (n = 3). (c) 24-hour IOP rhythm of the dog obtained from the SSCL (blue line) and the iCare Tonovet Plus (red line) (n = 3).

5.4.6 In-clinic Evaluations in Human Eyes

The user comfort, ease-of-use, lens fit, and visual field of the SSCL were examined in human eyes. A total of 3 adults (> 18 years old) who had worn contact lenses currently or previously were included in this study. Participants were tested following consent and study institutional review board approval. Prior to, during, and following each wear, the ocular health and lens fit of each participant were examined by visual acuity, participant-reported comfort rating, AS-OCT, and slit lamp biomicroscopic measurements. All participants were asked to

attend an initial in-clinic qualification visit to establish baseline measures and an initial fit of the SSCL. The lens fit, visual acuity, and user comfort rating of the SSCL were compared with wearing its bare soft contact lens or the Triggerfish lens on the contralateral eye.

Figure 5.12a shows the photographic (left panel) and slit lamp biomicroscopic (right panel) images of the SSCL in a participant. The SSCL was fitted well on the eye with good centration and coverage as similar as its bare soft contact lens. The internal ocular tonometer of the SSCL was positioned on the outer peripheral edge of the iris to be visually inconspicuous, and where the maximum strain occurred under any change of IOP.[39] The SSCL remained centered on the cornea, similar to its bare soft contact lens, during normal blinking and eye movements in all directions of gaze. The displacement of the SSCL on the eye was quantitatively comparable to that of its bare soft contact lens (Figure 5.13). Figure 5.12b provides a representative AS-OCT image of the eye after 1 hour of wearing the SSCL, confirming its conformational alignment with the cornea. As expected, the visual field of the eye wearing the SSCL remained unchanged as compared to the naked eye due to the substantially larger inner diameter of the internal ocular tonometer than the pupil diameter (Figure 5.12c).

Figure 5.12d shows the slit lamp biomicroscopic images of the eye after 6 hours of wearing the SSCL (top panel) as compared to the naked eye (bottom panel) by applying a drop (~1 mg) of sodium fluorescein (Fluorets ophthalmic strips; Bausch & Lomb, Inc.). No signs of corneal damage were observed following wear of the SSCL. Clinically insignificant superficial punctate corneal staining was noted in the corneal epithelial surface at a level that is commonly observed with all contact lens use.[40] The staining typically resolved within 1 hour following removal of the SSCL. The bulbar and limbal conjunctiva of the eye exhibited only mild hyperemia (clinician grade ≤ 0.5) after > 6 hours of wearing the SSCL, which mirrored the response following wear of its bare soft contact lens. No other complications were noted.

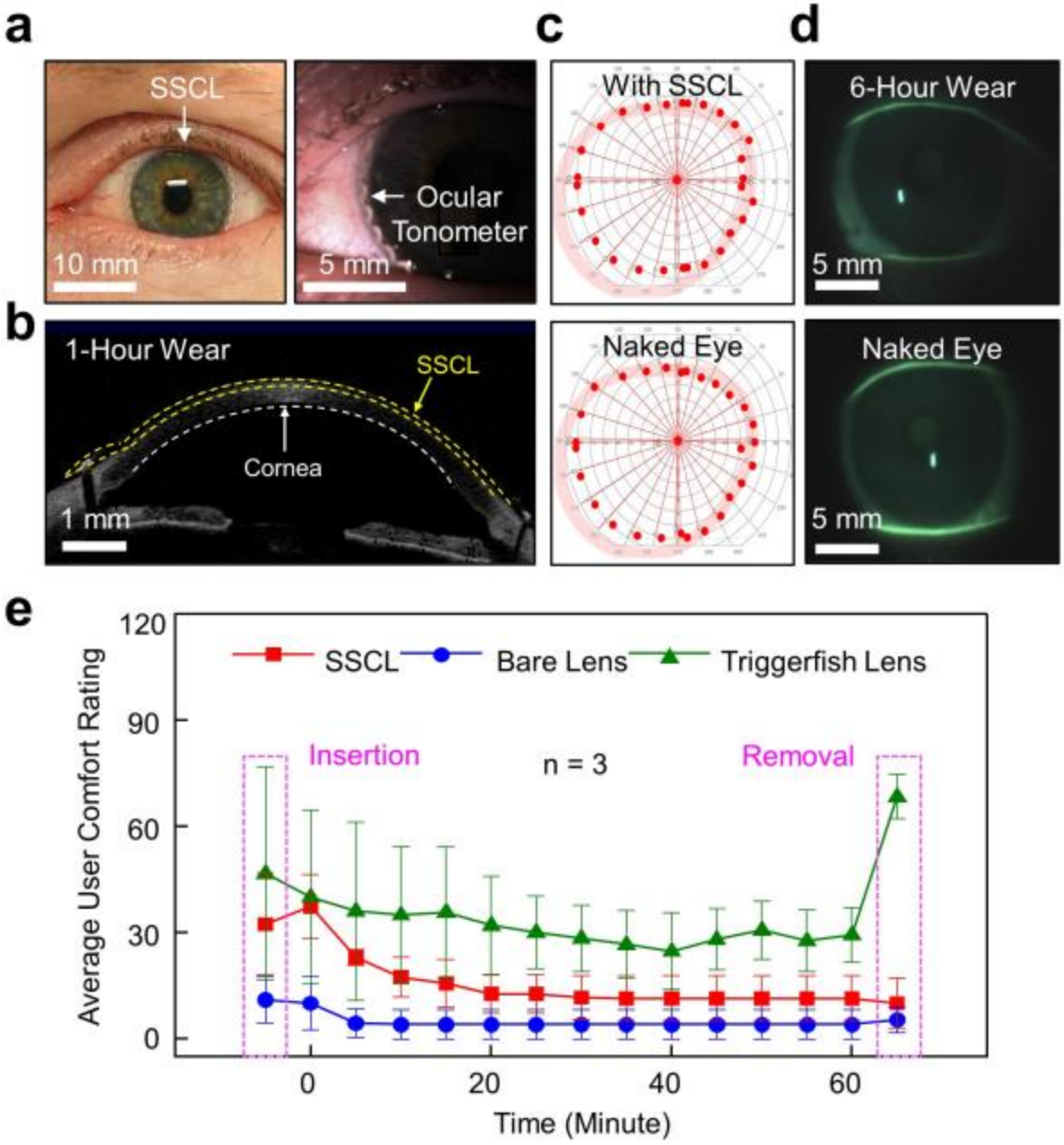

Figure 5.12. In-clinic examinations in human eyes. (a) Photograph (left panel) and slit lamp biomicroscopic image (right panel) of a human eye wearing the SSCL. (b) Representative AS-OCT image of the eye after 1 hour of wearing the SSCL. (c) Representative visual field of the eye wearing the SSCL (top panel) and the naked eye (bottom panel). (d) Representative slit lamp fluorescent images of the eye after 6 hours of wearing the SSCL (top panel) and the naked eye (bottom panel). € Average user comfort rating for the SSCL (red line), the bare soft contact lens (blue line), and the Triggerfish lens (green line) from a total of 3 participants.

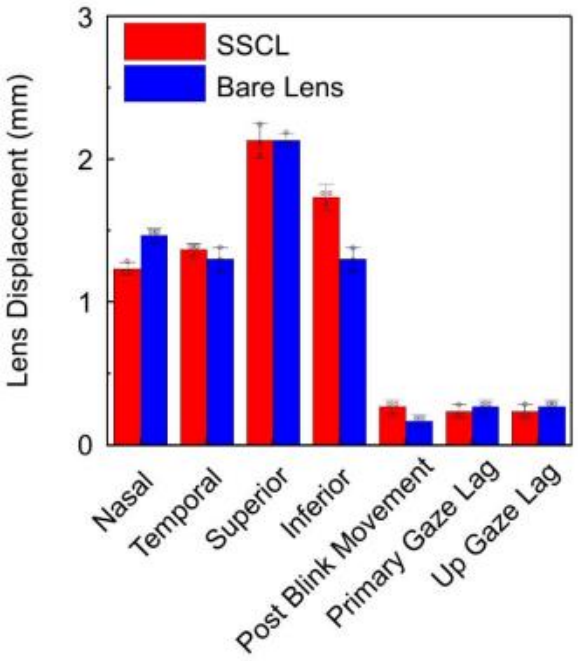

Figure 5.13. Displacement of the SSCL on a human eye compared to its bare soft contact lens (n =3).

For the quantitative assessment of comfort level, each participant was asked to complete a survey during and following wear of the SSCL, its bare contact lens, and the Triggerfish lens using a simple 100-point numeric scale, where a rating of "100" represented extremely uncomfortable/intolerable and a rating of "1" perfectly comfortable/unnoticeable at all, in a similar manner as previously used in many clinical studies with wearing contact lenses.[41] Figure 5.12e shows the average user comfort rating following insertion, during wear, and following removal of the SSCL, its bare soft contact lens, and the Triggerfish lens at a time interval of 5 minutes for total 60 minutes. All the participants were able to obtain an adequate lens fit with wearing the SSCL and settled into a satisfying comfort level. Specifically, the participants reported unnoticeable adaptation of the SSCL (i.e., average rating = 12.7 ± 5.4) within approximately 20 minutes of wear, which was slightly higher comparing to the control bare contact lens (i.e., average rating = 4.0 ± 4.2). On the other hand, the participants reported severe discomfort during insertion (i.e., average rating = 46.7 ± 30.1) and removal (i.e., average rating = 68.3 ± 6.2) of the Triggerfish lens without noticeable stabilization over time (i.e., average rating = 24.7 ± 10.9−68.3 ± 6.2).

5.4.7 Ambulatory IOP Monitoring in Human Eyes

The ambulatory IOP of the participants under postural changes was monitored in real time with the SSCL as compared to control measurements with both the iCare Home and the Triggerfish lens at time-matched points. Figure 5.14a and b show representative photographs of a participant in sitting and supine postures during IOP monitoring with the reader coil embedded within an eyeglass frame and a sleep eye mask, respectively. The SSCL was able to capture the dynamic change of the IOP in response to various body postures including sitting, standing, supine, right lateral, left lateral, and prone (Figure 5.14c). For calibration, the IOP of the same eye was also monitored with the iCare Home in a sequential manner immediately before each measurement with the SSCL. A total of 6 measurements were acquired in each body posture. The calibration took place only once at the initial use without iterative calibrations. The entire measurement sequence using both the SSCL and the iCare Home were completed within 1 hour for each participant to minimize unwanted nyctohemeral variation in IOP. Figure 5.14d shows the resonant frequency of the SSCL in each body posture for the participants with different corneal curvatures (i.e., 46.2, 45.4, and 40.9 D) and thicknesses (i.e., 542, 588, and 595 μm). Participants 1 & 2 exhibited normal IOP values (i.e., 13−21 mmHg) while participant 3 exhibited mild ocular hypertension (i.e., 22−26 mmHg), which were also confirmed by the GAT. An empirical linear fit (i.e., IOP = −3.6 × resonant frequency + 890) was consistently obtained by virtue of the seamless and reliable fit of the SSCL irrespective of corneal curvature and thickness. The corresponding responsivity and sensitivity of the SSCL were 0.27 MHz mmHg-1 (R2 = 0.91) and 1,121 ppm mmHg-1, respectively. It was noted that the sensitivity of the SSCL remained substantially (i.e., by 9-fold) higher relative to those in the enucleated pig eye (Figure 5.7d) mainly due to the improved fit of the SSCL to the human eye. Notably, the sensitivity of the SSCL also remained at least 2-fold higher than that (< 500 ppm mmHg-1) of current state-of-the-art wearable ocular tonometers that were tailored for human eyes (Table 5.2).[42–46]

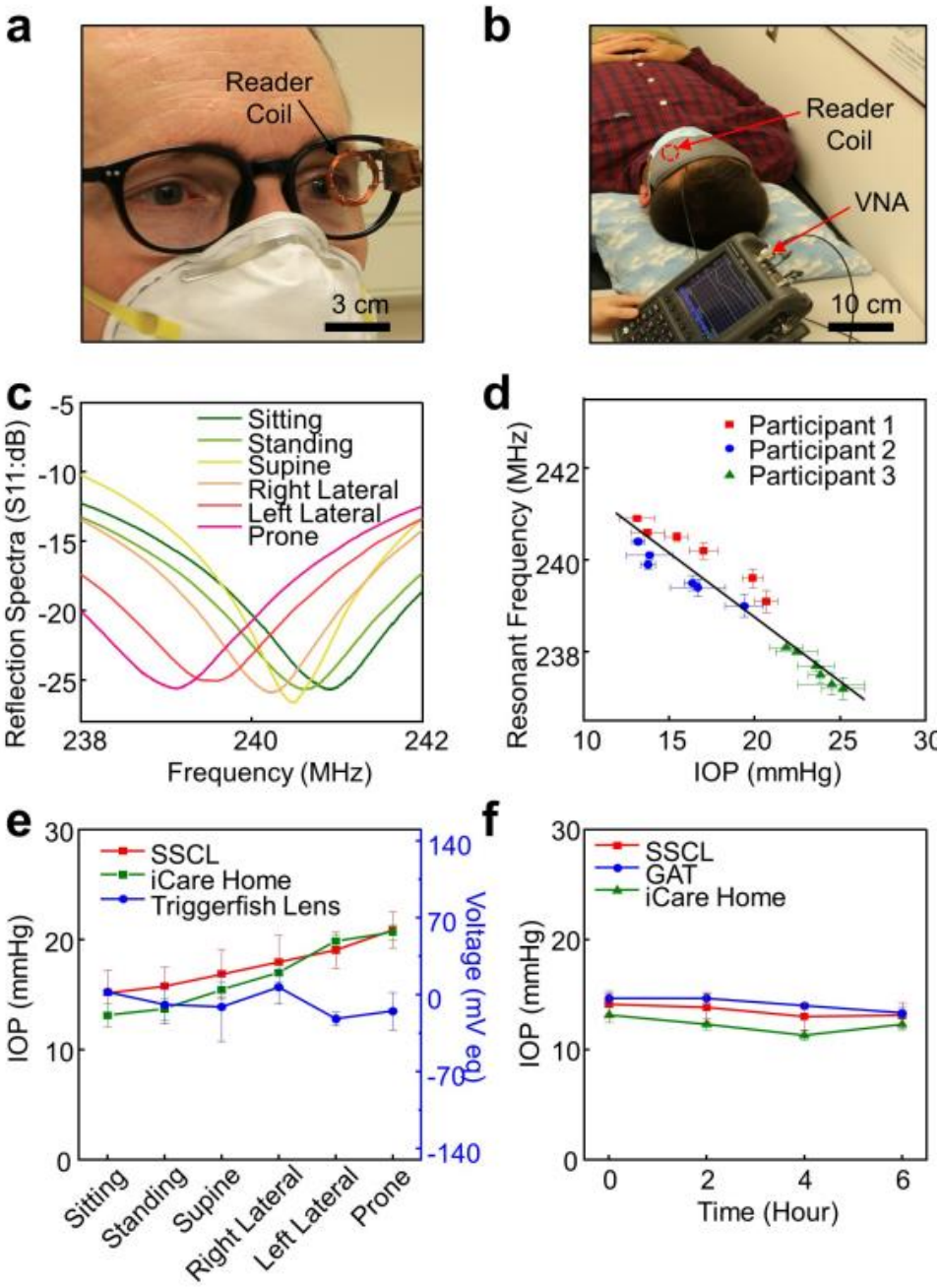

Figure 5.14. Ambulatory IOP monitoring in human eyes. (a) Photograph of a participant wearing the SSCL in a sitting posture with the reader coil embedded within a typical eyeglass frame and (b) a sleep eye mask. (c) Reflection spectra (S11) of the SSCL in response to various body postures. (d) Resonant frequency of the SSCL in each body posture for a total of 3 participants with different corneal curvatures and thicknesses (n = 3). (e) Calibrated absolute IOP data of a participant using the SSCL (red line), the iCare Home (green line), and the Triggerfish lens (blue line). (f) Time-varying change in the ambulatory IOP of a participant obtained using the SSCL (red line), the GAT (blue line), and the iCare Home (green line) for 6 hours (n = 3).

Figure 5.14e presents the calibrated absolute IOP values of a participant wearing the SSCL as compared to control measurements using the iCare Home and the Triggerfish lens on the same eye. The measurement results of the SSCL agreed well with those of the iCare Home, which also agreed with prior reports (Figure 5.15a).[47–50] The IOP values of the SSCL were strongly correlated with those of the iCare Home irrespective of whether the eyelid was open or closed (Figure 5.15b). These results were reproduced in different batches of the SSCL using the same brand (Air Optix Night & Day Aqua; Alcon, Inc.) of its bare soft contact lens (Figure 5.15c). On the other hand, the measurement results of the Triggerfish lens barely agreed due to its challenge in fitting a variety of corneal curvatures and thicknesses in human eyes. The weak correlation of the Triggerfish lens (i.e., relative IOP change in mV eq) with actual IOP values in human eyes has also been observed in prior reports.[11,50]

Figure 5.14f shows the time-varying change of the absolute IOP value in a participant wearing the SSCL for 6 hours under ambulatory conditions as compared to control measurements using the iCare Home and the GAT on the same eye. The measurement results of the SSCL were closer to those of the GAT over the iCare Home. The high measurement accuracy and within-subject repeatability of the SSCL were mainly attributed to its seamless and reliable fit across different corneal curvatures and thicknesses of the eyes. Importantly, the SSCL induced no heat unlike the Triggerfish lens (Figure 5.16), and thereby can eliminate safety risks associated with ocular burn and dehydration. To avoid excessive heating of the Triggerfish lens, a sufficient time interval (i.e., 5 minutes) was applied between each measurement.[51]

Table 5.2. Comparison of the SSCL with current wearable ocular tonometers in terms of sensing materials, working principle, responsivity, and sensitivity.

Validated in Human Eyes	Sensing Materials	Working Principle	Responsivity	Sensitivity (ppm $mmHg^{-1}$)	Ref.
Yes	AgSEBS/ Silbione/PDMS	Capacitive/ Inductive	0.27 MHz $mmHg^{-1}$	1,121	This work
Yes	AgNF-AgNW	Piezoresistive	N/A	500	[44]
No	GNWs	Piezoresistive	1.014 kOhm $mmHg^{-1}$	42,250	[45]
No	Graphene/AgNWs	Capacitive/ Inductive	2.64 MHz $mmHg^{-1}$	640	[46]
No	Graphene	Piezoresistive	N/A	68,000	[47]
No	Parylene C/Au/PDMS	Inductive	0.0468 MHz $mmHg^{-1}$	111	[48]

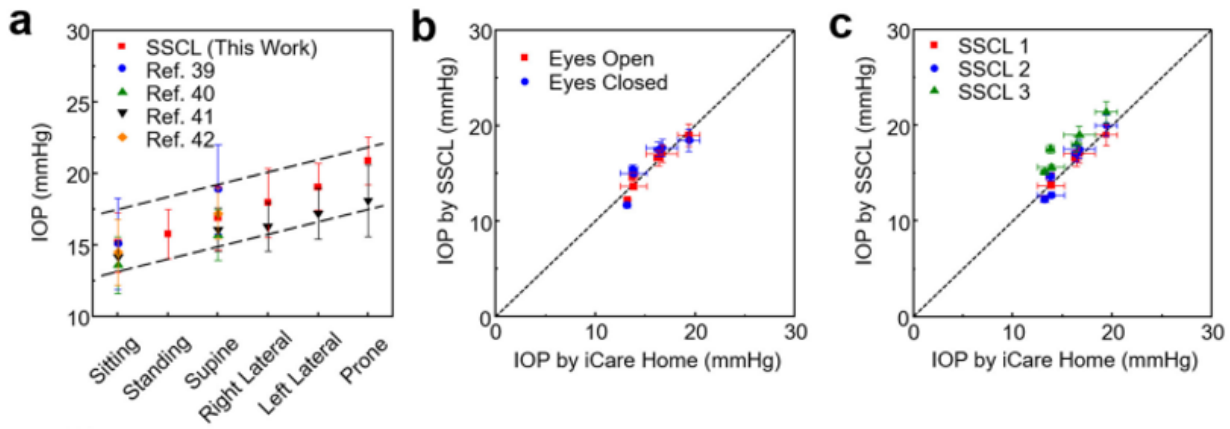

Figure 5.15. (a) Comparison of the IOP data obtained from the SSCL with prior studies. The dashed lines denote the range of IOP under each postural condition in prior studies. (b) Correlation of the IOP data obtained from the SSCL and the iCare Home with the eye open or closed (n = 3). (c) Correlation of the IOP data obtained from the SSCL and the iCare Home with different batches of the SSCL (n = 3).

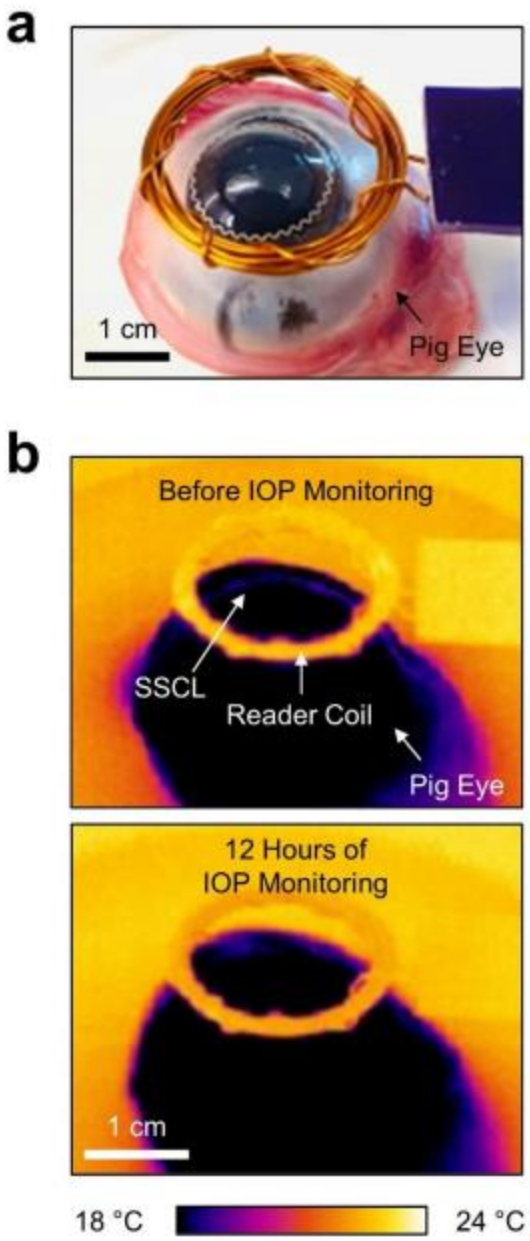

Figure 5.16. (a) Photograph of the SSCL in an enucleated pig eye. (b) Infrared (IR) image of the SSCL before (top panel) and after (bottom panel) 12 hours of IOP monitoring.

In conclusion, we report a safe and effective sensing platform for the continuous monitoring of glaucoma even during sleep at home with superior safety, user comfort, lens fit, visual field, ease-of-use, overnight wearability, and signal quality beyond current wearable ocular tonometers. Uniquely, this platform is built upon various commercial brands of soft contact lenses that have been proven safe for those whether or not the presence of glaucoma or

following incisional surgeries. We envision that this sensing platform will be of great significance for the management of glaucoma by enabling: (1) the continuous monitoring of glaucoma progression or treatment response on a daily to weekly to monthly basis at home; (2) the immediate alert for any event of ocular hypertension even during sleep; and (3) the development of optimal treatment regimes. As potential future directions, this sensing platform can be tailored for other chronic ocular diseases such as cataract and age-related macular degeneration.

5.5 References

(1) Weinreb, R. N.; Aung, T.; Medeiros, F. A. The Pathophysiology and Treatment of Glaucoma: A Review. *Jama* **2014**, *311* (18), 1901–1911.

(2) Beykin, G.; Norcia, A. M.; Srinivasan, V. J.; Dubra, A.; Goldberg, J. L. Discovery and Clinical Translation of Novel Glaucoma Biomarkers. *Prog. Retin. Eye Res.* **2021**, *80*, 100875.

(3) Garway-Heath, D. F.; Crabb, D. P.; Bunce, C.; Lascaratos, G.; Amalfitano, F.; Anand, N.; Azuara-Blanco, A.; Bourne, R. R.; Broadway, D. C.; Cunliffe, I. A. Latanoprost for Open-Angle Glaucoma (UKGTS): A Randomised, Multicentre, Placebo-Controlled Trial. *Lancet* **2015**, *385* (9975), 1295–1304.

(4) Li, G.; Lee, C.; Agrahari, V.; Wang, K.; Navarro, I.; Sherwood, J. M.; Crews, K.; Farsiu, S.; Gonzalez, P.; Lin, C.-W. In Vivo Measurement of Trabecular Meshwork Stiffness in a Corticosteroid-Induced Ocular Hypertensive Mouse Model. *Proc. Natl. Acad. Sci.* **2019**, *116* (5), 1714–1722.

(5) Gordon, M. O.; Kass, M. A. What We Have Learned from the Ocular Hypertension Treatment Study. *Am. J. Ophthalmol.* **2018**, *189*, xxiv–xxvii.

(6) Chintalapudi, S. R.; Maria, D.; Di Wang, X.; Bailey, J. N. C.; Hysi, P. G.; Wiggs, J. L.; Williams, R. W.; Jablonski, M. M. Systems Genetics Identifies a Role for Cacna2d1 Regulation in Elevated Intraocular Pressure and Glaucoma Susceptibility. *Nat. Commun.* **2017**, *8* (1), 1–12.

(7) Flatau, A.; Solano, F.; Idrees, S.; Jefferys, J. L.; Volpe, P.; Damion, C.; Quigley, H. A. Measured Changes in Limbal Strain during Simulated Sleep in Face down Position Using an Instrumented Contact Lens in Healthy Adults and Adults with Glaucoma. *JAMA Ophthalmol.* **2016**, *134* (4), 375–382.

(8) Mostafa, I.; Bianchi, E.; Brown, L.; Tatham, A. J. What Is the Best Way to Measure Intraocular Pressure (IOP) in a Virtual Clinic? *Eye* **2021**, *35* (2), 448–454.

(9) Aptel, F.; Weinreb, R. N.; Chiquet, C.; Mansouri, K. 24-h Monitoring Devices and Nyctohemeral Rhythms of Intraocular Pressure. *Prog. Retin. Eye Res.* **2016**, *55*, 108–148.

(10) Pronin, S.; Brown, L.; Megaw, R.; Tatham, A. J. Measurement of Intraocular Pressure by Patients with Glaucoma. *JAMA Ophthalmol.* **2017**, *135* (10), 1030–1036.

(11) Vitish-Sharma, P.; Acheson, A. G.; Stead, R.; Sharp, J.; Abbas, A.; Hovan, M.; Maxwell-Armstrong, C.; Guo, B.; King, A. J. Can the SENSIMED Triggerfish® Lens Data Be Used as an Accurate Measure of Intraocular Pressure? *Acta Ophthalmol.* **2018**, *96* (2), e242–e246.

(12) Dunbar, G. E.; Shen, B. Y.; Aref, A. A. The Sensimed Triggerfish Contact Lens Sensor: Efficacy, Safety, and Patient Perspectives. *Clin. Ophthalmol. (Auckland, NZ)* **2017**, *11*, 875.

(13) Jang, J.; Kim, J.; Shin, H.; Park, Y.-G.; Joo, B. J.; Seo, H.; Won, J.; Kim, D. W.; Lee, C. Y.; Kim, H. K. Smart Contact Lens and Transparent Heat Patch for Remote Monitoring and Therapy of Chronic Ocular Surface Inflammation Using Mobiles. *Sci. Adv.* **2021**, *7* (14), eabf7194.

(14) Ku, M.; Kim, J.; Won, J.-E.; Kang, W.; Park, Y.-G.; Park, J.; Lee, J.-H.; Cheon, J.; Lee, H. H.; Park, J.-U. Smart, Soft Contact Lens for Wireless Immunosensing of Cortisol. *Sci. Adv.* **2020**, *6* (28), eabb2891.

(15) Park, J.; Kim, J.; Kim, S.-Y.; Cheong, W. H.; Jang, J.; Park, Y.-G.; Na, K.; Kim, Y.-T.; Heo, J. H.; Lee, C. Y. Soft, Smart Contact Lenses with Integrations of Wireless Circuits, Glucose Sensors, and Displays. *Sci. Adv.* **2018**, *4* (1), eaap9841.

(16) Keum, D. H.; Kim, S.-K.; Koo, J.; Lee, G.-H.; Jeon, C.; Mok, J. W.; Mun, B. H.; Lee, K. J.; Kamrani, E.; Joo, C.-K. Wireless Smart Contact Lens for Diabetic Diagnosis and Therapy. *Sci. Adv.* **2020**, *6* (17), eaba3252.

(17) Park, J.; Ahn, D. B.; Kim, J.; Cha, E.; Bae, B.-S.; Lee, S.-Y.; Park, J.-U. Printing of Wirelessly Rechargeable Solid-State Supercapacitors for Soft, Smart Contact Lenses with Continuous Operations. *Sci. Adv.* **2019**, *5* (12), eaay0764.

(18) Sim, K.; Chen, S.; Li, Z.; Rao, Z.; Liu, J.; Lu, Y.; Jang, S.; Ershad, F.; Chen, J.; Xiao, J. Three-Dimensional Curvy Electronics Created Using Conformal Additive Stamp Printing. *Nat. Electron.* **2019**, *2* (10), 471–479.

(19) Yin, R.; Xu, Z.; Mei, M.; Chen, Z.; Wang, K.; Liu, Y.; Tang, T.; Priydarshi, M. K.; Meng, X.; Zhao, S. Soft Transparent Graphene Contact Lens Electrodes for Conformal Full-Cornea Recording of Electroretinogram. *Nat. Commun.* **2018**, *9* (1), 1–11.

(20) Guo, S.; Wu, K.; Li, C.; Wang, H.; Sun, Z.; Xi, D.; Zhang, S.; Ding, W.; Zaghloul, M. E.; Wang, C. Integrated Contact Lens Sensor System Based on Multifunctional Ultrathin MoS2 Transistors. *Matter* **2021**, *4* (3), 969–985.

(21) Kim, K.; Kim, H. J.; Zhang, H.; Park, W.; Meyer, D.; Kim, M. K.; Kim, B.; Park, H.; Xu, B.; Kollbaum, P. All-Printed Stretchable Corneal Sensor on Soft Contact Lenses for Noninvasive and Painless Ocular Electrodiagnosis. *Nat. Commun.* **2021**, *12* (1), 1–11.

(22) Kim, K.; Kim, B.; Lee, C. H. Printing Flexible and Hybrid Electronics for Human Skin and Eye-Interfaced Health Monitoring Systems. *Adv. Mater.* **2020**, *32* (15), 1902051.

(23) Nicolson, P. C.; Vogt, J. Soft Contact Lens Polymers: An Evolution. *Biomaterials* **2001**, *22* (24), 3273–3283.

(24) DR, S.; G, D. Cornea and Contact Lens Considerations in Glaucoma - Modern Optometry. *Int. J. open Access Ophthalmol.* **2018**, *3* (1), 1–5.

(25) Kim, J.; Cha, E.; Park, J. U. Recent Advances in Smart Contact Lenses. *Adv. Mater. Technol.* **2020**, *5* (1), 1900728.

(26) Kim, B.; Soepriatna, A. H.; Park, W.; Moon, H.; Cox, A.; Zhao, J.; Gupta, N. S.; Park, C. H.; Kim, K.; Jeon, Y.; et al. Rapid Custom Prototyping of Soft Poroelastic Biosensor for Simultaneous Epicardial Recording and Imaging. *Nat. Commun. 2021 121* **2021**, *12* (1), 1–14.

(27) Song, E.; Li, J.; Won, S. M.; Bai, W.; Rogers, J. A. Materials for Flexible Bioelectronic Systems as Chronic Neural Interfaces. *Nat. Mater. 2020 196* **2020**, *19* (6), 590–603.

(28) Yu, X.; Xie, Z.; Yu, Y.; Lee, J.; Vazquez-Guardado, A.; Luan, H.; Ruban, J.; Ning, X.; Akhtar, A.; Li, D.; et al. Skin-Integrated Wireless Haptic Interfaces for Virtual and Augmented Reality. *Nat. 2019 5757783* **2019**, *575* (7783), 473–479.

(29) Wang, C.; Qi, B.; Lin, M.; Zhang, Z.; Makihata, M.; Liu, B.; Zhou, S.; Huang, Y. hsi; Hu, H.; Gu, Y.; et al. Continuous Monitoring of Deep-Tissue Haemodynamics with Stretchable Ultrasonic Phased Arrays. *Nat. Biomed. Eng. 2021 57* **2021**, *5* (7), 749–758.

(30) Huang, Z.; Hao, Y.; Li, Y.; Hu, H.; Wang, C.; Nomoto, A.; Pan, T.; Gu, Y.; Chen, Y.; Zhang, T.; et al. Three-Dimensional Integrated Stretchable Electronics. *Nat. Electron. 2018 18* **2018**, *1* (8), 473–480.

(31) Wei, S.; Yin, R.; Tang, T.; Wu, Y.; Liu, Y.; Wang, P.; Wang, K.; Mei, M.; Zou, R.; Duan, X. Gas-Permeable, Irritation-Free, Transparent Hydrogel Contact Lens Devices with Metal-Coated Nanofiber Mesh for Eye Interfacing. *ACS Nano* **2019**, *13* (7), 7920–7929.

(32) Raghunathan, V. K.; Thomasy, S. M.; Strøm, P.; Yañez-Soto, B.; Garland, S. P.; Sermeno, J.; Reilly, C. M.; Murphy, C. J. Tissue and Cellular Biomechanics during Corneal Wound Injury and Repair. *Acta Biomater.* **2017**, *58*, 291–301.

(33) Hu, S.; Pei, X.; Duan, L.; Zhu, Z.; Liu, Y.; Chen, J.; Chen, T.; Ji, P.; Wan, Q.; Wang, J. A Mussel-Inspired Film for Adhesion to Wet Buccal Tissue and Efficient Buccal Drug Delivery. *Nat. Commun. 2021 121* **2021**, *12* (1), 1–17.

(34) Chen, P. Y.; Sakhdari, M.; Hajizadegan, M.; Cui, Q.; Cheng, M. M. C.; El-Ganainy, R.; Alù, A. Generalized Parity–Time Symmetry Condition for Enhanced Sensor Telemetry. *Nat. Electron. 2018 15* **2018**, *1* (5), 297–304.

(35) Bouhenni, R. A.; Dunmire, J.; Sewell, A.; Edward, D. P. Animal Models of Glaucoma. *J. Biomed. Biotechnol.* **2012**, *2012*.

(36) Jonas, J. B.; Aung, T.; Bourne, R. R.; Bron, A. M.; Ritch, R.; Panda-Jonas, S. Glaucoma – Authors' Reply. *Lancet* **2018**, *391* (10122), 740.

(37) Kenny, S. E.; Tye, C. B.; Johnson, D. A.; Kheirkhah, A. Giant Papillary Conjunctivitis: A Review. *Ocul. Surf.* **2020**, *18* (3), 396–402.

(38) Pallikaris, I. G.; Dastiridou, A. I.; Tsilimbaris, M. K.; Karyotakis, N. G.; Ginis, H. S. Ocular Rigidity. *http://dx.doi.org/10.1586/eop.10.30* **2014**, *5* (3), 343–351.

(39) Liu, Z.; Wang, G.; Ye, C.; Sun, H.; Pei, W.; Wei, C.; Dai, W.; Dou, Z.; Sun, Q.; Lin, C. Te; et al. An Ultrasensitive Contact Lens Sensor Based On Self-Assembly Graphene For Continuous Intraocular Pressure Monitoring. *Adv. Funct. Mater.* **2021**, *31* (29), 2010991.

(40) Shahid, S. M.; Ahmed, S. N.; Khan, Y. Eye Problems in Contact Lens Wearers. *BMJ* **2019**, *367*.

(41) Kollbaum, P. S.; Jansen, M. E.; Rickert, M. E. Comparison of Patient-Reported Visual Outcome Methods to Quantify the Perceptual Effects of Defocus. *Contact Lens Anterior Eye* **2012**, *35* (5), 213–221.

(42) Kim, J.; Park, J.; Park, Y.-G.; Cha, E.; Ku, M.; An, H. S.; Lee, K.-P.; Huh, M.-I.; Kim, J.; Kim, T.-S. A Soft and Transparent Contact Lens for the Wireless Quantitative Monitoring of Intraocular Pressure. *Nat. Biomed. Eng.* **2021**, *5* (7), 772–782.

(43) Liu, Z.; Wang, G.; Pei, W.; Wei, C.; Wu, X.; Dou, Z.; Li, Y.; Wang, Y.; Chen, H. Application of Graphene Nanowalls in an Intraocular Pressure Sensor. *J. Mater. Chem. B* **2020**, *8* (38), 8794–8802.

(44) Kim, J.; Kim, M.; Lee, M.-S.; Kim, K.; Ji, S.; Kim, Y.-T.; Park, J.; Na, K.; Bae, K.-H.; Kyun Kim, H. Wearable Smart Sensor Systems Integrated on Soft Contact Lenses for Wireless Ocular Diagnostics. *Nat. Commun.* **2017**, *8* (1), 1–8.

(45) Zhang, Y.; Chen, Y.; Man, T.; Huang, D.; Li, X.; Zhu, H.; Li, Z. High Resolution Non-Invasive Intraocular Pressure Monitoring by Use of Graphene Woven Fabrics on Contact Lens. *Microsystems Nanoeng. 2019 51* **2019**, *5* (1), 1–8.

(46) Kouhani, M. H. M.; Wu, J.; Tavakoli, A.; Weber, A. J.; Li, W. Wireless, Passive Strain Sensor in a Doughnut-Shaped Contact Lens for Continuous Non-Invasive Self-Monitoring of Intraocular Pressure. *Lab Chip* **2020**, *20* (2), 332–342.

(47) Lindén, C.; Qvarlander, S.; Jóhannesson, G.; Johansson, E.; Östlund, F.; Malm, J.; Eklund, A. Normal-Tension Glaucoma Has Normal Intracranial Pressure: A Prospective Study of Intracranial Pressure and Intraocular Pressure in Different Body Positions. *Ophthalmology* **2018**, *125* (3), 361–368.

(48) Lee, T. E.; Yoo, C.; Lin, S. C.; Kim, Y. Y. Effect of Different Head Positions in Lateral Decubitus Posture on Intraocular Pressure in Treated Patients With Open-Angle Glaucoma. *Am. J. Ophthalmol.* **2015**, *160* (5), 929-936.e4.

(49) Lee, T. E.; Yoo, C.; Kim, Y. Y. Effects of Different Sleeping Postures on Intraocular Pressure and Ocular Perfusion Pressure in Healthy Young Subjects. *Ophthalmology* **2013**, *120* (8), 1565–1570.

(50) Eklund, A.; Jóhannesson, G.; Johansson, E.; Holmlund, P.; Qvarlander, S.; Ambarki, K.; Wåhlin, A.; Koskinen, L. O. D.; Malm, J. The Pressure Difference between Eye and Brain Changes with Posture. *Ann. Neurol.* **2016**, *80* (2), 269–276.

(51) Farandos, N. M.; Yetisen, A. K.; Monteiro, M. J.; Lowe, C. R.; Yun, S. H. Contact Lens Sensors in Ocular Diagnostics. *Adv. Healthc. Mater.* **2015**, *4* (6), 792–810.

6. CONCLUSIONS AND FUTURE WORK

The present dissertation highlights research efforts that advance organic bioelectronics both on the fundamental and applied fronts. Specifically, many work revolves around design and application of organic mixed ion and electron conductors (OMIECs) that simultaneously conduct ionic and electronic currents. An alternative class of conducting macromolecules to conventionally adopted conjugated polymers, a nonconjugated radical polymer is used for the first time as a blended active layer in the organic electrochemical transistor (OECT) devices. On the other hand, new approaches to designing wearable ocular electrophysiology sensors with high performance and patient comfort are presented, where sensor components are integrated onto commercial soft contact lenses (SCLs) using soft materials.

While the work discussed in this dissertation contributes to organic electronics research both on fundamental and applied fronts, there are venues worth investigating further to expand the scientific knowledge and techniques gained herein. Several ongoing and suggested future projects are introduced that extend from initial hypotheses of or findings from the work completed here. Pursuit of these efforts will advance the understanding of the structure-property relationships of mixed conduction in radical polymers and realization of next generation of various organic electronic devices.

6.1 Balancing Mixed Transport in Radical-bearing Mixed Conductors

Chapter 3 demonstrates the contribution of the radical moieties blended into a model conjugated polymer matrix for the OECT testbeds (Figure 6.1a). However, the present blending strategy bears certain limitations. These are: (1) the hydrophobicity of the conjugated polymer cannot be tuned, (2) phase separation occurs at moderate to high blending ratios, and (3) composition of the hydrophilic moiety (PEO backbone) and the radical moiety (TEMPO) cannot be adjusted. As such, a different molecular design strategy of incorporating stable radicals into OECT organic semiconductors is desired. One such approach involves synthesizing conjugated radical polymers (CRPs) grafted with both radical species and hydrophilic functional groups (Figure 6.1b). Tuning the ratio between the bare backbone, ethylene glycol (EG) functionalized

backbone, and the radical functionalized backbone will provide a better handle in evaluating the effect of radical pendant groups in mixed conduction.

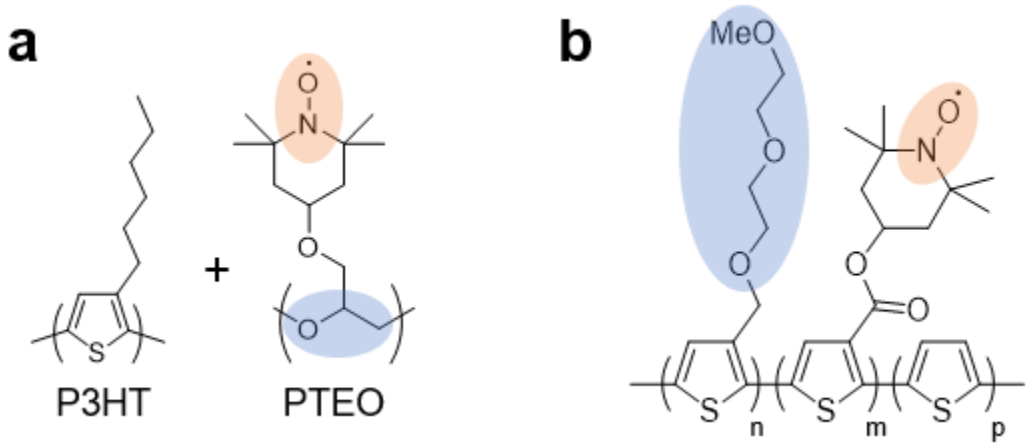

Figure 6.1. (a) P3HT and PTEO were blended as the OECT active layer. (b) Conceptual design of a novel copolymer which has both hydrophilic (e.g., TEG) and a stable radical (e.g., TEMPO) side chains. Blue and orange highlights denote the hydrophilic moiety and the secondary redox-active radical species, respectively.

In addition, various combinations of backbone and radical chemistries may be designed to better understand the interactions between the two redox active species. In Chapter 3, the thiophene backbone had a higher oxidation potential that that of the TEMPO radical. Reversal of the relative potential may draw out a different OECT characteristics altogether, and such manipulation may prove as another useful handle to dictate the mechanism of such phenomenon.[1] Further examination on how the interaction between the radical species and the conjugated system impacts sought-out metrics for the OECT application (i.e., threshold voltage, volumetric capacitance, time response, etc.) will lead to design of next-generation OECT materials.

6.2 Investigation of Solid-state Charge Conduction of Different Radical Species

Owing to the unusual stability of the neutral radical, numerous macromolecular designs bearing TEMPO radicals have been designed for solid-state charge conduction[9–15] and energy storage applications.[16–20] Despite considerable success, relatively low electronic conductivity of nonconjugated radical polymers remains a prominent hurdle for practical applications. A more-

in-depth grasp of the structure-property relationship of these radical conductors is therefore highly desired. For instance, there are other radical moieties (e.g., galvinoxyl and verdazyl radicals) with potentially superior charge conduction properties that are studied with much less frequency. These radical species are predicted to exhibit varying degrees of radical delocalization as opposed to highly localized TEMPO radicals, which are preferential toward radical-radical coupling and hence higher charge conduction.[21] Recently a nonconjugated macromolecule bearing galvinoxyl pendant groups, poly[2,6-di-*tert*-butyl-4-((3,5-di-*tert*-butyl-4-(λ1-oxidaneyl)phenyl)(4-((3-(methoxydimethylsilyl)propoxy)methylene)cyclohexa-2,5-dien-1-one] (PGMS) was synthesized by our research group, and the galvinoxyl-based polymer showed a high electronic conductivity in the order of 10^{-2} S m^{-1} despite having a low radical content of ~36%.[15] As another experimental effort in this front, poly[3-(4-(1-(3-methoxy-2-methylpropyl)-1,2,3-triazol-4-yl)phenyl)-1,2,4,5-tetrazin-6-one] (TA-PVEO) was synthesized by our research group (Figure 6.2). The design motif for TA-PVEO follows that of PTEO, where the poly(ethylene oxide) (PEO) backbone would render a low glass transition temperature (T_g) to promote formation of the inter-radical percolation network. As a result, TA-PVEO featured a low T_g of ~−20°C. Solid-state electronic conductivity of ~10^{-4} S m^{-1} was achieved, which was obtained for TA-PVEO samples with relatively low radical contents of ~15% (Figure 6.2b and c). While the effect of thermal annealing was not observed, this may be a result of not having sufficient radicals in close proximity due to a low radical content.

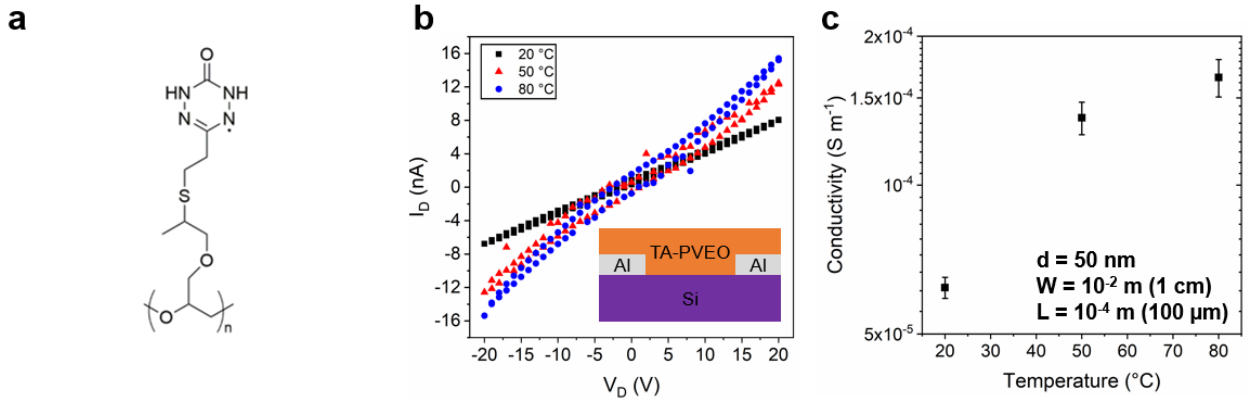

Figure 6.2. (a) Chemical structure of TA-PVEO. (b) I-V sweeps of the TA-PVEO thin film with Al electrode at three different temperature values. The channel length, width and the film thickness are 50 nm, 1 cm, and 100 µm, respectively. (c) The electronic conductivity of TA-PVEO shows promising results for verdazyl-based nonconjugated macromolecules as solid-state charge conductor. The data were averaged over five separate devices, and the error bars represent the values that are one standard deviation from that average value.

While the observed electronic conductivities of PGMS and TA-PVEO were several orders of magnitude lower than observed for PTEO, it is worth noting that at similar radical contents PTEO was found to have conductivity in the order of ~10^{-8} S m^{-1} or less.[12] As the radical content is correlated with the connectivity and hence the overall conductivity, overcoming the issues of synthetic challenges to yield high radical content and stability of galvinoxyl- and verdazyl-based radical polymers would lead to improvement in electronic conductivity and more extensive utilization in developing next-generation organic electronic devices.

6.3 Developing Advanced Smart Soft Contact Lenses

The integration strategy detailed in Chapter 5 has the potential to be utilized in developing next-generation wearable ocular sensors for purpose beside continuous IOP tracking. While the ERG sensor presented in Chapter 4 showed state-of-the-art performance and with significantly improved patient comfort, the PEDOT:Tos electrode was in direct contact with the patient's cornea (Figure 6.3a). In addition, the design requires electroplating of a thin gold (Au) layer before electropolymerization because the Ag/SEBS composite chemically reacts (i.e., Ag ionizes into Ag^{+}). On the other hand, the PDA-based bonding strategy is universally applicable without safety risks for any type of sensor as long as its mechanical flexibility is comparable to that of the commercial SCLs (Figure 6.3b). For instance, ERG electrodes on introduced in Chapter 4 could theoretically designed using PDA adhesive coating, where anchoring via electropolymerization may be removed altogether (Figure 6.3c). As opposed to having a distinction between the working electrode (e.g., PEDOT:Tos) and the interconnect (e.g., Ag/SEBS), the two components may be integrated into one by using a conductive polymer/elastomer composite.[22–25] In addition, a perforated protective layer of biocompatible elastomer (e.g., PDMS) may be placed on top of the conductive layer to avoid direct contact between the eye and the working electrode for additional protection. As such, there are venues for further improvement upon the designs presented in this dissertation, and further research efforts will contribute to developing superior wearable ocular sensors and realization of practical application.

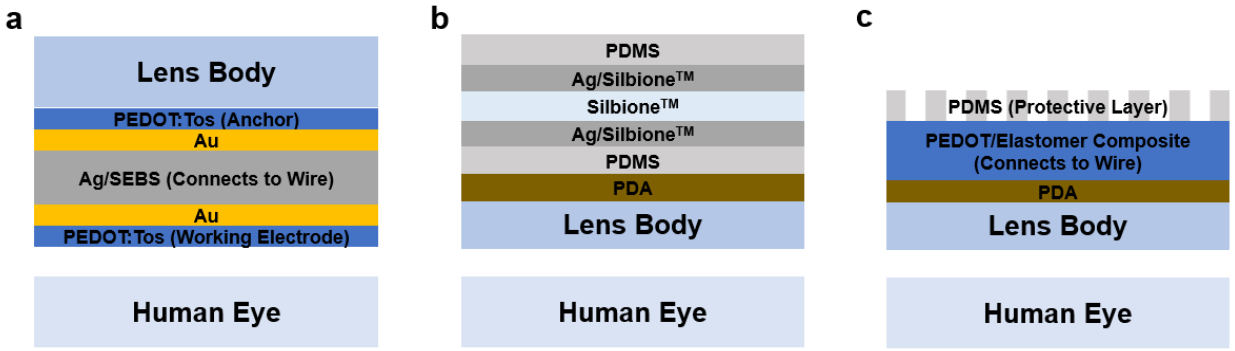

Figure 6.3. Schematic cross-sectional illustrations of (a) an ERG and (b) an IOP sensor discussed in Chapters 4 and 5, respectively. (c) A conceptual design of an all-organic ERG electrode may be realized by using PDA-assisted bonding and PEDOT-based elastomer composite interconnect. In this approach the cornea the organic conductor is placed on the anterior of the SCL, thereby further reducing the patient discomfort.

6.4 References

(1) Li, F.; Gore, D. N.; Wang, S.; Lutkenhaus, J. L. Unusual Internal Electron Transfer in Conjugated Radical Polymers. *Angew. Chemie - Int. Ed.* **2017**, *56* (33), 9856–9859.

(2) Jones, B. A.; Ahrens, M. J.; Yoon, M. H.; Facchetti, A.; Marks, T. J.; Wasielewski, M. R. High-Mobility Air-Stable n-Type Semiconductors with Processing Versatility: Dicyanoperylene-3,4:9,10-Bis(Dicarboximides). *Angew. Chemie - Int. Ed.* **2004**, *43* (46), 6363–6366.

(3) De Leeuw, D. M.; Simenon, M. M. J.; Brown, A. R.; Einerhand, R. E. F. Stability of N-Type Doped Conducting Polymers and Consequences for Polymeric Microelectronic Devices. *Synth. Met.* **1997**, *87* (1), 53–59.

(4) Giovannitti, A.; Maria, I. P.; Hanifi, D.; Donahue, M. J.; Bryant, D.; Barth, K. J.; Makdah, B. E.; Savva, A.; Moia, D.; Zetek, M.; et al. The Role of the Side Chain on the Performance of N-Type Conjugated Polymers in Aqueous Electrolytes. *Chem. Mater.* **2018**, *30* (9), 2945–2953.

(5) Zhan, X.; Facchetti, A.; Barlow, S.; Marks, T. J.; Ratner, M. A.; Wasielewski, M. R.; Marder, S. R. Rylene and Related Diimides for Organic Electronics. *Adv. Mater.* **2011**, *23* (2), 268–284.

(6) Dose, J.; Matsugo, S.; Yokokawa, H.; Koshida, Y.; Okazaki, S.; Seidel, U.; Eggersdorfer, M.; Rimbach, G.; Esatbeyoglu, T. Free Radical Scavenging and Cellular Antioxidant Properties of Astaxanthin. *Int. J. Mol. Sci.* **2016**, *17* (1), 103.

(7) Esatbeyoglu, T.; Wagner, A. E.; Motafakkerazad, R.; Nakajima, Y.; Matsugo, S.; Rimbach, G. Free Radical Scavenging and Antioxidant Activity of Betanin: Electron Spin Resonance Spectroscopy Studies and Studies in Cultured Cells. *Food Chem. Toxicol.* **2014**, *73*, 119–126.

(8) Assiri, A. M. A.; Elbanna, K.; Abulreesh, H. H.; Ramadan, M. F. Bioactive Compounds of Cold-Pressed Thyme (Thymus Vulgaris) Oil with Antioxidant and Antimicrobial Properties. *J. Oleo Sci.* **2016**, *65* (8), 629–640.

(9) Hay, M. E.; Hui Wong, S.; Mukherjee, S.; Boudouris, B. W. Controlling Open-Shell Loading in Norbornene-Based Radical Polymers Modulates the Solid-State Charge Transport Exponentially. *J. Polym. Sci. Part B Polym. Phys.* **2017**, *55* (20), 1516–1525.

(10) Tomlinson, E. P.; Hay, M. E.; Boudouris, B. W. Radical Polymers and Their Application to Organic Electronic Devices. *Macromolecules* **2014**, *47* (18), 6145–6158.

(11) Yu, I.; Jeon, D.; Boudouris, B.; Boudouris, B.; Joo, Y. Mixed Ionic and Electronic Conduction in Radical Polymers. *Macromolecules* **2020**, *53* (11), 4435–4441.

(12) Joo, Y.; Agarkar, V.; Sung, S. H.; Savoie, B. M.; Boudouris, B. W. A Nonconjugated Radical Polymer Glass with High Electrical Conductivity. *Science (80-.).* **2018**, *359* (6382), 1391–1395.

(13) Rostro, L.; Wong, S. H.; Boudouris, B. W. Solid State Electrical Conductivity of Radical Polymers as a Function of Pendant Group Oxidation State. *Macromolecules* **2014**, *47* (11), 3713–3719.

(14) Akkiraju, S.; Vergados, J.; Hoagland, L.; Lu, Z.; Anandan, V.; Boudouris, B. W. Design of Mixed Electron-and Ion-Conducting Radical Polymer-Based Blends. *Macromolecules* **2021**.

(15) Chi, T.; Akkiraju, S.; Liang, Z.; Tan, Y.; Kim, H. J.; Zhao, X.; Savoie, B. M.; Boudouris, B. W. Design of an N-Type Low Glass Transition Temperature Radical Polymer. *Polym. Chem.* **2021**, *12* (10), 1448–1457.

(16) Sato, K.; Sukegawa, T.; Oyaizu, K.; Nishide, H. Synthesis of Poly(TEMPO-Substituted Glycidyl Ether) by Utilizing t-BuOK/18-Crown-6 for an Organic Cathode-Active Material. In *Macromolecular Symposia*; Wiley Online Library, 2015; Vol. 351, pp 90–96.

(17) Wilcox, D. A.; Agarkar, V.; Mukherjee, S.; Boudouris, B. W. Stable Radical Materials for Energy Applications. *Annu. Rev. Chem. Biomol. Eng.* **2018**, *9*, 83–103.

(18) Hansen, K. A.; Nerkar, J.; Thomas, K.; Bottle, S. E.; O'Mullane, A. P.; Talbot, P. C.; Blinco, J. P. New Spin on Organic Radical Batteries-An Isoindoline Nitroxide-Based High-Voltage Cathode Material. *ACS Appl. Mater. Interfaces* **2018**, *10* (9), 7982–7988.

(19) Oyaizu, K.; Nishide, H. Radical Polymers for Organic Electronic Devices: A Radical Departure from Conjugated Polymers? *Adv. Mater.* **2009**, *21* (22), 2339–2344.

(20) Suga, T.; Ohshiro, H.; Ugita, S.; Oyaizu, K.; Nishide, H. Emerging N-Type Redox-Active Radical Polymer for a Totally Organic Polymer-Based Rechargeable Battery. *Adv. Mater.* **2009**, *21* (16), 1627–1630.

(21) Tan, Y.; Casetti, N. C.; Boudouris, B. W.; Savoie, B. M. Molecular Design Features for Charge Transport in Nonconjugated Radical Polymers. *J. Am. Chem. Soc.* **2021**, *143* (31), 11994–12002.

(22) Kayser, L. V.; Lipomi, D. J. Stretchable Conductive Polymers and Composites Based on PEDOT and PEDOT:PSS. *Adv. Mater.* **2019**, *31* (10), 1806133.

(23) Wang, Y.; Zhu, C.; Pfattner, R.; Yan, H.; Jin, L.; Chen, S.; Molina-Lopez, F.; Lissel, F.; Liu, J.; Rabiah, N. I. A Highly Stretchable, Transparent, and Conductive Polymer. *Sci. Adv.* **2017**, *3* (3), e1602076.

(24) Luo, R.; Li, H.; Du, B.; Zhou, S.; Zhu, Y. A Simple Strategy for High Stretchable, Flexible and Conductive Polymer Films Based on PEDOT: PSS-PDMS Blends. *Org. Electron.* **2020**, *76*, 105451.

(25) Ding, Y.; Yang, J.; Tolle, C. R.; Zhu, Z. Flexible and Compressible PEDOT: PSS@ Melamine Conductive Sponge Prepared via One-Step Dip Coating as Piezoresistive Pressure Sensor for Human Motion Detection. *ACS Appl. Mater. Interfaces* **2018**, *10* (18), 16077–16086.

VITA

EDUCATION

Ph.D. in Chemical Engineering
Purdue University, West Lafayette, IN
- Thesis Advisor: Dr. Bryan W. Boudouris
- Leslie Bottorff Fellowship: Awarded for excellence in interdisciplinary biomedical research

M.S. in Chemical Engineering
Stanford University, Stanford, CA

B.E. in Chemical Engineering
The Cooper Union for the Advancement of Science and Art, New York, NY
- Graduated Cum Laude
- Awarded a full-tuition scholarship of $120,000

RESEARCH EXPERIENCE

Graduate Research Assistant May 2018 – Present
Charles D. Davidson School of Chemical Engineering, Purdue University, IN
- Investigate the structure-property relationship of organic semiconductors in mixed conduction applications
- Fabricate thin film organic electronic devices and characterize their electronic and electrochemical properties
- Design and optimize seamless bonding of ocular electrophysiological sensors onto commercial contact lenses using various polymeric adhesives

Research Associate July 2016 – September 2017
Korea University, Seoul, Republic of Korea
- Synthesized and characterized morphology-controlled metal nanoparticles for hydrogen peroxide generation
- Investigated how alloying affected the physical properties and catalytic activity of nanoparticles

Research Intern July 2013 – September 2013
Korean Institute of Science and Technology (KIST), Seoul, Republic of Korea
- Investigated composition and treatment effects on the hygroscopicity of polyelectrolyte gel
- Simulated numerical models for gel swelling and relaxation

INDUSTRY EXPERIENCE

Packaging R&D Engineer August 2014 – June 2016

STATS ChipPAC, Incheon, Republic of Korea

- Worked with Sr. Packaging Engineers to execute packaging strategies to support new product development
- Planned and executed DOE on the flip chip and interposer attach processes for the Package-on-Package architecture to meet customer requirements and improved the process yield from 85% to > 99.5%
- Prepared prompt assessment reports, defined process specifications, and drafted standard operating procedures

TECHNICAL SKILLS

- Device fabrication techniques: photolithography & e-beam lithography, thermal and e-beam evaporation, dry (reactive ion) etching, parylene CVD, and vacuum probe station
- Laboratory techniques: NMR, EPR, GPC, DSC, and various syntheses
- Surface characterization: SEM, TEM, AFM, and profilometry
- Electrochemistry: CV and EIS
- Spectroscopy: FT-IR and UV-Vis spectroscopy
- Analytics: MATLAB, Python and JMP
- Engineering drawing: AutoCAD and KLayout

LEADERSHIP ROLES AND TEACHING EXPERIENCE

Lab Manager January 2020 – Present

Boudouris Research Group, Davidson School of Chemical Engineering, Purdue University

- Train new and returning users on general safety and various equipment
- Perform regular inspections to ensure laboratory hygiene and safety and comply with all OSHA regulations
- Resolve various equipment mechanical failures directly or by liaising with external technicians to ensure optimal laboratory output for fellow group members
- Administer chemical stock control and purchasing

Soft Materials Seminar Manager November 2020 – October 2021

Davidson School of Chemical Engineering, Purdue University

- Coordinated 50+ student researchers, including five faculty members, and invited speakers to organize weekly meetings and promote interdisciplinary discussions/research projects
- Hosted workshops for the second-year students to assist with oral presentations and qualifying exams

President August 2019 – January 2021

Korean Chemical Engineers at Purdue University

- Coordinated ~30 professors, students, and their families to hold regular social events

Teaching Assistant January 2019 – January 2020

Davidson School of Chemical Engineering, Purdue University

- Graduate-level Statistics (ChE 697)
- Undergraduate-level Statistics (ChE 320)

PUBLICATIONS

1. Zhang, J.; Kim, K.; **Kim, H. J.**; Meyer, D.; Park, W.; Lee, S. A.; Dai, Y.; Kim, B.; Moon, H.; Shah, J. V. Smart Soft Contact Lenses for Continuous 24-Hour Monitoring of Intraocular Pressure in Glaucoma Care. *Nat. Commun*. **2022**, *13* (1), 1–15.

2. Woeppel, A. B.; Schaefer, J.; **Kim, H. J.**; Boudouris, B. W.; Beaudoin, S. P. Ion-Selective Organic Electrochemical Transistor Sensors Using Molecularly Imprinted Polymers. *ACS Appl. Polym. Mater.* **2022**, *4* (9), 6667-6674.

3. **Kim, H. J.**; Perera, K.; Liang, Z.; Bowen, B.; Mei, J.; Boudouris, B. Radical Polymer-Based Organic Electrochemical Transistors. ACS Macro Lett. **2022**, 11 (2), 243–250.

4. Kim, K.; **Kim, H. J.**; Zhang, H.; Park, W.; Meyer, D.; Kim, M. K.; Kim, B.; Park, H.; Xu, B.; Kollbaum, P.; Boudouris, B.; Lee, C. H. All-Printed Stretchable Corneal Sensor on Soft Contact Lenses for Noninvasive and Painless Ocular Electrodiagnosis. *Nat. Commun. 2021 121* **2021**, *12* (1), 1–11.

5. Chi, T.; Akkiraju, S.; Liang, Z.; Tan, Y.; **Kim, H. J.**; Zhao, X.; Savoie, B. M.; Boudouris, B. W. Design of an N-Type Low Glass Transition Temperature Radical Polymer. *Polym. Chem.* **2021**, *12* (10), 1448–1457.